Scuola Internazionale Superiore di Studi Avanzati - Trieste

International School for Advanced Studies
- Astrophysics and Cosmology-

Thesis submitted for the degree of
Doctor Philosophie

Probing patchy reionization via CMB, LSS and their cross correlations

---

Candidate
Anirban Roy

Supervisors
Prof. Carlo Baccigalupi
Prof. Andrea Lapi
Prof. David Spergel

Academic Year 2018 – 2019

SISSA - Via Bonomea 265 - 34136 TRIESTE - ITALY

To,
My parents
and
The teachers who inspired me.

"*anadi-madhyantam ananta-viryam*
ananta-bahum sasi-surya-netram
pasyami tvam dipta-hutasa-vaktram
sva-tejasa visvam idam tapantam"

-Bhagavad Gita, Chapter 11, Verse 19

"*You are the origin without beginning, middle or end. You have numberless arms, and the sun and moon are among Your great unlimited eyes. By Your own radiance You are heating this entire universe.*"

-Bhagavad Gita, Chapter 11, Verse 19

Contents

Acknowledgement

> "All that we are is the result of what we have thought".
>
> *Gautama Budhha*

This thesis has hugely benefited from the guidance, discussions and support from many, and it is my genuine pleasure to express a deep sense of gratitude to them. Foremost, I would like to like to thank my advisors Prof. Carlo Baccigalupi, Prof. Andrea Lapi and Prof. David Spergel for allowing me to work with them jointly. Carlo always gave me a tremendous amount of freedom to work on a problem and gave his constant support whenever things did not work out. While working with him, I understood "foreground cleaning" for CMB is also a crucial task which should be seriously taken care to interpret the CMB dataset. I have numerous discussions with Andrea on several research topics which span over Gravitational waves to galaxy evolution and Quasars to cluster cosmology. It is always fun to work with him for hours sitting beside his desk in his office, 509. I am grateful to David for giving me his time irrespective of his busy schedule. If I have learnt so many things from someone on Astrophysics and Cosmology in a short time, that will be from David. I thank Luigi Danese for being an inspiration in my academic career.

Next, I would like to thank my collaborators for working together on several exciting projects. Among them, I want to express my special gratitude to Prof. Girish Kulkarni and Prof. Daniel Meerburg. I got a chance to work with the simulations of reionization, and this helped to build my computer skills to the next level. Daan is always open to discuss many topics and also helped me to improve my scientific writing skills. I am thankful to Daan and Girish for guiding me during the application period for the postdoc position. I thank Prof. Martin G. Haehnelt for his support and the hospitality of the University of Cambridge, where I spend a few months. It was one of the most exciting times in my academic journey. I thank Prof. Anthony Challinor for teaching me many topics in Cosmology and providing me with guidance for my future career path. I always enjoyed discussions with Anthony and the way he explains difficult concepts starting from the basic ideas without going into rigorous derivations.

Some of the projects that I carried out during my PhD tenure are not included in this thesis. I am thankful to Prof. Anjan Ananda Sen for involving me in those projects, which gave me a chance to explore outside the research line of my thesis. I also thank Prof. Kaushik Dutta and Prof. Shahin Sheikh-Jabberi for being a part of this collaboration and discussion on several topics related to Dark Energy.

I am privileged to have sufficient travel fund for visiting several institutions during my PhD life. Many discussions during those times helped significantly to develop my scientific skills. I want to thank Marcelo Alvarez, Soumen Basak, Nick Battaglia, Olivier Dore, Cora Dvorkin, Andrew Jaffee, Rishi Khatri, Eichiiro Komatsu, Nicoletta Krachmalnicoff, Suvodip Mukherjee, Davide Poletti, Tirthankar Roychaudhuri, Ravi sheth, Tarun Souradeep, Matteo Viel, Matias Zaldarriaga. I express my sincere gratitude to Prof. Graca Rocha and Prof. Kris Gorski for hosting me for several days in NASA JPL.

We usually do not get a chance to acknowledge our friends and family members in scientific papers, but their support plays a crucial role through the ups and downs of our research career. Here, I want to use the opportunity to thank them all. I am lucky that I have met some entertaining friends in Trieste. Among them, firstly, I would like to thank my office-mate, Sabyasachi for keeping the relaxed ambience in the office. None can expect a better office mate than him. I thank Aichaaa for being my "first friend" in Trieste, and even time flows very fast, all the memories we shared are unforgettable. Thanks to Gamze for being a travel companion and taking me to some places where I thought I never would be. I am grateful to Kemal and Sultan Gurler for hosting me several times in Turkey, where I used to visit during the breaks in PhD life.

I thank Arnab da, Ranjan da and Tanay da for giving me advice whenever I need it. They played a role as my elder brother in Trieste. Being with them, I have seen many intellectual debates (jokes apart!). I also thank Urna di for helping me with several things in the first two years of my PhD life, in particular, how to deal with very complicated and extended programming code. I want to thank Diksha, Sadaf, Srikanth, Gauri, Priyanka di, Raagini and other member's in "Nadan Parindey" group for arranging many events in Trieste. (Even I could not attend many of those during the last year of my PhD).

I want to thank other friends whom I met during my PhD life Burcu, Muntazir, Valeri, Zeynep, Malena, Nicolo, Carlos, Rodrigo, Nilufar, Raniero, Malena, Hasti, Jiaxin and Nilay. Anto, my only friend from Kerela, India, has an equal interest in science, arts and politics. In particular, I enjoyed most talking about Communism (as we both share a dream to change the world) and what strategy we should make to publish a paper in "Nature". I also thank Anna Paola and Laura for being wonderful flatmate and being big sisters in Trieste.

There is one friend in everybody's life who always gives support irrespective of the situation. My Friend, Arnab, played that role in my life. We started our Journey from Asutosh College, and we both are pursuing our career in Astrophysics and Cosmology, and I am sure that our path will cross again! I thank Arijeet, Prabal, Aparajita, Kankana, Biswabibek and all other friends from school, college and University. I collaborated with Ruchika on a scientific project, and after that, we had become friends. During her visit to Trieste, we spent lots of time talking about poetry and dark energy. Special thanks go to Anindita for keeping our friendship preserved and valuable as same as the school days.

I can not finish this section without mentioning my teachers who taught new things till today. I learned fundamental physics from my school teacher, Jyotirmoy Pattanayak, Ramchandra Das and Satyajit Manna. Later, I got interested more in some advanced topics in physics, and Krishnendu Ojha is the teacher who taught me Physics in my high school days. I also thank Prof. Atish Dipankar Jana, who always stressed to learn physics

with simple logic. I want to acknowledge Prof. Suchetana Chatterjee for teaching me some of the fundamental topics in cosmology. She is one of the most influential persons who inspired me first to pursue a research career in Cosmology.

I am lucky that I always get supports from my family members and relatives. My parents always encouraged to involve myself in scientific research, and their curiosity about the unknown world has inspired me very much. But staying in abroad was not easy for me when I need to take care of my family! All became possible because my brother, Archisman, was there in the correct time. He alone managed everything and never made me worried about family. Without him, my PhD journey could not be so smooth. Later, his wife, Tanushree, made our family more colourful and happier. I do not have any words to thank them all, and instead, I love them for the rest of my life!

Among my relatives, I want to thank my Mama (maternal uncle) and choto Meso (younger uncle). They always provide me with positive energy towards life which helped me to overcome some of the bad periods in my life. I have a very extended family in my village, Hamirpur in India, and it is impossible to acknowledge their contribution to my life individually. However, I would like to say that I got huge inspiration from the people of my village for their struggle in daily life.

In the end, I thank all the people in my beautiful country, India. I have completed my education in India without paying a huge amount of tuition fee. It became possible because of the contributions from the tax-payers' money. I will always carry my liability to them.

Abstract

> “If we knew what it was we were doing, it would not be called research, would it?”
>
> *Albert Einstein*

One of the most important predictions of the Big Bang theory is that the Universe will be filled with electromagnetic radiation as the remnant heat left-over, known as Cosmic Microwave Background (CMB) radiation. Through measurements of the CMB, a simple yet powerful model of the Universe has emerged, providing a precise estimate of its age, contents, topological properties and initial conditions. The latter are thought to be generated during a phase of transient vacuum energy in the very early Universe, the Inflation, driven by the physics of fundamental quantum fields. Although impressive, a question we hope to answer with future cosmological measurements is when cosmic Inflation happened by observing the imprints of those perturbations in the CMB. In particular, the spacetime metric itself is able to generate perturbations in terms of primordial gravitation waves, which perturb the CMB polarization in its curl (B) mode, at the last scattering onto electrons happened when CMB photons decoupled from the rest of the system forming neutral atoms (recombination), and later, hitting again electrons made free by the formation of first structures (reionization era). Cosmological gravitational waves generate B-modes at degree scales and different models of Inflation predict different amplitudes of the signal, which is parametrized in terms of the tensor-to-scalar ratio, r. Other cosmological sources of B-modes exist, such as the Gravitational lensing onto CMB photons travelling to us, deflected by forming cosmological structures, generating CMB anisotropies at the arcminute scale. Also, astrophysical contributions to B-modes, the so called foregrounds, are capable of contaminating the signal from primordial gravitational waves. Despite of these challenges, upcoming CMB experiments are set to detect a level $r \approx 10^{-3}$, as this level carries ultimate information of the Inflationary process itself.

On the other side, Reionization is believed to have occurred when the first generations of stars and quasars produced sufficient amounts of UV and X-ray radiation to ionize the vast majority of neutral hydrogen in the Universe. We have measurements telling us when the process started and ended, but poor knowledge of its details because of the complex physics involved. The epoch of Reionization (EoR) is the key event to understand the intergalactic medium (IGM) evolution and subsequent structure formation. For this reason, the study of the reionization epoch has now become a central topic in Astrophysics

and Cosmology. Precise measurements of the temperature and polarization anisotropies in CMB is one of the most promising probes of the EoR and hence, exploring fundamental questions in the field of Astrophysics and Cosmology.

CMB observations currently constrain the Reionization measuring the optical depth τ and its epoch parametrized by its mean redshift z. This thesis represents a step further in this analysis, investigating the spatial dependence of the process concerning the details of the involved astrophysical processes. Also, we consider how these new investigations modify the CMB signal induced by Reionization itself.

The astrophysics determining how the gas of known particles in the Universe passed from being almost neutral to the ionized state is related to the properties of high redshift galaxies, which are the primary sources of ionizing photons. The spatial structure ("Patchiness") of Reionization creates fluctuations in the electron density in different directions along the line of sight and generates secondary B-modes in the CMB, which are targets of the measurements of the ultimate CMB experiments in the next decade.

Our methodology includes performing cross correlation analyses of the fluctuations in optical depth with the brightness temperature in 21cm observations tracing neutral gas at high redshifts, along with its detectability from future CMB and 21cm probes. The measurements yield a determination of the sizes of the characteristic reionizing structures ("bubble") and ionization fraction as a function of redshifts.

B-modes in the CMB is generated as a consequence of patchy Reionization due to the screening and scattering mechanisms. We investigate the amplitude of the signal and studied its contamination to primordial B-modes. In particular, we exploit recent advances in the understanding of the reionization history through observations of the Lyman-α forest. We use high-dynamic-range radiative transfer simulations of cosmological Reionization that are calibrated to these data. These simulations allow us to calibrate the excursion set approach, providing the necessary validity check of this methodology. Our findings suggest that the contribution of Reionization to the search for primordial gravitational waves is unlikely to be a concern for sensitivities of planned and proposed experiments for most realistic models of the reionization history.

The thesis is organized as follows. We review the basic physics of the CMB in Chapter 1 and provide definitions relevant for the following Chapters. In Chapter 2 we describe how to model Reionization providing the basics of star formation history in high redshift galaxies; also, we explain the statistical techniques for the reconstruction of the optical depth and forecast the detectability by future CMB experiments. In chapter 3, we studied an alternative probe of patchy Reionization by performing the cross correlation of the optical depth field with the 21cm brightness temperature field. In chapter 4 we estimate the amplitude of the B-mode signal due to patchy Reionization by using high-dynamic-range radiative transfer simulation of Reionization; in particular, we study the contamination to the primordial B signal from cosmological gravitational waves.

Chapter 1

Basic physics of the Cosmic Microwave Background

> When our Universe is in harmony with man, the eternal, we know it as truth, we feel it as beauty.
>
> *Rabindranath Tagore*

As light takes a finite time to travel the distance between astrophysical objects and us, actually, we see them at the time when the light was emitted. What if we can see the Universe back in time when it was young? It is indeed possible because of the CMB; the Universe started from a hot and dense state, known as the big bang. After that, all the elementary particles such as electrons, protons and neutrons were together in a plasma state, in thermal equilibrium with the hot bath of the high energy photons. Russian born American physicist George Gamow considered for the first time the signatures of the hot big bang model in the present day [1, 2, 3]. Due to the expansion of the Universe, the temperature decreases and neutral hydrogen atoms formed when the thermal energy went below the binding energy of hydrogen atoms. Gamow made various predictions for the temperature of this radiation today is ~ 5K.

About two decades later, Penzias and Wilson accidentally discovered the radiation left over from the big bang in 1964 [4]. They found an unexpected noise in their radio receiver, which is same in every direction of the sky. The corresponding temperature of this signal was about 2.7 K. Penzias, and Wilson's discovery of the CMB started a new era in Cosmology. The CMB was expected to be mostly isotropic and characterized by a black body spectrum due to the expansion of the Universe. However, there should be fluctuations in the temperature and linear polarization via Thomson scattering due to the initial quantum fluctuations which will later form galaxies and large scale structures by the gravitational instability.

The CMB photons carry information about the early Universe and as well as for the late times. Different events in the timeline of the Universe modulate the fluctuations, and that is why the study of CMB provides a unique opportunity to understand the evolution of our Universe throughout its entire history. We now discuss the basic physics of the CMB after a brief description of the standard model of cosmology.

1.1 Standard model of cosmology

The Universe began to expand about 14 billion years ago in all directions from an infinitesimally small and infinitely dense point known as the singularity. The explanation about the beginning of time was derived from the standard model of big bang cosmology. The Big Bang model makes an accurate and scientifically testable hypothesis, which is in agreement with the observational datasets. After the big bang, every particle started rushing apart from each other in an early super-dense phase. Hubble [5, 6] first discovered the fact that galaxies are receding from us in all directions. He observed that light rays are coming from galaxies are redshifted rather than being blueshifted. He plotted redshift(z) vs distance of a galaxy (r) for almost 50 galaxies, and he found the famous linear relation, now known as Hubble's law, $z = H_0/c$, where H_0 is called Hubble constant. Hubble interpreted the observed redshift of galaxies as being a Doppler shift due to their radial velocity away from Earth. He concluded that all galaxies are moving away from each other. If v is the recessional velocity of a galaxy then according to classical non-relativistic relation for Doppler shift we have $v = H_0 r$. Projecting trajectories of galaxies backwards in time means they converge to a high density state which supports hot and dense phase of early Universe in Big Bang model of cosmology.

The standard model is also based on two fundamental assumptions which state that the Universe is homogeneous and isotropic, i.e. there is no preferred location and no preferred direction in our Universe. These principles mean if we are blindfolded and taken to any part of the Universe then after removal of the fold we are not able to tell where we are and in which direction we are looking at because Universe around us looks same in all directions. This principle holds only on the scales as large as 100 Mpc or more. The cosmological principle is also known as a generalization of "Copernican principle" who pointed out that Earth is not at the center of the Universe; in fact, there is no center of the Universe.

The theory of relativity tells us that space and time together comprise a 3+1 space-time continuum. If we include gravity, Einstein's general theory of relativity (GR) shows that in the presence of mass and energy space-time becomes curved. The Standard model assumes that Einstein's GR is the correct theory of gravity on the cosmological scale because it provides the framework of the formation of large scale structures observed in the Universe today. Under this assumption together with the cosmological principle, the metric of four-dimensional space-time can be written as [7]

$$ds^2 = c^2 dt^2 - R^2(t) \left[\frac{dr^2}{1 - Kr^2} + r^2 (d\theta^2 + sin^2\theta d\phi^2) \right] . \tag{1.1}$$

This equation is called Friedmann-Lemaitre-Robertson-Walker metric (FLRW) metric [8, 9, 10]. Here (r, θ, ϕ) are comoving coordinates and t is the cosmological proper time, $R(t)$ is the radius of curvature and K is the curvature parameter which can be one of the three values,i.e, $K = 0$ for flat space , $K = +1$ for positively curved space and $K = -1$ for negatively curved space. Standard model of cosmology is also known as Lambda-cold dark matter model or ΛCDM model [11, 12]. The letter "Λ" stands for the cosmological constant, which is currently associated with vacuum energy or dark energy in empty space that is used to explain the observed acceleration of space against the attractive effects of gravity (first observed in Type-Ia supernova). A cosmological constant has negative pressure, $P = -\rho c^2$, which contributes to the stress-energy tensor that according to the general theory of relativity, causes accelerating expansion. The fraction of the total energy density of our Universe (flat or almost flat) that is dark energy, Ω_Λ, is currently estimated to be 69% based on *Planck* satellite data [13]. Observations of the "flat" rotation curves of galaxies; the gravitational lensing of light by galaxy clusters; and enhanced clustering of galaxies indicate the existence of dark matter which cannot be accounted for by the quantity of observed luminous matter. Dark matter is described as being cold because its velocity is far less than the speed of light at the epoch of radiation-matter equality; non-baryonic (i.e. consisting of matter other than protons and neutrons); dissipationless since radiating photons can not cool it; and collisionless (i.e. the dark matter particles interact with each other and rest of the particles only through gravity. The dark matter component is currently estimated to constitute about 26.8% of the mass-energy density of the Universe. The remaining 4.9% comprises all ordinary matter observed as atoms, chemical elements, gas and plasma, the stuff of which visible planets, stars and galaxies are made. Also, the energy density includes a tiny fraction of $\sim 0.01\%$ of CMB photons, and not more than 0.5% in relic neutrinos. Although minimal today, these were much more important in the distant past, dominating the matter at $z > 3200$.

At the time of big bang, the Universe has a temperature of the order of 10^{32} K at the Planck epoch. This was immediately (within 10^{-33} to 10^{-32} seconds) followed by an exponential expansion of space by a scale multiplier of 10^{26} or more, known as cosmic inflation [14, 15]. Cosmic inflation solves the problems in standard cosmology such as flatness, horizon, entropy and magnetic monopole problems [16, 17, 18]. To explain the growth of gravitationally collapsed structures in the Universe, it is assumed that inflation in the early Universe generated density perturbations with a nearly scale invariant spectrum involving quantum mechanical fluctuations. The total energy of the Universe is conserved, and as it expands adiabatically, its temperature and energy density decreases. The early Universe remained hot (above 3000 K) for several hundred thousand years, a state that is detectable as the CMB, very low energy radiation emanating from all parts of the sky. The big bang scenario, with cosmic inflation and standard particle physics, is the only current cosmological model consistent with the observed continuing expansion of space, the observed distribution of lighter elements in the Universe (hydrogen, helium, and lithium), and the spatial texture of minute irregularities (anisotropies) in the CMB radiation.

1.2 CMB physics

Our Universe started to evolve from a dense and hot state after the big bang. Within the first second, baryonic matter formed, and later light elements started to form within a few minutes as Universe started to cool down and continue the expansion. At that time the

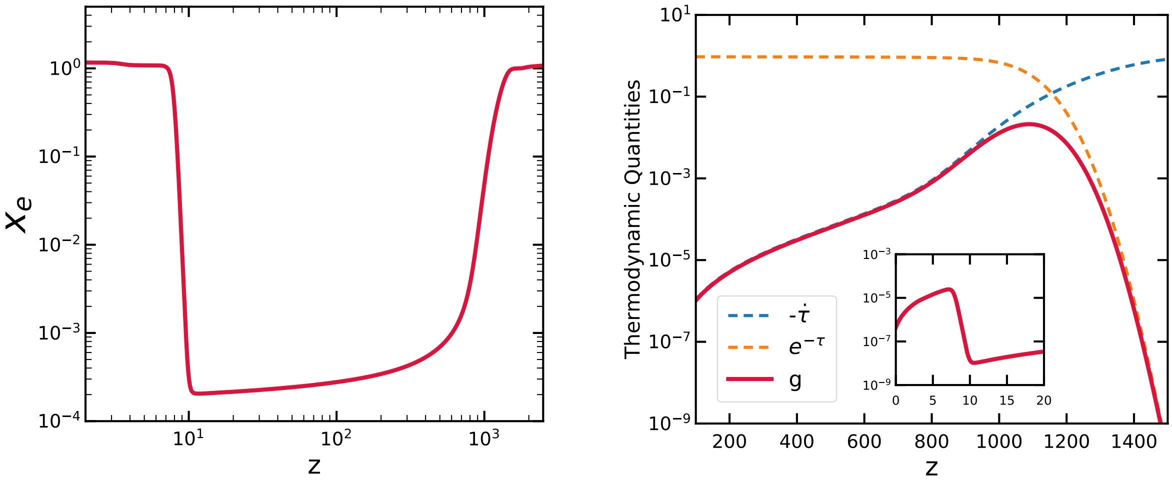

Figure 1.1: Left: This plot shows the evolution of ionization fraction. Right: We plot the evolution of thermodynamics quantities before and after the epoch of decoupling, $z_{dec} \sim 1100$. In the Inset, we show the visibility function at the low redshift range due to the reionization.

Universe can be considered as a soup of elementary particles. The main components of the Universe were electrons, protons, neutrons, neutrinos and photons. The free electrons scattered photons via Coulomb scattering. The binding energy of an electron to the nucleus of a hydrogen atom is 13.6 eV. The temperature of the Universe dropped down to 3000 K roughly 300000 years after the big bang. It provides sufficient conditions for a proton to capture an electron to form a hydrogen atom. This process is called recombination, and the time when recombination occurred is known as recombination epoch. Decoupling of photons occurs when the expansion rate of the Universe becomes larger than the scattering rate of photons by the electrons. At $z \sim 1100$, when neutral hydrogen atoms formed there were not many free electrons to scatter off photons. The Universe was essentially opaque but after decoupling photons are able to travel freely as they cease to interact with electrons. The surface where a photon scattered by an electron for the last time before reaching us is called the last scattering surface. The surface of last scattering surface is not really a three-dimensional surface; rather, it is a spherical shell with a thickness of around 90 Mpc. All the CMB experiments observe the photons coming from the last scattering surface, which describes the properties of the Universe when it was 380000 years old. As the Universe is expanding linearly since then the temperature of the CMB photons are scaling as $T = T_0(1+z)$, here T_0 is the present-day temperature of the radiation. Photon number density evolves as $n_\gamma = n_\gamma(0)(1+z)^3$ cm^{-3}, here $n_\gamma(0)$ is the number density of photons at $z = 0$. We express ionization fraction, $x_e(z)$ to quantify how the Universe made a transition from ionized to neutral phase. If we neglect the helium contribution to the ionization fraction, we can write $x_e(z) = n_e/(n_e + n_H)$, here n_e and n_H are the number density of electrons and the number density of neutral hydrogen. If $x_e \to 0$, the Universe is almost neutral and if $x_e \to 1$ it is almost ionized. The scattering rate, Γ, can be expressed in terms of the ionization fraction as $\Gamma = x_e(z)n_e\sigma_T$. In Figure 1.1 (left) we see Universe was almost fully ionized before the recombination epoch around $z_{rec} \sim 1100$ and after the decoupling, it gradually becomes neutral. The Universe remains in the neutral state until the high energy sources such as galaxies, and quasars ionized the intergalactic medium at the low redshift Universe. Due to the reionization process universe again become ionized, and ionization fraction reaches to its maximum value. If we know the scattering rate,$\Gamma(t)$, at time t, then we can quantify the number of scatterings a photon had experienced when the age of the Universe increased from t_1 to t_2. It can be represented by a dimensionless quantity know as optical depth which is

$$\tau(t) = \int_{t_1}^{t_2} \Gamma(t)dt = \int_{t_1}^{t_2} \sigma_T n_e(t)dt\,. \tag{1.2}$$

To understand the probability that a photon last scattered at conformal time η, is defined by the visibility function, $g(\eta)$. It is written as

$$g(\eta) = -\dot{\tau(\eta)}e^{-\tau(\eta)}\,. \tag{1.3}$$

Visibility function can be interpreted as the probability density as it satisfies, $\int_0^{\eta_0} g(\eta)d\eta = 1$. In Figure 1.1 we showed the evolution of three thermodynamic quantities such as $-\dot{\tau}$, $e^{-\tau}$ and g separately. τ is very large in the early Universe so, $e^{-\tau}$ term tends to zero, and hence the visibility function also tends to zero, meaning that the probability that a photon will scatter is essentially zero. The visibility function reaches its maximum at the time of decoupling in which the probability of the last scattering is higher. Most of the CMB photons decoupled at redshifts where the visibility function peaks. After recombination, the visibility function falls gradually as τ becomes smaller.

We observe the CMB photons which are coming from the last scattering surface. After the recombination, the Universe consists mainly of the hydrogen gas (neglecting helium and other heavy elements), photons, neutrinos and dark matter. Baryons are free to collapse for gravity as there is no pressure exerted by photons. Later, structures in the Universe formed due to the gravitational instability.

1.3 Frequency Spectrum of the CMB

The intensity spectrum of the CMB is expected to follow Planck's law of radiation as the early Universe was in thermal equilibrium. Before the recombination epoch, radiation component interacted with the matter sector mainly by Compton, double Compton, Coulomb scattering and thermal bremsstrahlung. Any source of energy injection in the early Universe may change the spectral shape of the CMB if the time needed for thermalization is longer than the timescale before decoupling. Blackbody spectrum will remain unchanged till $z \gtrsim 2 \times 10^6$ due to the Compton scattering, double Compton scattering and the bremsstrahlung processes [19, 20, 21].

In Compton scattering, a photon scatters off by an electron, and a fraction of photon's momentum and energy are being transferred to the recoil electron. Bose-Einstein (BE)

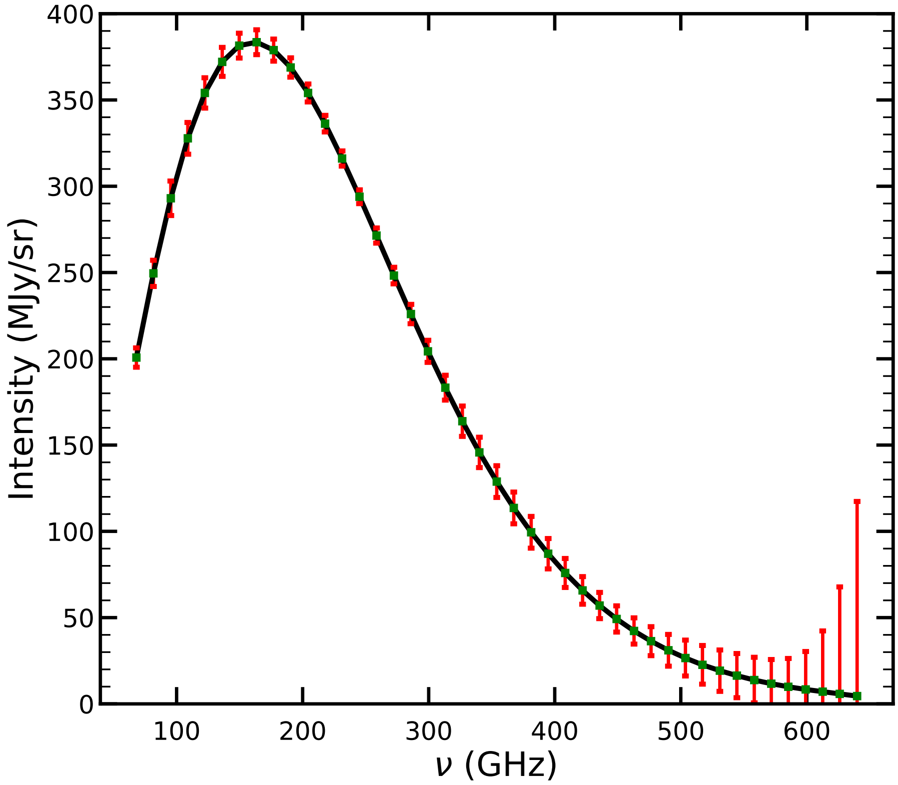

Figure 1.2: Blackbody spectrum of CMB measured by the COsmic Background Explorer (COBE) satellite [22]. The error bars are 400 times larger than the original ones just for the visual purpose. We used data from NASA Lambda data product website (https://lambda.gsfc.nasa.gov/product/cobe/).

spectrum could be created by the Compton scattering. The BE distribution function is expressed as

$$f_{\rm BE} = \frac{1}{e^{h\nu/k_B T + \mu} - 1}\,. \tag{1.4}$$

Here, $k_B = 1.38 \times 10^{-23} J/k$ is Boltzmann constant. μ is the chemical potential, which is the energy released or absorbed due to the change in the number of particles. Compton scattering conserves the total number of photons but redistributes the photon's energy in different frequencies. Bremsstrahlung is a process in which the energy is released when the electromagnetic field of an ion decelerates an electron and can be expressed as $e^- + I \to e^- + I + \gamma$. For the double Compton scattering, it produces another extra photon via $e^- + \gamma \to e^- + \gamma + \gamma$. On the other hand, double Compton scattering and Thermal bremsstrahlung can not create spectral distortions in CMB below $z \lesssim 10^7$ [19, 23, 24].

The expansion of the Universe does not change the blackbody spectrum as temperature and frequency both scales with the $(1 + z)$ factor by keeping $e^{h\nu/kT}$ fixed. Any energy injection happens in the early Universe at $z \gtrsim 10^5$, and Compton scattering will redistribute the photon's energy as a Planckian spectrum. Otherwise, if the energy injection happens at $z \lesssim 10^5$, there will be a spectral distortion in CMB from its blackbody spectrum.

The spectrum of CMB perfectly follows the black body radiation. The temperature of CMB is very close to 2.7255 K, which is across the whole sky. It was first measured by the space mission COBE [22], see Figure 1.2. The Far Infrared Absolute Spectrophotometer (FIRAS) instrument in the COBE satellite measured the peak of the blackbody spectrum very precisely. In the high frequency errorbars increase due to the residual foreground contamination from the interstellar dust.

Spectral distortion in CMB can be categorized into y-type and μ-type distortion (Sometimes the intermediate distortion is called as i-type. See [25] for more details). Double Compton scattering and Bremsstrahlung processes are efficient enough to create low energy photons in the redshift range $2 \times 10^6 \gtrsim z \gtrsim 10^5$. Compton scattering is not efficient enough to redistribute the low energy photons to high energy end. Therefore, the blackbody spectrum will not be preserved, and μ distortion will leave its imprint. The Bose-Einstein distribution function describes this spectrum with a frequency dependent chemical potential following equation 1.3. The current upper limit of the chemical potential is $|\mu| \lesssim 9 \times 10^{-5}$ with 95% confidence [26].

If energy injection happened anytime at $z \lesssim 5 \times 10^5$, the Universe could not be thermalized by the Compton scattering, and rather hot electrons will up-scatter the CMB photons. It is known as y-type distortion. The current upper limit of y parameter is $|y| \lesssim 1.5 \times 10^{-5}$ with 95% confidence [26]. We will discuss more y distortion due to Sunyaev Zeldovich effect in Section 1.5.5.

Spectral distortion in CMB is a powerful probe to understand several physics in the early Universe. There could be several sources which can inject energy and leave the spectral signature in the CMB. Energy injected in such events as evaporation of primordial black holes, the decay of cosmic strings, the decay of Sterile neutrinos and primordial magnetic fields can in principle distort the blackbody spectrum of CMB [27, 28, 29, 30, 31].

Future proposed space-based CMB experiments such as *PIXIE*, *PRISM* and *PRISTINE* aim to put constraints on μ and y distortions at the level $\mu \lesssim 5\times10^{-8}$ and $y \lesssim 10^{-8}$ respectively [32, 33].

1.4 Primary Anisotropies

Primary anisotropies are usually defined in terms of processes occurring at last scattering. In this Section we give the necessary definitions of quantities and probes which are relevant for the rest of the Thesis, for temperature and linear polarization.

1.4.1 Temperature Anisotropies

The quantum fluctuations generated during the time of inflation put distinct signatures in the CMB sky, at the level $\Delta T/T_0 \sim 10^{-5}$, on the top of the mean temperature of CMB at present, $T_0 \sim 2.7255$ K. Let the temperature at a point on the CMB sky in the direction $(\theta,\, \phi)$ be $T(\theta, \phi)$. In spherical co-ordinate system we can average over all the directions as

$$\langle T\rangle = \frac{1}{4\pi}\int T(\theta,\phi)\sin\theta d\theta d\phi = T_0\,. \tag{1.5}$$

Since the temperature fluctuations are defined on the surface of the sphere, we decompose it in spherical harmonics as

$$\frac{\Delta T}{T_0}(\theta,\phi) = \sum_{\ell m} a_{\ell m} Y_{\ell m}(\theta,\phi)\,. \tag{1.6}$$

Here T_0 is the mean temperature of the CMB, $Y_{\ell m}(\theta,\phi)$ is the basis vector in the spherical harmonic system and $a_{\ell m}$ is the coefficient of the temperature. As temperature is a real field it follows: $a^*_{\ell m} = (-1)^m a_{\ell -m}$. The fluctuations are generated from a Gaussian random field, and hence the statistics of the temperature fluctuations should be predictable by any cosmological model. This statistics should also be independent of the position in space. With these conditions, we can write:

$$\langle a^X_{\ell m} a^{X*}_{\ell' m'}\rangle = \delta_{\ell\ell'}\delta mm' C^X_\ell\,. \tag{1.7}$$

C_ℓ is known as power spectra. C^X_ℓ carries all the statistical information of the field X. Power spectra for the true field can be defined as:

$$\widehat{C}^X_\ell = \frac{1}{2\ell+1}\sum_m |a_{\ell m}|^2\,. \tag{1.8}$$

This is an unbiased estimator as it follows $\langle \widehat{C_\ell}^X = C^X_\ell$. The chi-square distribution will have $2\ell+1$ degrees of freedom, which can not be avoided as we have only one observable Universe. This criterion will lead to

$$\left(\Delta\widehat{C}^X_\ell\right)^2 = \frac{2}{2\ell+1}C^2_\ell\,. \tag{1.9}$$

This statistical uncertainty for the measurement of the angular power spectrum is known as "cosmic variance". All the models aim to explain the early universe physics should be able to explain the temperature fluctuations in the CMB at the recombination epoch. We will review below the techniques to predict the fluctuations in the CMB sky theoretically.

The CMB temperature power spectrum can be numerically computed by the Line Of Sight integration (LOS) method first prescribed by [34]. In this method, CMB temperature fluctuations are described by the time integral of the product of the geometrical factor and the source term. Source term accounts all the physics at the time of recombination, but the geometrical term is the radial transfer function which does not depend on the physics at the recombination. Transfer function describes the evolution of the initial Newtonian curvature. Temperature fluctuations can be expressed as:

$$C^{TT}_\ell = 4\pi\int k^2 dk |\Theta^T_\ell(k,\eta_0)|^2 \mathcal{P}_{\mathcal{R}}(\mathrm{k})\,. \tag{1.10}$$

$\mathcal{P}_{\mathcal{R}}(\mathrm{k})$ is the initial curvature power spectrum and $\Theta_\ell^T(k,\eta_0)$ is the transfer function of photons which is related to the source function as

$$\Theta_\ell^T(k,\eta_0) = \int_0^{\eta_0} d\eta S_T(k,\eta) j_\ell \left[k(\eta_0-\eta)\right] . \tag{1.11}$$

We use the Cosmic Linear Anisotropy Solving System (CLASS) code to calculate CMB power spectra [35, 36]. The source term can be calculated separately for the each effect as

$$S_T(k,\eta) = S^{\mathrm{Dp}}(k,\eta) + S^{\mathrm{ISW}}(k,\eta) + S^{\mathrm{SW}}(k,\eta) + S^{\mathrm{sec}}(k,\eta) . \tag{1.12}$$

The superscripts Dp, SW and ISW in the R.H.S denote the source function for the Doppler, Sachs-Wolfe and integrated Sachs-Wolfe effects. The first one is caused by photons emitted by electrons having a non-zero peculiar velocity in the direction of the emission. The SW effect is due to the redshift or blueshift on photons caused by gravitational perturbations at last scattering. The ISW is the same metric effect but caused by the evolution of the gravitational perturbations along the line of sight. In addition to the ISW, additional anisotropies are introduced in CMB when photons travel from the last scattering surface to us. $S^{\mathrm{sec}}(k,\eta)$ is the source function for those secondary anisotropies. We discuss these in details in Section 1.5.

In Figure 1.3, we show the temperature power spectrum in different angular scales, which we briefly describe now. Before the recombination, baryons and photons were tightly coupled to each other. Perturbations in dark matter density were growing with time due to gravity, influencing the photon-baryon fluid competing with radiative pressure, causing acoustic oscillations on sub-horizon scales. The horizon size at the last scattering surface subtends an angle which is about 1° ($\ell \sim 180$). Perturbations on scales larger than the horizon size on the last scattering are not affected as they are causally disconnected. As a result of this phenomenology, the power spectrum between $100 \leq \ell \leq 1000$ exhibits oscillations, making the last scattering surface a snapshot of the perturbations in different phases through photons. At $\ell \gtrsim 1000$, CMB photons diffuse from overdensity regions to small scales, leading to exponential damping of the temperature power on small scales.

1.4.2 Polarization Anisotropies

As we anticipated, CMB photons are expected to be polarized due to the Thomson scattering with electrons. The magnitude of the polarization of the scattered radiation is proportional to the magnitude of the quadrupole of the radiation incident on the scattering electron. The orientation of the quadrupole determines the orientation of the polarization.

We use Stokes parameters to describe the state of polarization of an electromagnetic wave. I denotes the total intensity of CMB photons. Q and U are used to express the linear polarization and V for the circular polarization. I is invariant under any rotation, but Q and U transforms under the rotation angle, ϕ, along the axis perpendicular to the wave, as

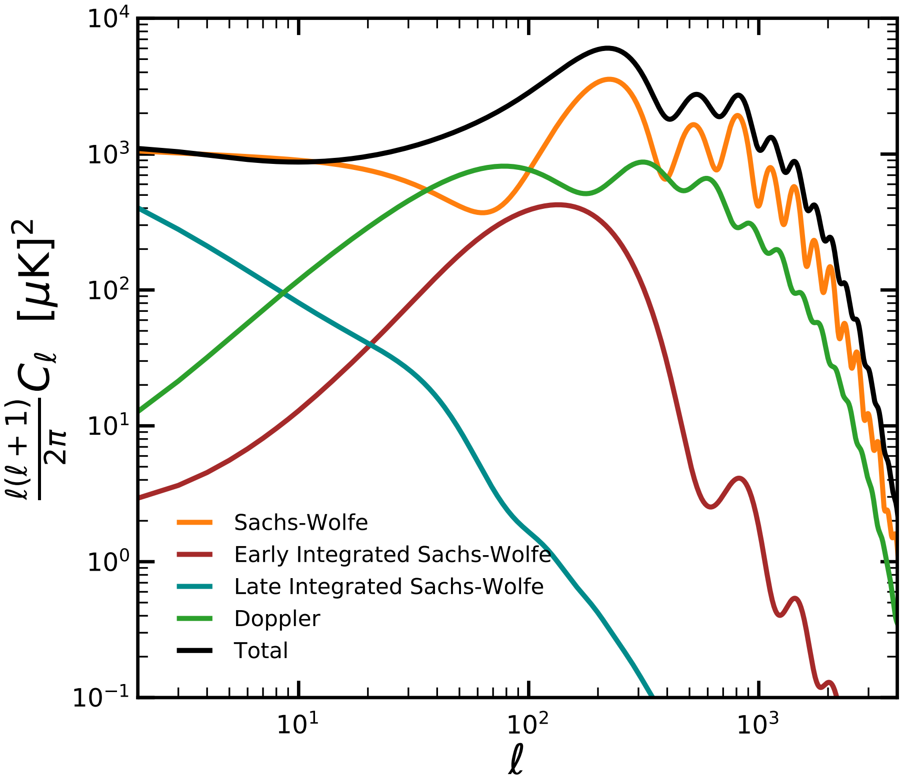

Figure 1.3: We show the contributions of scalar perturbations due to SW, Early-time and late-time ISW and doppler effects. We use cosmological parameters for the flat *Lambda* CDM model described in [13]. This figure has been produced using CLASS code [1][35]

$$Q' = Q\cos(2\phi) + U\sin(2\phi), \tag{1.13}$$

$$U' = -Q\sin(2\phi) + U\cos(2\phi). \tag{1.14}$$

Q and U are the spin two fields. They depend on the choice of a coordinate system. In the complex plane, Q and U transform as

$$(Q \pm iU)'(\hat{\mathbf{n}}) = (Q \pm iU)e^{\mp 2i\phi}(Q \pm iU)\,. \tag{1.15}$$

In terms of spherical harmonics, we have:

$$(Q \pm iU)(\hat{\mathbf{n}}) = \sum a_{\pm 2,\ell m} Y_{\pm 2,\ell m}\,. \tag{1.16}$$

We can now decompose the tensor field in terms of gradient and curl components as

$$a^E_{\ell m} = -\frac{1}{2}\left(a_{2,\ell m} + a_{-2,\ell m}\right)\,, \tag{1.17}$$

$$a^B_{\ell m} = \frac{i}{2}\left(a_{2,\ell m} - a_{-2,\ell m}\right)\,. \tag{1.18}$$

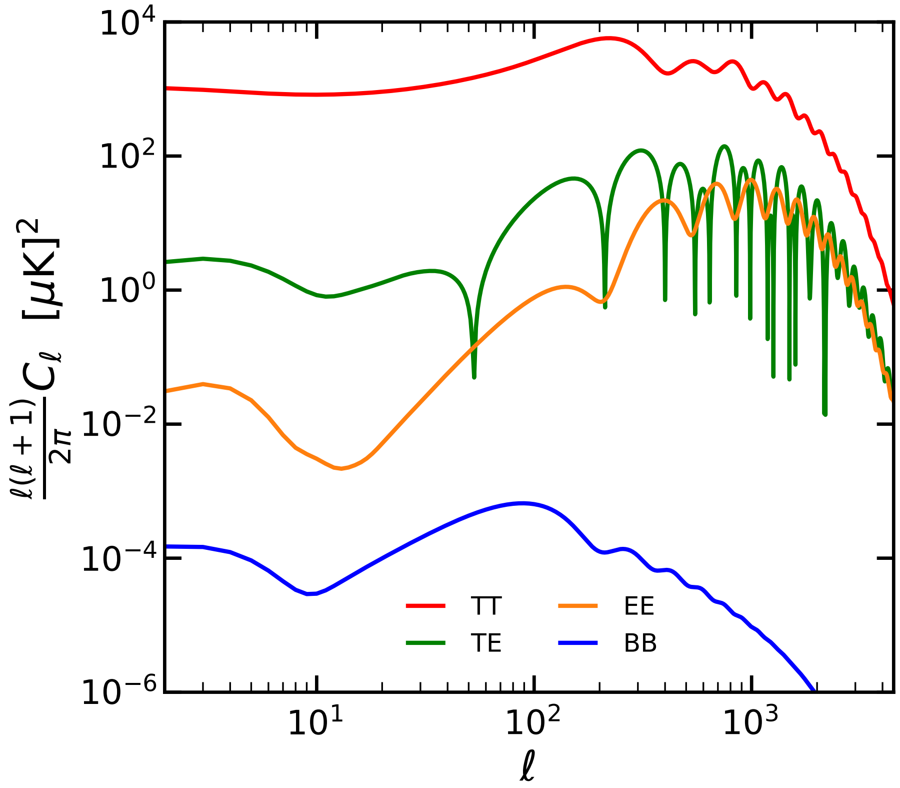

Figure 1.4: CMB temperature, E-mode, B-mode and $T-E$ cross power spectra. We used cosmological parameters derived from the combination of *Planck* TT, TE, EE, LowP+Lensing+Ext [13], see Section 1.7. The B-mode power spectrum is shown for $r = 0.01$ and all the polarization power spectra assumed reionization with $\tau = 0.054$.

E modes remain invariant under the parity transformation but B modes changes its sign. In principle, we can construct the six power spectra such as C_ℓ^{TT}, C_ℓ^{EE}, C_ℓ^{BB}, C_ℓ^{TE}, C_ℓ^{EB}, C_ℓ^{TB}. As E and T changes opposite way than B under the parity transformation, due to the parity conservation, the cross power spectrum of EB and TB becomes zero.

In figure 1.4 we show all the theoretical primordial temperature, E-mode, B-mode and TE power spectra for the indicated Cosmology. Oscillations in the EE and TE power spectra are due to the oscillations in the photon-baryon fluid inside the gravitational potential well and are originated by acoustic oscillation in T, which we described in the previous Section. The polarization signal arises from the gradient of the peculiar velocity (v_γ) of the photon fluid. Hence, the peak of the EE power spectra is opposite phase with respect to TT. The correlations between density and velocity perturbations on the last scattering surface can be both positive and negative. The TE power spectrum is primarily the product of the monopole terms for temperature and the velocity, and its oscillation frequency is twice with respect to TT and EE. The bump at large scale ($\ell \lesssim 10$) in polarization and TE power spectra are due to the reionization. Reionization produces free electrons along the path of CMB photons and a late stage Thomson scattering epoch. The large scale polarization increases with an increase of τ and therefore the measurement of the large scale CMB polarization is a unique probe of the reionization optical depth. As it can be seen in the Figure, the shape of the BB spectrum is quite different; we discuss the associated main phenomenology in the next Section.

1.4.3 B-mode phenomenology and scientific relevance

The basic prediction of Inflation are the following: (i) the Universe should be flat, i.e. $\Omega_k \sim 0$, (ii) the primordial scalar perturbations should be Gaussian, adiabatic and characterized by a nearly scale-invariant spectrum, (iii) the perturbations are correlated on scales larger than the Hubble horizon, (vi) primordial gravitational waves due to the tensor perturbations during inflation are also generated, Gaussian, and with a power law whose slope is related to the scalar one. The primordial B-mode signal sourced by cosmological gravitational waves is still undetected. E modes are generated due to both tensor, vector and scalar perturbations but finding the signature of tensor perturbations in E modes is complex due to the dominance of the contribution from density. As we describe now, the B-mode of CMB polarization is an unique signature for inflationary gravitational waves. As we will see later, future CMB experiments are set up to detect the primordial gravitational waves till the ultimate limit of $r = 0.001$.

For simple model of inflation, let ϕ be the scalar field in the early Universe and $V(\phi)$ the inflationary potential. In the FRLW space-time we can write the equation of motion and Friedmann equation as [37]

$$\ddot{\phi} + 3H\dot{\phi} + V'(\phi) = 0\,, \tag{1.19}$$

$$H^2 = \left(\frac{\dot{a}}{a}\right)^2 = \frac{V(\phi) + \frac{\dot{\phi}^2}{2}}{3m_P^2}\,. \tag{1.20}$$

Where m_P is the Planck mass. We can define the slow roll parameter,$\epsilon = -\dot{H}/H^2$. The standard picture of inflation has $\epsilon \ll 1$. If $H^2 \propto V$ holds during the inflation then we can find that the tensor-to-scalar ratio, r, is defined in terms of the inflaton potential as

$$r = 16\epsilon = \left[0.1 \times \frac{V}{(2 \times 10^16\ \mathrm{GeV})^4}\right]\,. \tag{1.21}$$

For the power law potentials such as ϕ, ϕ^2, $\phi^{2/3}$, the 3σ bound on r is 0.057, 0.038 and 0.028 respectively [38, 39]. Whereas for well-known Starobinsky's R^2 (R represents Ricci scalar)inflationary model the constraion on r is $\gtrsim 6 \times 10^{-4}$ [40, 41]. As we will see in the last Section of this Chapter, these values are the target of future B-mode experiments.

Primordial gravitational waves creates quadrupole anisotropies in the CMB. Their amplitudes remain unchanged for scales larger than the horizon size, but oscillate and decay on smaller scales. At the same time, there is no time from photons de-coupled on scales larger than the horizon to reach last scattering. This phenomenology makes the

B-modes from primordial gravitational waves to appear like a peak in the spectrum at about $\ell \sim 80$, which is about the scale of the horizon during recombination, see Figure 1.4. A second scattering, occurring at the epoch of reionization, is able to boost the B-mode power from inflationary gravitational waves from larger scales, generating the so called reionization bump at $\ell \simeq 20$, also evident in Figure 1.4.

Hence, detection primordial B-mode signal will be the final confirmation of inflation. Not only that, but it will also be able to distinguish between different inflationary models which will provide us with the fundamental physics in the early Universe. If r is smaller than the current upper limit (0.06), the detection will be a very challenging task. Outstanding challenhes are represented for example by the foreground emissions, and also the need to separate the secondary B-modes which can contaminate the primordial B-mode signal. We will discuss the effects of foreground in Section 1.6.

1.5 Secondary Anisotropies

Secondary anisotropies are those imprinted on CMB photons after last scattering. We review their basic definitions and phenomenology here.

1.5.1 Integrated Sachs Wolfe effect

It can be seen that if the Universe is dominated by matter, then the large scale gravitational potentials do not evolve significantly, but when radiation or dark energy dominate they will evolve significantly. The energy of photons will change due to the phase transition of the Universe from radiation to the matter-dominated phase. The ISW signal was first detected by performing the cross correlation of Wilkinson Microwave Anisotropy Probe (WMAP) first-year data with the number count of radio galaxies from the NVSS data and HEAO1 A1 X-ray data [42].

Thus, the ISW has contributions from the early and late time Universe. The first occurrence is due to the fact that the Universe is not entirely matter dominated at the last scattering surface. Potentials change with time when the Universe made a transition from the radiation to matter domination era. Non-negligible radiation pressure leads to the decay of the gravitational potential of perturbations which enter the horizon immediately after the last scattering. The main early ISW contribution comes from this decay of gravitational potential just after recombination. This is known as early ISW. On the other hand, at present, we are living in the dark energy dominated Universe. The gravitational potentials decay when the Universe becomes dark energy dominated after the matter-dominated era. Anisotropies generated due to this effect is referred to as late time ISW effect.

In Figure 1.3, we show the temperature power spectra due to the early and late ISW. Late time ISW is dominant on the large scales as the horizon size is larger at low redshifts where dark energy dominates. Late time ISW could be a clean probe of dark energy or modified gravity. However, It is a difficult task to separate the ISW contribution from the primary temperature anisotropies. ISW effect has imprinted on the large scale structures and cross correlated signal of CMB and galaxy surveys is a probe of ISW effect.

1.5.2 Rees Sciama Effect

Non-linear integrated Sachs Wolfe effect is sometimes known as Rees Sciama (RS) effect. RS effect is the fluctuation in temperature in CMB caused by the time dependence of the gravitational potential inside a non-linear structure. [43] first introduced the explanation of non-linear clustering on the CMB in 1968. The fluctuations due to the RS effect is very hard to detect, but it can be calculated using N-body simulations. The RS effect from a typical distribution of non-linear object was established to be at most 10^{-6} [44]. If the photon crossing time for a particular evolving structure is an appreciable fraction of the non-linear structure evolution time scale, the blueshift gathered by each photon will not be compensated by the corresponding redshift. As an outcome, there will be a net change in the temperature of CMB photon. For $\Omega_0 = 1$ the RS effect expected to scale with structure and the void site as follows [44]

$$\frac{\Delta T}{T} = \left(\frac{\delta\rho}{\rho}\right)^{\frac{3}{2}} d^3(1+z)^{\frac{9}{2}} \,. \tag{1.22}$$

Here $\frac{\delta\rho}{\rho}$ is the density contrast of the void or structure at the redshift z and d is the physical size of the object. The proper motion of the cluster and ρ supercluster also contributes on the temperature fluctuation in CMB [45].

1.5.3 CMB lensing

Photons propagate from one point to another point following spacetime geodesics, which is the shortest distance between those two points. The general theory of relativity predicts that the path of the light will be bent if photons experience the presence of the gravitational field. Massive objects in the Universe, such as galaxy clusters, but also unprocessed density perturbations on scales of hundred of Mpc have a surrounding gravitational field. In their way from the last scattering to us, photons get deflected due to the gradient of the gravitational field. This effect changes the photon distribution along the line of sight and modifies their statistics, becoming non-Gaussian, and their angular distribution as well. CMB lensing has some unique features in the temperature and polarization power spectra, as we summarize below. If a CMB photon is deflected with an angle, α, it can be expressed with the lensing potential, $\phi(\hat{\mathbf{n}})$ [46, 47].

$$\alpha = -2\int_0^{\chi_*} d\chi \frac{f_K(\chi_* - \chi)}{f_K(\chi_*) f_K(\chi)} \phi(\chi\hat{\mathbf{n}}; \eta_0 - \eta) \,. \tag{1.23}$$

The lensing potential can be expanded into spherical harmonics as

$$\Phi(\hat{\mathbf{n}}) = \sum_{\ell m} \phi_{\ell m} Y_{\ell m}(\hat{\mathbf{n}}) \,. \tag{1.24}$$

We can now construct lensing potential power spectra as $\langle < \phi_{\ell m}\phi_{\ell' m'}\rangle = \delta_{\ell\ell'}\delta_{mm'}C_\ell^{\phi\phi}$. CMB generates non-Gaussianity by correlating different modes. We can write the correlation function for the temperature and polarization field as:

$$\langle X(\boldsymbol{\ell_1})X'(\boldsymbol{\ell_2})\rangle = f_\phi(\boldsymbol{\ell_1},\boldsymbol{\ell_2}))\phi(\boldsymbol{L})\,. \tag{1.25}$$

Here X and X' are the different combinations of T, E and B and $\boldsymbol{L} = \boldsymbol{\ell_1}+\boldsymbol{\ell_2}$. The coupling factor, $f_\phi(\boldsymbol{\ell_1},\boldsymbol{\ell_2}))$ is the correlation function which depends on the unlensed power spectra. Even the unlensed power spectra is statistically isotropic but for a given ϕ power spectra, isotropy breaks in the observed lensed CMB. Using the non-Guassianity in the lensed CMB, the lensing potential power spectra can be reconstructed by applying a quadratic estimator [46, 46, 48, 49, 50]. CMB lensing is a powerful tool to understand the large scale distribution of dark matter. *Planck* has detected the lensing signal with 5σ using only polarization and combined with the temperature data, the detection is at the level of 40σ. Lensing amplitude has degeneracies with the other cosmological parameters such as τ, $\sum m_\nu$, H_0 and Ω_b, dark energy and modified Gravity. Thus, precision measurement of CMB lensing constrain these cosmological parameters.

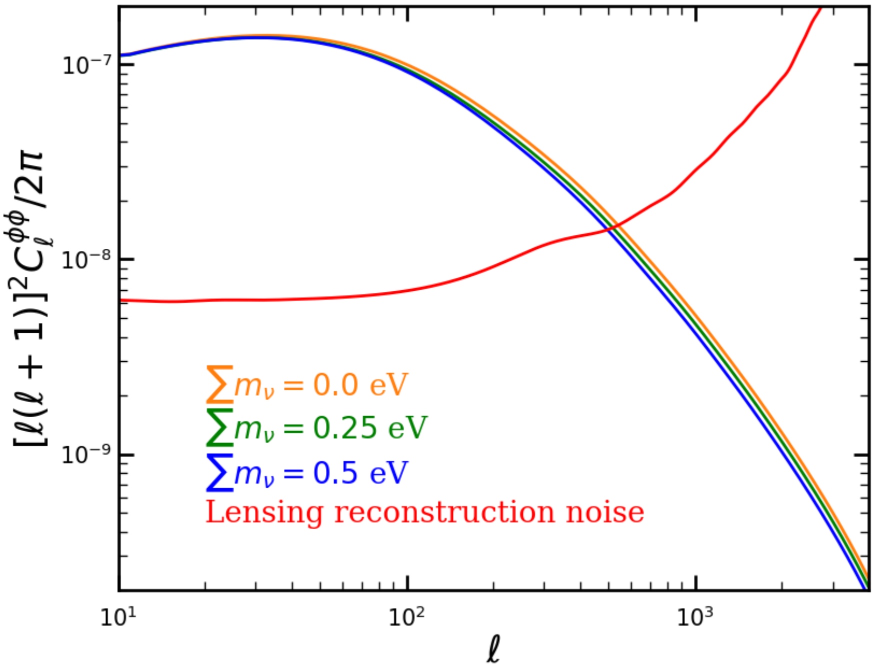

Figure 1.5: Power spectra of the lensing potential showing the effects of the neutrino masses. Lensing reconstruction noise is calculated using *Quicklens* code (https://github.com/dhanson/quicklens) using specifications from future B-mode satellite measurements.

As an illustration, Figure 1.5 shows the effects of the neutrino mass on the lensing potential power spectra. The shape of the lensing power spectrum is due to the convolution between the background CMB anisotropies and the LSS lenses distributed across redshift. Increase of the neutrino mass suppresses the lensing effect at $\ell \gtrsim 60$. We show the reconstruction noise for an experiment with 1μK-arcmin sensitivity in temperature and 1 arcmin beam size. Future experiments such as CMB-bharat and PICO will have similar lensing reconstruction noise [51, 52]. As we will see in the last Section, future experiments such as Simons Observatory will constrain the neutrino mass, $\sigma\left(\sum m_\nu\right) = 33$ Mev using CMB and LSS datasets [53, 54].

1.5.4 Ostriker-Vishniac effect

Scattering of CMB photons from ionized gas clouds will contribute to anisotropies at an higher order perturbation theory. This effect is called Ostriker Vishniac (OV) effect [55]. The measurements of fluctuations in CMB is highly sensitive to the cosmological parameters and also the model of reionization history. Doppler anisotropies are suppressed at the small scales, but non-linear perturbations become important at those scales. OV generates non-Gaussianity in CMB by coupling modes between velocity and free electron density fields. The predicted anisotropy of typical cold dark matter models is at about 50 μK at arc minute scale. [56].

1.5.5 Sunyaev Zel'dovich effect

CMB photons get scattered off by the hot electron gas present in the galaxy clusters and intercluster medium via inverse Compton effect [57, 58]. This process creates spectral distortion in the CMB (y-type) and also generates additional temperature fluctuations [59]. Considering different physical processes, we can broadly categorize the SZ effect into i) the Thermal Sunyaev Zeldovich (tSZ) ii) Kinetic Sunyaev Zeldovich (kSZ) and the iii) relativistic Sunyaev Zeldovich (rSZ) effect, as we briefly describe now.

Kinetic SZ Effect

If we consider the rest frame of CMB photons as a reference frame then the galaxy clusters are moving with respect to that frame. Hence, additional frequency distortion will be introduced due to the cluster bulk velocity.[60]. This frequency distortions result in temperature fluctuation in CMB, which is referred as kinetic SZ effect [61, 62]. If the component of cluster velocity along the line of sight is v_p, then the temperature fluctuation in the non-relativistic limit ($v_p \ll c$) is given as [63]

$$\frac{\Delta T_{\mathrm{kSZ}}}{T_0} = -\tau_e \left(\frac{v_p}{c}\right) , \tag{1.26}$$

where $\tau_e = \sigma_T \int n_e d\ell$, is the optical depth of cluster. The change in CMB spectral intensity due to the kSZ effect is given as [64]

$$\frac{\Delta I_\nu}{I_\nu} = -\tau_e \beta_l \frac{x e^x}{e^x - 1} . \tag{1.27}$$

Here, $x = h\nu/K_bT$ and $\beta_l = v_p/c$. As the clusters subtend a small angle in the sky, we can write the kSZ power spectrum under the Limber approximation. The kSZ power spectrum is given by [65, 66]

$$C_\ell^{kSZ} = \int dz Q(z) \langle v_p(z)^2 P_e \rangle \left(\frac{\ell}{\chi(z)}, z \right) , \tag{1.28}$$

where $\langle v_p(z)^2 \rangle$ is the mean square velocity along the line of sight and $P_e(k, z)$ is the power spectrum of free electrons. The function $Q(z)$ is

$$Q(z) = T_0^2 \frac{H(z)}{\chi(z)^2} \left(\frac{d\tau_e}{dz} \right) e^{-2\tau(z)} . \tag{1.29}$$

The Atacama Cosmology Telescope detected the kSZ signal for the first time [67]. They measured a non zero mean pairwise momentum of the clusters from the kSZ signal. Future CMB experiments will precisely measure the kSZ signal, which will become an independent cosmological probe. For example, the kSZ signal has the potential to constrain the dark energy and modified gravity [68, 69, 70]. The kSZ signal has two sources; i) from the galaxy clusters at low redshifts (the late-time kSZ); ii) From the ionized bubbles during the epoch of reionization (the early-time kSZ). It is very difficult to characterize the kSZ signal from the primary CMB, tSZ and the point sources. A telescope such as CCAT-prime with many frequency channels will be able to separate the foregrounds sufficiently to have a clean measurement of the direct kSZ signal [71]. The precise measurement of the kSZ would be able to break the degeneracy between the optical depth and the radial velocity of the cluster. The radial velocity of galaxy clusters and the shape of the kSZ signal could act as an alternative probe for studying the growth of the structures and expansion history of our Universe.

Thermal SZ Effect

Thermal SZ effect occurs when CMB photons interact with hot, high energy electrons inside the galaxy clusters by inverse Compton scattering [59]. When CMB photons pass-through of the massive cluster, it has only 1% probability of interacting with an ICM electron. An important property of the tSZ effect is that it is independent of the redshift of the galaxy cluster. If a cluster atmosphere contains electron gas with density $n_e(\overline{r})$, the scattering optical depth τ_e, Comptonization parameter y and x-ray spectral brightness b_X are given by [72]

$$\tau_e = \int n_e(\overline{r}) \sigma_T dl , \tag{1.30}$$

$$y = \int n_e(r) \sigma_T \frac{K_b T_e(r)}{m_e c^2} dl , \tag{1.31}$$

$$b_X(E) = \frac{1}{4\pi(1+z)^3} \int n_e(r)^2 \Lambda(E, T_e) dl \,, \tag{1.32}$$

where z is the redshift of the cluster, Λ is the spectral emissivity of the gas at observed X-ray energy E. Let x be the ratio of photon energy to the electron energy, expressed as, $x = \frac{h\nu}{K_b T_e}$. Inverse Compton effect can be simplified considering two cases: when $h\nu << K_b T_e$ and $h\nu >> K_b T_e$. But for the intermediate case we need to use Kompaneets equation, which can be written as [73]

$$\frac{dN}{dy} = \frac{1}{x^2} \left[x^4 \left(\frac{dN}{dy} + N + N^2 \right) \right] . \tag{1.33}$$

N is the photon occupation number given by Bose-Einstein (BE) distribution,

$$N = \frac{1}{e^{\frac{h\nu}{K_b T}} - 1} .$$

We can solve the Kompaneets equation for $h\nu \ll K_b T_e$ ($x \ll 1$) case, implying

$$-2y = \ln \frac{N'}{N} . \tag{1.34}$$

$N' = N + \delta N$ is the photon occupation number after passing through the cluster. Since the observed amount is very small, we can Taylor expand $\ln N'/N$ and get

$$-2y = ln \left(\frac{N + dN}{N} \right) = ln \left(1 + \frac{dN}{N} \right) \approx \frac{dN}{N} . \tag{1.35}$$

Since $N = \frac{1}{e^x - 1} \approx \frac{1}{x} = \frac{K_b T}{h\nu}$. We have

$$\frac{dn}{N} \approx \frac{dT}{T} = -2y \,, \tag{1.36}$$

which finally reduced to

$$\frac{\Delta T}{T} = -2 \frac{K_b \sigma_T}{m_e c^2} \int n_e T_e dl \,. \tag{1.37}$$

In Figure 1.6, we show the frequency dependence of tSZ. We observe that at low frequency, $\nu \lesssim 220$, we will observe galaxy clusters appearing as black spots in CMB map, but if we observe at high frequencies, $\nu \gtrsim 220$, those points will look brighter than the mean CMB temperature. Many galaxy clusters are detected through the tSZ effect by CMB experiments such as South Pole Telescope[2] (SPT) [74], Atacama Cosmology Telescope[3] (ACT) [75] and *Planck* [13].

---

[2] `https://pole.uchicago.edu/`

[3] `https://act.princeton.edu/`

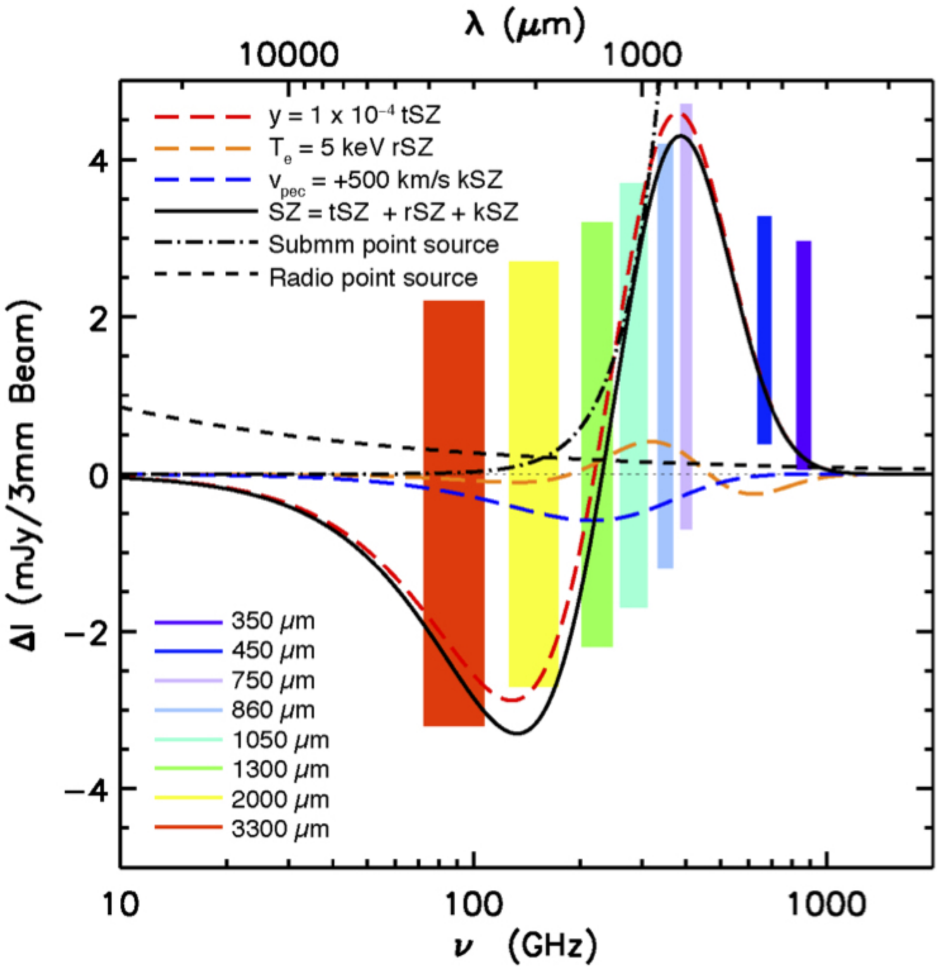

Figure 1.6: Predicted tSZ, kSZ and rSZ signal. This picture is taken from the Cerro Chajnantor Atacama Telescope (CCAT-p) website (http://www.ccatobservatory.org/). The parameters used for the simulation is described in [76].

Relativistic SZ Effect

The calculations of temperature fluctuations due to the SZ effect are correct when $K_bT_e << m_ec^2$. If the temperature of electrons is higher, one should include the relativistic corrections in the Kompaneet's equation. One can expand the Kompaneet's equation in powers of $x = KT_e/m_ec^2$. This correction makes the calculations of the temperature fluctuations very complicated but numerically solvable. This has been addressed by many studies, and yet the rSZ signal is not detected [77, 78, 79, 80, 81]. The spectral distortion due to the the relativistic SZ effect can be expressed as [82]

$$I_\nu^{\rm tSZ,rel}(\hat{\mathbf{n}}, M, z) = g_\nu y(\hat{\mathbf{n}}, M, z) + g_\nu \delta_\nu^{\rm rel}(\hat{\mathbf{n}}, T_e) y(\hat{\mathbf{n}}, M, z)\,. \tag{1.38}$$

Here, $\delta_\nu^{\rm rel}$ is the additional distortion term which depends on the gas temperature of the cluster, T_e. g_ν is the spectral function of tSZ, which can be writen as [82]

$$g_\nu = \frac{(2K_BT_0)^3}{(hc^2)} \frac{x^4e^x}{(e^x-1)^2} \left[x \coth\left(\frac{x}{2}\right) - 4\right] . \tag{1.39}$$

As relativistic effects change the frequency dependence of the SZ signal, they do also for the cross over frequency, x_0. To take into account the relativistic effects in tSZ, one has to expand the Kompaneets equation in a power series of x. The numerical fit is given by [80] by taking into account the third-order correction term. Thus, the new cross over frequency also changes which is given by a numerical fit as [83]

$$x_0 = 3.830(1 + 1.1674x - 0.8533x^2) . \tag{1.40}$$

In principle, relativistic corrections should be made for the calculation of the kSZ signal if the velocity of the cluster is high enough. The relativistic kSZ term is rather small which corresponds to $\langle y \rangle = 10^{-8}$ after averaging over all the clusters [84]. In Figure 1.6 we show the frequency dependence of the intensity due to the tSZ, kSZ and rSZ effects.

1.6 Foregrounds

We won't be addressing open problems concerning Foreground emissions for CMB experiments in this Thesis. On the other hand, we would like to highlight the main challenges associated to them in this Section, as they are most relevant nowadays, especially in polarization and for B-modes in particular. We will focus on the diffuse foregrounds only, emitted by our own Galaxy. At the present level of knowledge, two emissions contribute to the polarized Galactic emission. The synchrotron is caused by cosmic ray electrons spiraling the Galactic magnetic field lines. The dust grains have instead an almost thermal spectrm (grey body), at a temperature of about 18 K, and heated back by starlight. The synchrotron is dominant at low frequencies, $\nu \lesssim 60$ while dust emission dominates at higher ones. Figure 1.7 shows the contamination on the lensing B-modes to the Synchrotron and dust emission as forecasted by the Simons Observatory [85]. The frequency bands are highlighted in grey, and the *rms* of foreground refer to about 10% of the sky. Synchrotron and thermal dust emissions are generate in map space for the SAT forecasts using the PySM model [86], which extrapolates template Galactic emission maps estimated from *Planck* and WMAP data. As an illustration of the Foreground behavior across the whole sky, we also show *Planck* maps with foregrounds in Figure 1.8, in total intensity. The Galactic emission is dominated by synchrotron at 30 GHz, mixed between synchrotron and dust at 100 GHz, dust dominated at 545 GHz.

There are several foreground removal methods which follow different assumptions in order to extract the CMB signal. We highlight the parametric fitting in which foreground and background unknowns are parametrized and fitted out of multi-frequency datasets [88, 89, 90], using a data model written as

$$d_i(p) = \sum_j A_{ij}(p)s_j(p) + n_i(p) . \tag{1.41}$$

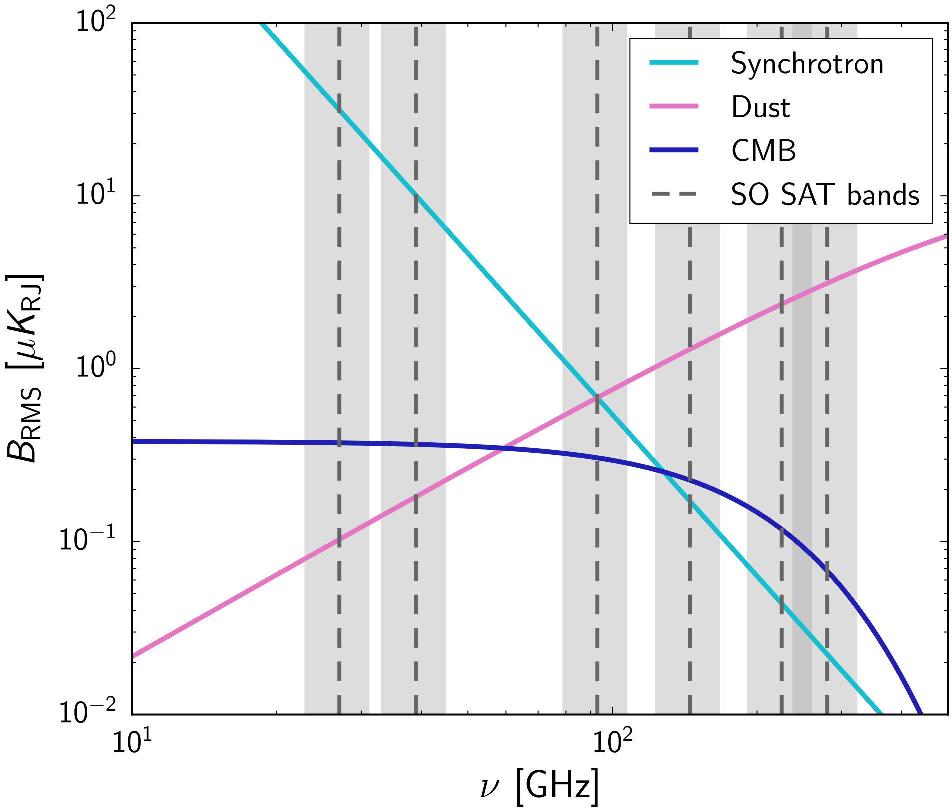

Figure 1.7: RMS brightness temperature variation of synchrotron, dust and CMB lensing B mode with frequency, over 10% of the sky, in the targeted region for the Simons Observatory. The virticle dashed lines represent central frequencies of the Small aperture telescopes (SATs) of the Simons Observatory.

Here, $d_i(p)$ is the measured signal in each frequency band i. $s_j(p)$ is the unknown vector which contains both CMB and foregrounds, and these components are labeled by running index j. $A_{ij}(p)$ is the mixing matrix which combines different sky components in a certain way so that it gives the signal for each of the considered frequency channels. n_p is the uncorrelated Gaussian instrumental noise with dispersion N_i.

In simple applications, synchrotron is assumed to follow a power law behaviour as [91, 92]

$$A_{\rm syn}(\nu, \nu_{\rm ref}) = \left(\frac{\nu}{\nu_{\rm ref}}\right)^{\beta_s}, \tag{1.42}$$

where $\nu_{\rm ref}$ is the reference frequency and β_s is the spectral index for synchrotron. The dust emission is described by modified grey body spectrum, given by [92]

$$A_{\rm dust}(\nu, \nu_{\rm ref}) = \left(\frac{\nu}{\nu_{\rm ref}}\right)^{\beta_d+1} \frac{e^{\frac{h\nu_{\rm ref}}{kT_d}} - 1}{e^{\frac{h\nu}{kT_d}} - 1}. \tag{1.43}$$

β_d and T_d are the spectral index and temperature of dust respectively. Explicit applications and results of this phenomenology to *Planck* can be found in [91].

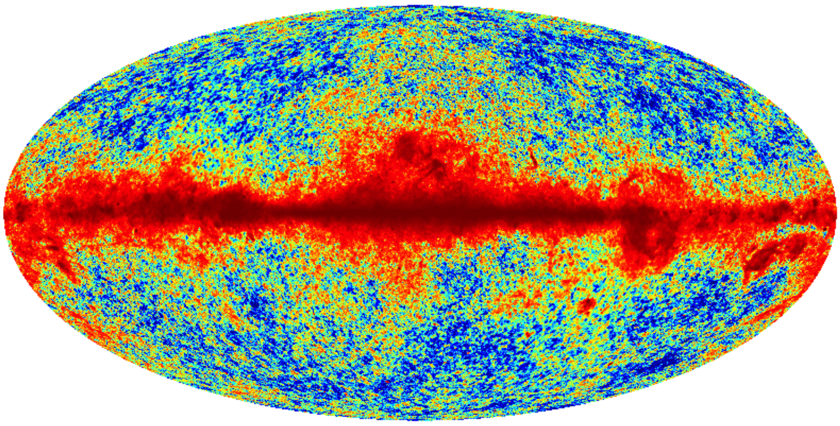

30 GHz

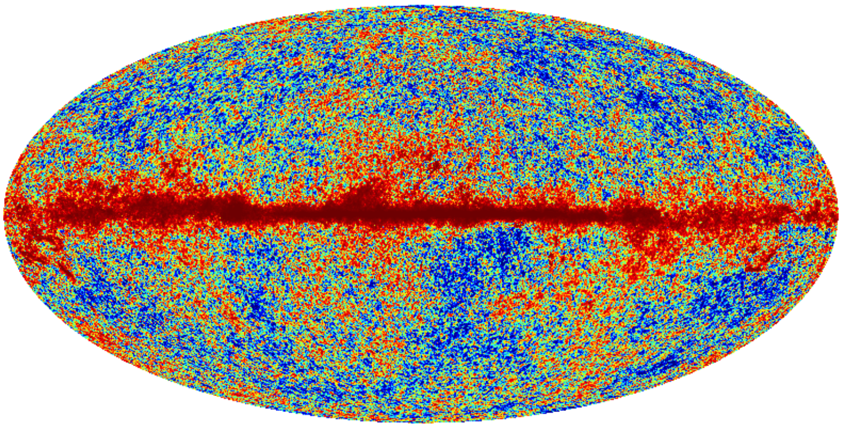

100 GHz

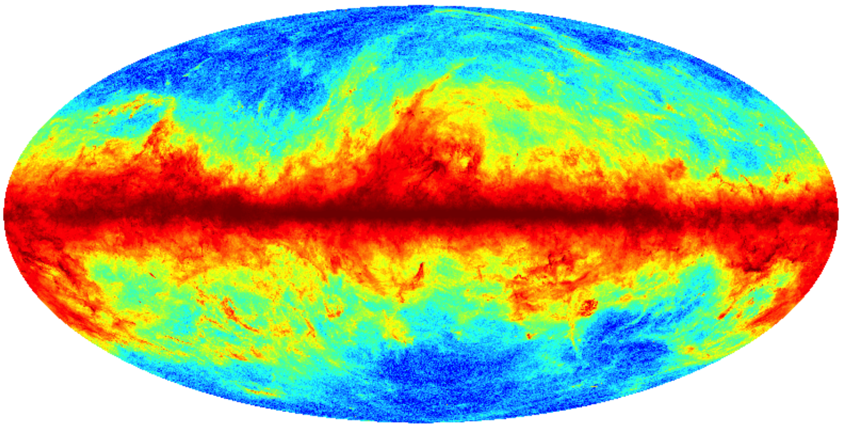

545 GHz

Figure 1.8: The CMB sky seen by *Planck* with 30, 100 and 545 GHz. All the maps are taken from the *Planck* Legacy Archive (https://pla.esac.esa.int) [87].

1.7 Present and Future CMB experiments

We end this Chapter by reviewing the present measures concerning the CMB and the most important future experiments.

In figure 1.9, we show the temperature power spectra as measured by *Planck* [13]. The error bars shown in the figure corresponds to the 1σ uncertainty, and the continue line the prediction from the fiducial ΛCDM model. The latter consists of six independent parameters which are Hubble constant (H_0), dark matter density (Ω_c), baryon density (Ω_b), the amplitude of the primordial perturbation (A_s), scalar spectral index (n_s) and the optical depth (τ). The measurements are complemented by the WMAP measurements [93] and on smaller scales by the ACTpol and SPTpol observations [94, 95]. All together, the data allow to constrain all six ΛCDM parameters by percent precision or better.

1.7.1 Future Probes

For a full list of operating and future probes, please see the Legacy Archive for Microwave Background Data Analysis[5]. We report here only the future probes we use for our forecasts in this Thesis.

Simons Observatory: The SO is being deployed in the Atacama Desert in Chile and will operate in six frequency channels from 27 GHz to 280 GHz. The SO is a series of telescopes which consists of three Small 0.4 m Aperture Telescopes (SATs) and one 6 m Large Aperture Telescope (LAT). The LAT will scan 40% of the sky with arcmin resolution, and SATs will observe 10% of the sky at degree scale. The overall sensitivity and resolution will be ten times and five times compared to the *Planck* satellite [53, 101, 102]. One of the most important science goals of SO is to measure the amplitude of the primordial B-mode signal. So will target to probe the the primordial B modes with uncertainty $\sigma(r) = 0.003$ for an $r = 0$ model [53]. This will be able to detect primordial GWs with $r \geq 0.01$ with at least 3σ. So will also aim to measure the sum of neutrino mass with uncertainty $\sigma \sum m_\nu = 0.04$ via CMB lensing, cluster counts through SZ effect combined with LSS data from Dark Energy Spectroscopic Instrument [6] (DESI) [103]. SO will play an important to constrain the duration and mean redshift of reionization.

CCAT-prime: CCAT-prime is a 6-meter telescope which will be built up at an altitude of 5600 meters at Cerro Chajnantor in the Atacama region of Chile. Due to its substantial altitude, atmospheric noise will be less than the other experiments in the Atacama desert. CCAT prime will observe in the frequency range 100 to 800 GHz; hence, the study of dust contamination will play an essential role in the detection of primordial B modes. CCAT prime will probe reionization via the cooling radiation in the 158 μ m [CII] line from star-forming galaxies. Detection of kSZ and relativistic SZ signal, measurement of the sum of neutrino mass, constraining the Dark energy parameters via kSZ are the other vital goals of CCAT-prime.

CMB-S4: CMB-S4 (CMB stage IV)is a planned fourth-generation CMB experiment

---

[5] https://lambda.gsfc.nasa.gov

[6] https://www.desi.lbl.gov/

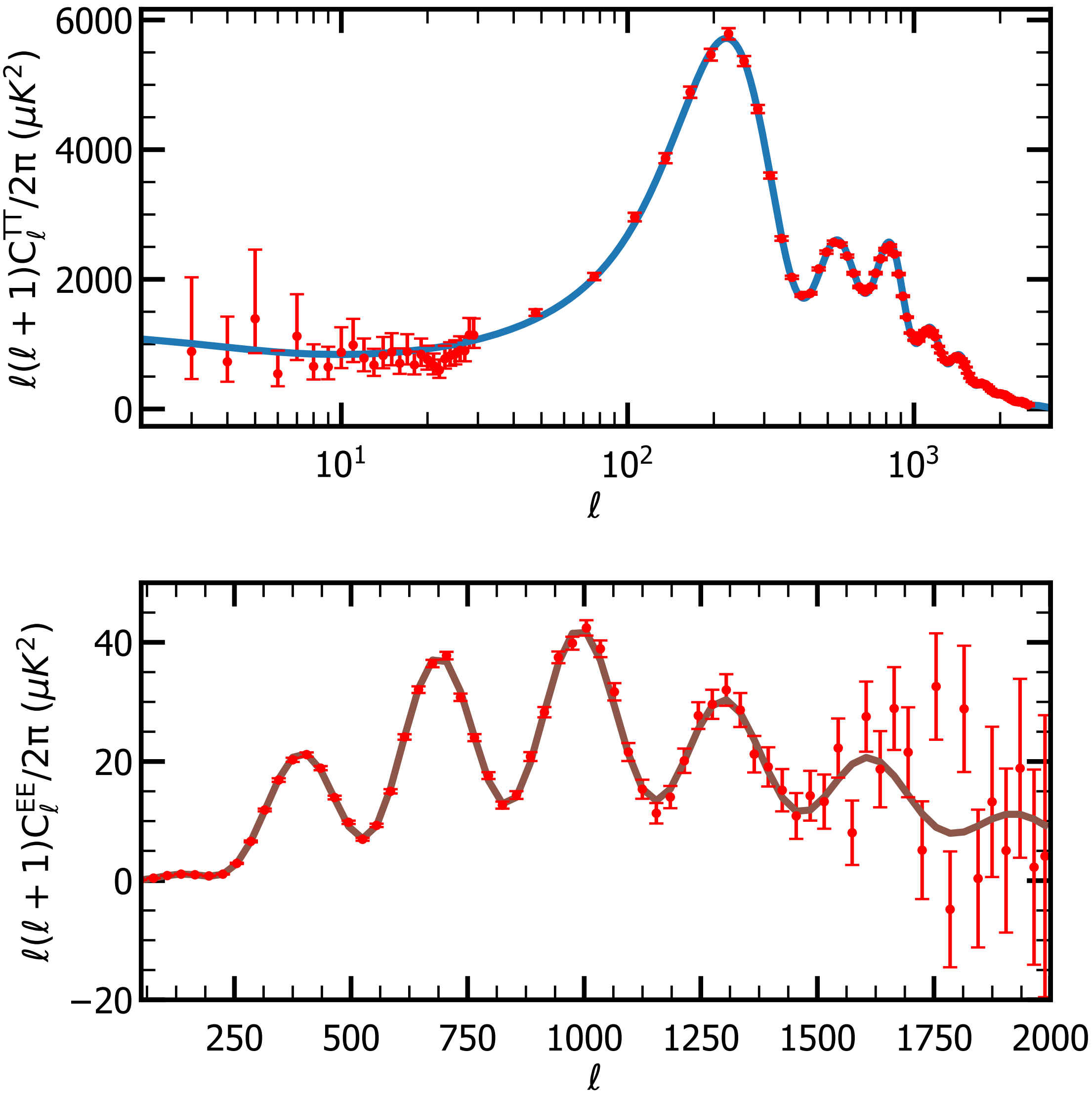

Figure 1.9: Top panel: Best-fit temperature power spectra measured by *Planck* along with measurements. Bottom panel: The best fit E-mode power spectra measure by *Planck* [13].

from the ground. It will consist of the $500,000$ detectors by combining the telescope arrays situated both in the Atacama desert and South pole. The ultimate sensitivity will be 1 μK-arcmn with three arcmin resolution. CMB-S4 will be able constrain the neutrino mass and number of effective number of neutrino species reaching a sensitivity $\sigma(\sum m_\nu) = 16$ MeV, $\sigma(N_{\rm eff}) = 0.02$. It will also be able to detect the primordial gravitational wave due to inflation for $r \gtrsim 10^{-3}$ with 5σ.

LiteBIRD: the LiteBIRD satellite mission by JAXA[7] with participation of ESA and

---

[7] Japan Aerospace Exploration Agency

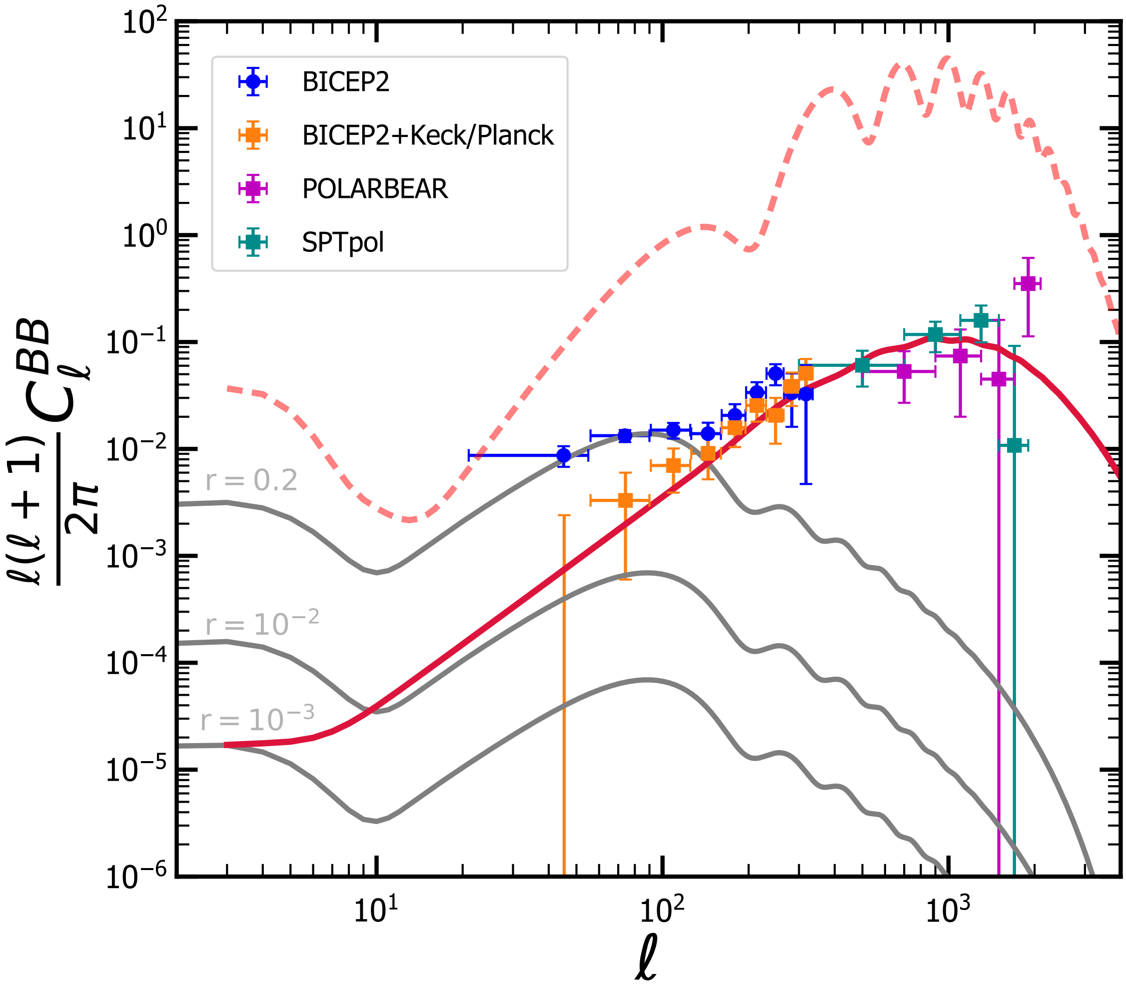

Figure 1.10: Current status of CMB polarization observation towards the detection of primordial B modes. Solid black lines represent primordial B-mode power spectra with $r = 0.2$, 10^{-2} and 10^{-3}. We put all the data points from the data taken by BICEP2 [4] [96], BICEP2+Keck/*Planck*, POLARBEAR and SPT [97, 98, 99, 100]. Lensing B-mode is shown in a solid red line. We also show lensing E-mode (red dashed line) power spectra for comparison.

NASA [8] to measure the temperature and polarization anisotropies of the CMB with 15 frequency bands from 40 GHz to 402 GHz [104]. For the detection of primordial B modes with $\sigma(r) \lesssim 10^{-3}$ with $r = 0$. LiteBIRD will also measure the reionization optical depth τ with ultimate precision at the cosmic variance limit, and the forecasted uncertainty is $\sigma(\tau) = 0.002$ [104].

---

[8] European Space Agency and the National Aeronautics Space Administration

Chapter 2

Optical Depth reconstruction

> A feature of science is that as the frontiers of our knowledge are extended, new mysteries, just beyond the frontiers, come into sharper focus
>
> *Martin J. Rees*

2.1 Introduction

In this Chapter, we study the capability of future CMB experiments concerning the reconstruction and understanding of the reionization process, by probing not only the sky averaged reionization history, but also the accessible information regarding its morphology through the dependence on the line of sight. That would provide invaluable insight into the reionization process which would open unprecedented windows on the astrophysical processes responsible for the epoch of reionization, but also allowing to reconstruct the overall behaviour of cosmology at those epochs.

Ultraviolet radiation from first sources ionizes the IGM and alters the thermal, ionization and chemical properties of the gas. The reionization optical depth τ, weighting Thomson cross-section along the line of sight, represents a most important characterization of the effect. Through the measurements of large-scale E-mode polarization in the CMB anisotropies ("reionization bump"), the WMAP has constrained the sky average optical depth to be 0.089 ± 0.014 [105]; the Planck satellite, by combining the polarization data ranging from 30 to 353 GHz, reported a lower value, $\tau = 0.058 \pm 0.012$ [106]. In Figure 2.1, we show the improvement of the measurement of τ by WMAP and *Planck*. This Chapter has been derived from [107] where the 2015 value of τ from *Planck* was used, slightly different from the one we quote in Chapter 3 which refers to the 2018 release. For consistency, we will adopt the old value in this Chapter.

Accurate τ measurements are crucial for breaking degeneracies with the amplitude of the primordial scalar perturbations A_s in order to infer the dependence of the primordial power with physical scales. However, a precise astrophysical knowledge of the reionization process is necessary for interpreting and exploiting the τ measurements expected from future CMB polarization experiments. Most important targets of these efforts are represented by the B-modes of CMB polarization from cosmological Gravitational Waves and Gravitational Lensing. Currently the POLARBEAR/Simons Array [108, 109], BICEP[1]3 [96], ACTpol[2][75], SPT 3G[3][74], SPIDER[4] [110], EBEX[5] [111] and others[6] are searching these signals. In the near future, the Simons Observatory [7] will be observing from the Atacama desert, paving the way to a network of ground-based systems equipped with 10^4 detectors, which will represent the Stage-IV (CMB-S4) phase of ground-based CMB experiment.

The detection of almost complete Lyα absorption in the spectra of distant quasars may suggest that the end of reionization occurred around $z \approx 6$ [112]. Recent data on the evolution of Lyα optical depth show a sharp increase for redshift z larger than $6-7$. A similar conclusion is supported by the study of the line of sight variations in the IGM Lyα optical depth [113]. Moreover, the Lyα transmission profile of the highest-redshift quasar (Quasi-Stellar Objects, QSO) ULAS $J112001.48+064124.3$ at $z \sim 7.1$ is strikingly different from that of two lower redshifts $z \sim 6.3-6.4$ counterparts detected in the Sloan Digital Sky Survey (SDSS[8]). It features a measured near-zone radius of ~ 1.9 Mpc, a factor of ~ 3 smaller than it is typical for QSOs at $z \sim 6-6.5$ [114], suggesting higher$-z$ QSOs live in an IGM whose HI fraction is much higher. High redshift GRBs with their bright afterglow can also be exploited as probes of cosmic reionization, dispensing with some of the complications inherent to QSO observations. Extreme drop off in transmission profile of GRB140515A at z $\approx$ 6.3 places an upper limit on HI fraction at these redshift [115, 116]. Several studies support the picture that first galaxies in the Universe are the primary source of reionization [117, 118, 119] but the morphology of the reionization process is still poorly understood. Numerical simulations, as well as analytical studies, suggest that ionization fraction is spatially inhomogeneous [120, 117, 121]. Reionization sources first ionize the surrounding IGM by producing ionized bubbles around them and later they grow and merge [122, 123]. Patchy reionization produces different scattering histories along a different line of sights so that the value of τ varies with the direction. Patchy reionization also generates kSZ signal due to the peculiar motion of ionized bubbles along the line of sight [124, 125]. In the near future, it will be possible to detect patchy kSZ signal and separating that from other secondary anisotropies in the CMB, by exploiting an accurate astrophysical modelling [66]. [126] constrained the optical depth fluctuations by estimating the trispectrum from Planck 2015 CMB temperature anisotropies data.

The chapter is organized as follows: in Section 2.2 we discuss a realistic model of

---

[1] Background Imaging of Cosmic Extragalactic Polarization, `www.cfa.harvard.edu/CMB/bicep3`

[2] Atacama Cosmology Telescope (polarization-sensitive), `https://act.princeton.edu/`

[3] South Pole Telescope (third generation), `https://pole.uchicago.edu/`

[4] `https://spider.princeton.edu`

[5] The E and B Experiment, `http://groups.physics.umn.edu/cosmology/ebex/`

[6] See `lambda.gsfc.nasa.gov` for a complete list of operating and planned CMB experiments.

[7] `https://simonsobservatory.org`

[8] `www.sdss.org`

reionization based on recent determination of the star formation rate functions. In Section 2.3 we study the effects of reionization on the CMB. In Section 2.4 we implement the reconstruction method first introduced by [127] and forecast the capabilities of future CMB experiments with specifications corresponding to CMB-S4 to detect patchy reionization. In Section 2.5 we summarize our findings. Throughout this work we assume flat ΛCDM cosmology with parameters $h = 0.677$, $\Omega_b h^2 = 0.02230$, $\Omega_c h^2 = 0.1188$, $\Omega_\Lambda = 0.6911$, $n_s = 0.9667$, $A_s = 2.142 \times 10^{-9}$, derived from the combinations of Planck TT,TE,EE,LowP+Lensing+Ext [128]. Stellar masses and luminosities of galaxies are based on a Chabrier initial mass function [20].

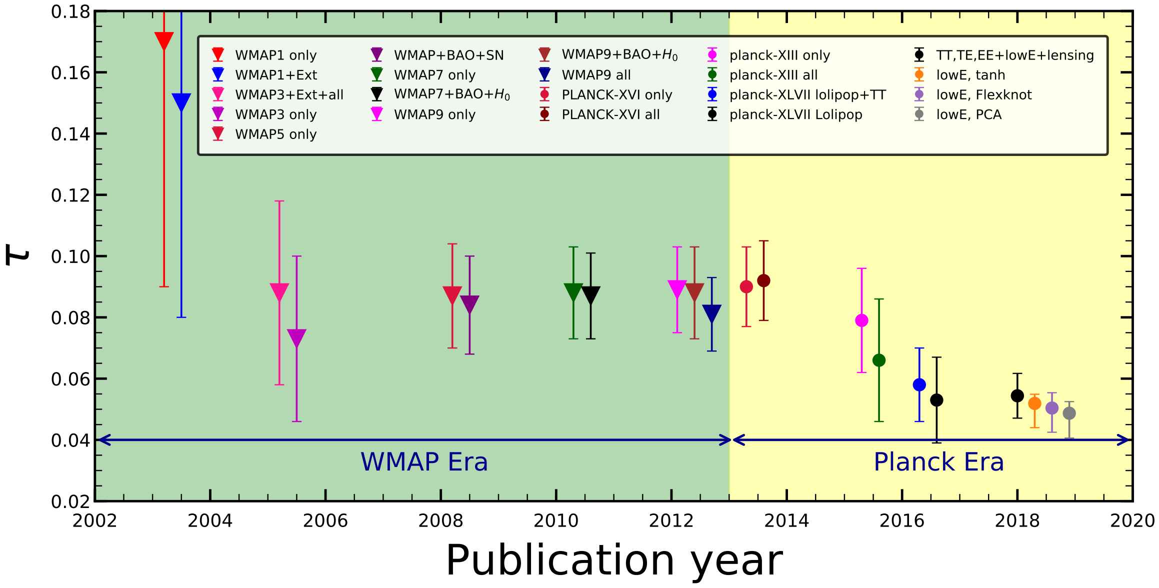

Figure 2.1: The measured value of τ has been improved significantly from the WMAP to *Planck* era. This plot shows the value of τ is now very well constraint and hence, also the mean redshift and duration of reionization.

2.2 Realistic Models of Reionization

This Section describes our model of reionization based on the assumption that star-forming galaxies are the primary source of ionizing photons.

2.2.1 SFR functions

In this Chapter, we assume the [129, 130] and [119] models of cosmological star formation history. These are based on analyses of recent dust-corrected UV, far-IR and radio data (see figure 2.2).

For galaxies with relatively low star formation rates ($\dot{M}_\star \lesssim 30\, M_\odot$ yr^{-1}), UV observations are the most important tracers of the SFR. Dust emission is mainly due to the diffuse (cirrus) dust component, and attenuation is mild. Thus UV data extending down to a magnitude $M_{\rm UV}\approx -17$ have been dust-corrected according to the local empirical relation between the UV slope $\beta_{\rm UV}$ and the IR-to-UV luminosity ratio IRX [see 131], that is also routinely exploited for high-redshift galaxies [see 132, 133, 134, 135]. A Meurer/Calzetti prescription has been adopted, but the determination of the SFR functions is only marginally affected at the faint end by choosing a different extinction law, like for example the Small Magellanic Cloud (SMC) one.

For galaxies with relatively higher star formation rates, far-IR and radio data are the most important tracers as dust emission is largely dominated by molecular clouds and the UV dust corrections are large and uncertain [see 136, 137, 138, 139, 140]. Interestingly, the shape of the SFR function for $\dot M_\star \gtrsim 10^2\, M_\odot$ yr^{-1}, which so far has been probed only indirectly at $z\gtrsim 4$ due to sensitivity limits in current far-IR surveys, is found to agree out to $z\lesssim 6$ with the constraints from the recent VLA-COSMOS radio survey [see 141] and from the few individual galaxies detected at $z\gtrsim 5$ with ALMA and SMA [see 142, 143].

The luminosity L has been converted into the SFR $\dot M_\star$ using $\log \dot M_\star/M_\odot\ {\rm yr}^{-1}\approx -9.8+\log L/L_\odot$, a good approximation both for far-IR and (intrinsic) UV luminosities, as expected on energy conservation arguments, under the assumption of a Chabrier's IMF. Note that actually this conversion factor depends on the star formation history, and specifically on duration and age of the burst [see 137, 144]; the standard value adopted here is the average for a continuous star formation over 100 Myr, the age at which 90% of emission has been contributed [see 145, their table 1].

The SFR function can be described as a smooth Schechter function

$$\frac{{\rm d}N}{{\rm d}\log \dot M_\star}(\dot M_\star, z)=\mathcal{N}(z)\,\left[\frac{\dot M_\star}{\dot M_{\star,c}(z)}\right]^{1-\alpha(z)}\, e^{-\dot M_\star/\dot M_{\star,c}(z)}\;, \tag{2.1}$$

with three parameters: the overall normalization $\mathcal{N}$, the characteristic SFR $\dot M_{\star,c}$ and the faint end slope α. The redshift evolution for each parameter $p(z)$ of the Schechter function has been described as a third-order polynomial in log-redshift $p(z)=p_0+p_1\,\xi+p_2\,\xi^2+p_3\,\xi^3$, with $\xi=\log(1+z)$. The values of the parameters $\{p_i\}$ are reported in Table 1 of [119]. In Figure 2.2 dashed lines refer to the (dust-corrected) UV-inferred SFR functions while solid line to the global (UV+far-IR/radio) SFR functions. The behavior of the normalization $\mathcal{N}$ and of the characteristic SFR $\dot M_{\star,c}$ highlights that UV surveys tend to pick up many galaxies with low SFR, while far-IR surveys also select less numerous galaxies with higher SFR; this mirrors the fact that high SFRs are usually associated to large dust abundance. The evolution with redshift of these parameters shows that most of the SFR occurs in dusty galaxies around redshift $z\approx 2$ (cf. also Figure 2.3); on the other hand, toward high redshift $z\gtrsim 6$ the dust content progressively decreases and UV surveys become more effective in selecting the typical population of star forming galaxies. For the purpose of this chapter, the high-redshift evolution is most relevant.

[129, 130] and [119] validate the SFR functions against independent datasets, including integrated galaxy number, counts at significative far-IR/(sub)mm/radio wavelengths, counts/redshift distributions of strongly gravitationally-lensed galaxies, stellar mass function via the continuity equation, main sequence of star-forming galaxies, and even associated AGN statistics. In particular, the analysis of the main sequence for high-redshift galaxies and AGNs presented in [146], and Lapi et al. (2017b) highlights that the current data can be consistently interpreted in terms of an in situ coevolution scenario for star formation and black hole accretion, envisaging these as local, time coordinated processes.

Since faint galaxies are likely the source of much of the ionizing background, we need to extrapolate the SFR to well beyond the magnitude limit of the current blank field surveys $M_{\rm UV} \approx -17$ (corresponding to SFR $\dot{M}_\star \approx$ a few $10^{-1}\, M_\odot$ yr^{-1}) down to $M_{\rm UV} \approx -13$ (corresponding to SFR $\dot{M}_\star \approx$ a few $10^{-2}\, M_\odot$ yr^{-1}). Actually, at redshifts $z \lesssim 6$ the faint end of the luminosity/SFR functions has been recently explored, though still with large uncertainties, even down to $M_{\rm UV} \approx -13$ via gravitational lensing by foreground galaxy clusters [see 147, 148, 149, 134]. We have reported (but not used in the fit because of the still large systematic uncertainties) these data in Figure 2.2 to highlight that they are indeed consistent with the extrapolation of our SFR functions; specifically, the faint portion of the SFR function is seen to keep rising steeply with $\alpha \lesssim 2$ out to $z \lesssim 6$.

2.2.2 Cosmic star formation rate density

Based on the star formation rate functions in the previous section, we can compute a star formation rate density:

$$\rho_{\rm SFR}(z) = \int_{\dot{M}_\star^{\rm min}}^{\infty} {\rm d}\log\dot{M}_\star\, \frac{{\rm d}N}{{\rm d}\log\dot{M}_\star}\, \dot{M}_\star\ ; \tag{2.2}$$

Since the SFR function diverges at the faint end ($\alpha \gtrsim 1$), the results are sensitive to the minimum SFR cutoff, $\dot{M}_\star^{\rm min}$. Figure 2.3 shows the cosmic star formation rate based on integrating the UV-corrected SFR to three cut-offs: $M_{\rm UV} \approx -17$, the observational limit of current blank field surveys. The outcome matches the determination by [150, dotted line] and is in good agreement with the dust corrected data by [151, cyan shaded area] at $z \lesssim 4$ and by [133, cyan squares] at $z \gtrsim 4$. On the other hand, the cosmic SFR density from (dust-corrected) UV data is inconsistent with other datasets both at low and high redshift. Specifically, at redshift $z \lesssim 4$ it falls short with respect to the multiwavelength determination by [152, orange shaded area] based on UV/optical, radio, Hα and mid-IR 24 μm data, to the far-IR measurements from *Herschel* by [153] and [154, red shaded area], and by the recent estimate from deblended data from *Herschel*, JCMT/AzTEC and JCMT/SCUBA-2 in the GOODS field by [155]. At redshift $z \gtrsim 4$ it underestimates the determinations based on stacking of far-IR data from *Herschel* by [156, red dots], the measurements from radio data by [141], and the estimates based on long GRB rates from *Swift* by [157, 158]. This mostly reflects the fact, already mentioned above, that the UV-inferred SFR functions (even corrected for dust extinction by the UV slope) appreciably underestimate the number density of dusty galaxies with $\dot{M}_\star \gtrsim 30\, M_\odot$ yr^{-1}.

Then we compute the cosmic SFR density exploiting our global SFR functions down to the same magnitude limit $M_{\rm UV}^{\rm min} \approx -17$. The outcome (solid line) is found to be in good agreement both with the [152], [154] and [155] determinations at $z \lesssim 4$, with the stacked far-IR data by [156] at $z \gtrsim 4$. In Figure 2.3 we also show the outcomes when integrating our global SFR functions down to $M_{\rm UV}^{\rm lim} \approx -13$ (dot-dashed line) and -12 (dashed line); as we shall discuss in the next Section, these value are suggested by the recent data on the reionization history of the Universe in terms of electron scattering optical depth $\tau_{\rm es} \approx 0.058$ as measured by [159].

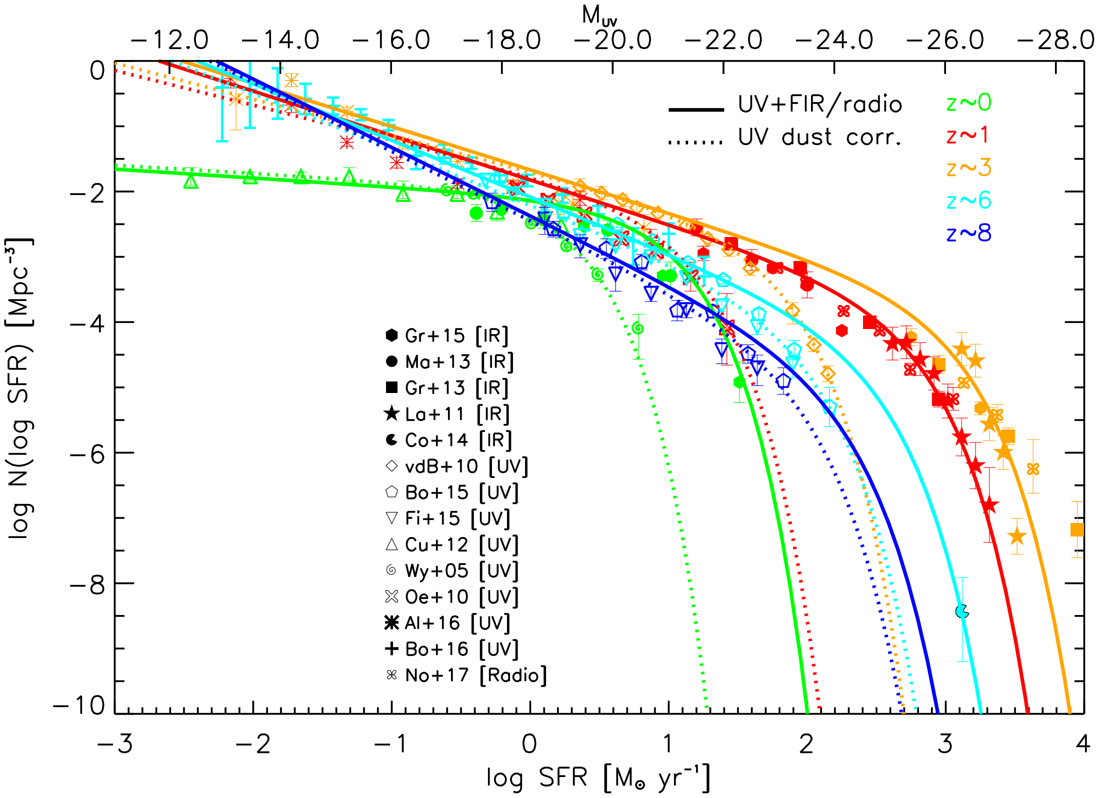

Figure 2.2: The SFR functions at redshifts $z = 0$ (green), 1 (red), 3 (orange), 6 (cyan), and 8 (blue) determined according to the procedure by [129, 130, 146] and [119]. Solid lines refer to the rendition from UV (dust corrected according to standard prescriptions based on the UV slope) plus far-IR/radio data; dotted lines refer to the rendition from only (dust-corrected) UV data. UV data (open symbols) are from [160, diamonds], [133, pentagons], [161, inverse triangles], [162, triangles], [163, spirals], [164, crosses], [148, asterisks], [134, plus signs]; far-IR data from [165, hexagons], [153, circles], [154, squares], [119, stars], and [166, pacmans]; radio data from [141, clovers].

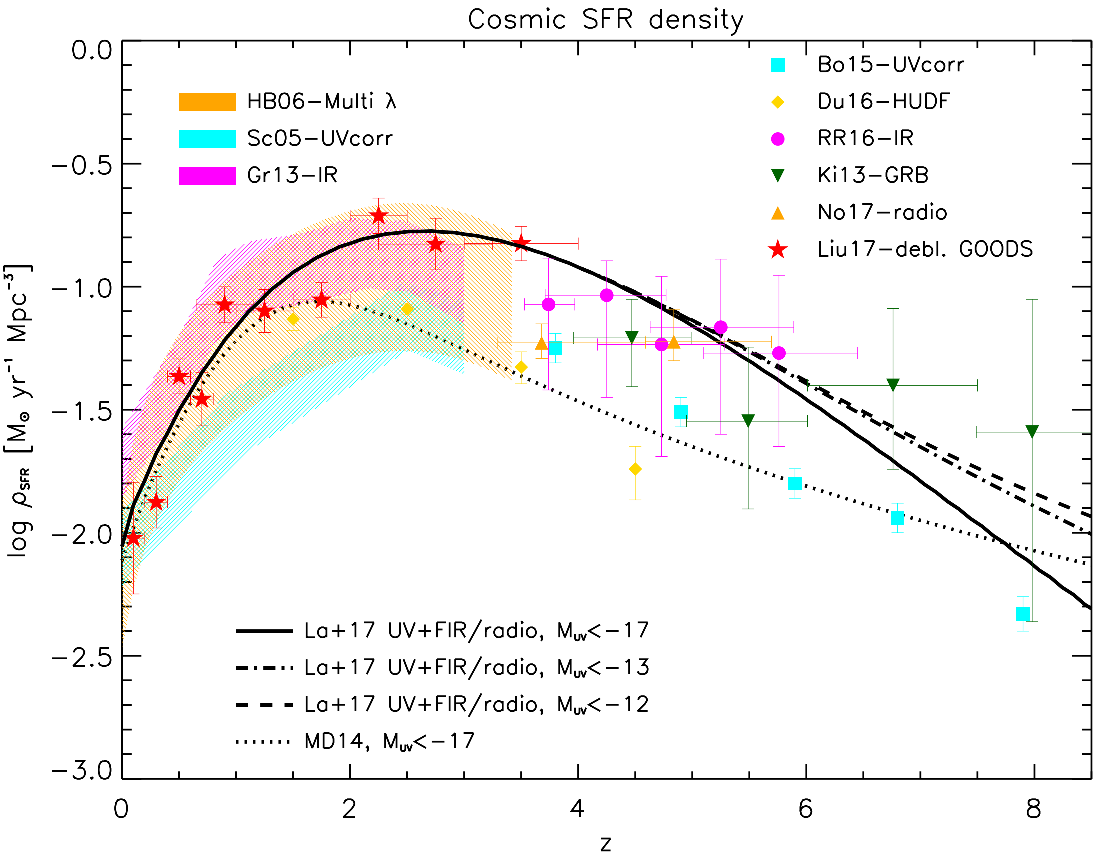

Figure 2.3: Cosmic SFR density as a function of redshift. The solid, dot-dashed, and dashed lines are our results on using the SFR functions from UV+far-IR/radio data presented in Figure 2.2, integrated down to a magnitude limit $M_{\rm UV} \lesssim -17$, -13, and -12, respectively. For comparison, the dotted line illustrates the determination by [150] from dust-corrected UV data integrated down to a magnitude limit $M_{\rm UV} \lesssim -17$. At $z \lesssim 4$ data are from (dust-corrected) UV observations by [151, cyan shaded area]; far-IR observations by [154, magenta shaded area]; multiwavelength determination including UV, radio, Hα, and mid-IR 24 μm data collected by [152, orange shaded area]; deblended far-IR/sub-mm data on the GOODS field by Liu et al. (2017; red stars). At higher redshifts $z \gtrsim 4$, we report the estimate of the SFR density inferred from (dust-corrected) UV data by [133, cyan sqares], stacked IR data by [156, magenta circles], and long GRB rates by [157, 158, green stars].

2.2.3 Reionization history

The cosmic star formation history determines the cosmic ionization history. The cosmic ionization rate is proportional to cosmic SFR density:

$$\dot{N}_{\rm ion} \approx f_{\rm esc}\, k_{\rm ion}\, \rho_{\rm SFR}\ ; \qquad (2.3)$$

here $k_{\rm ion} \approx 4 \times 10^{53}$ is the number of ionizing photons s^{-1} $(M_\odot/{\rm yr})^{-1}$, with the quoted value appropriate for a Chabrier IMF, and $f_{\rm esc} \approx 1 - 20\%$ is the poorly constrained

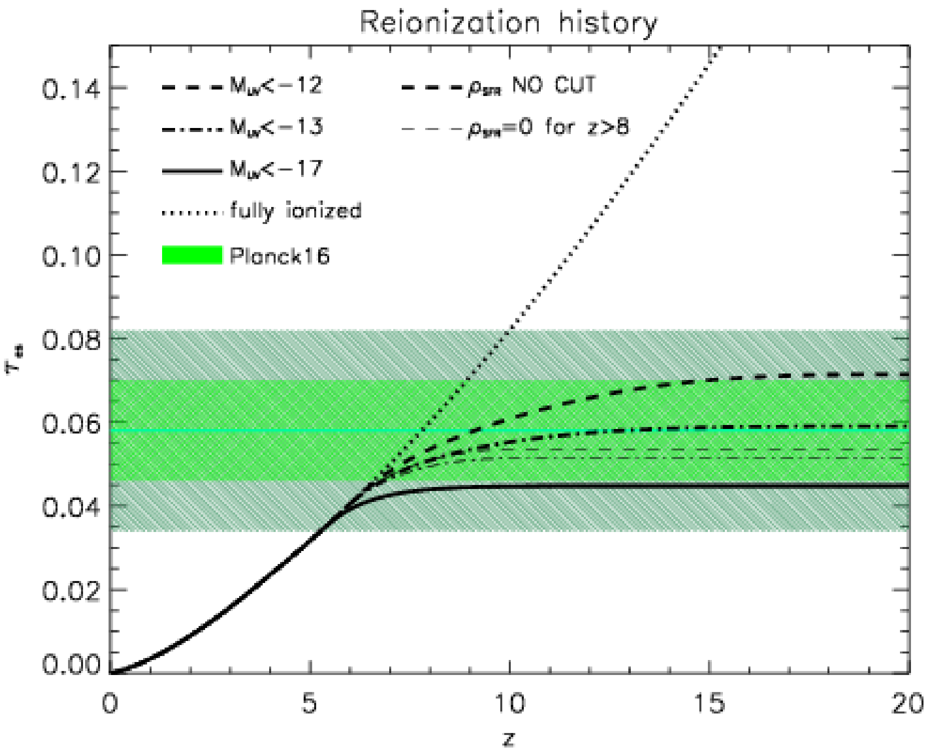

Figure 2.4: Reionization history of the universe, in terms of the redshift evolution of the optical depth $\tau_{\rm es}$ for electron scattering. Thick solid, dot-dashed and dashed lines illustrate the outcomes of the EERM for the cosmic SFR density integrated down to UV-magnitude limits $M_{\rm UV} \lesssim -17$, -13, and -12, respectively; thin lines refer to SFR density truncated at $z > 8$. For reference, the dotted line refers to a fully ionized universe up to redshift z. The green line shows the measurement (with the 1σ and 2σ uncertainty regions highlighted by the dark and light green areas respectively) from [159].

average escape fraction for ionizing photons from the interstellar medium of high-redshift galaxies [see 167, 168, 169]. Note that two other parameters implicitly entering in the expression $\rho_{\rm SFR}$ are the minimum UV limiting magnitude, and the faint-end slope of the SFR functions α discussed at the end of Section 2.2.1.

The competition between ionization and recombination determines the evolution of the ionization state of the universe [see 170, 171]:

$$\dot{Q}_{\rm HII} = \frac{\dot{N}_{\rm ion}}{\bar{n}_{\rm H}} - \frac{Q_{\rm HII}}{t_{\rm rec}} \tag{2.4}$$

Here $\bar{n}_{\rm H} \approx 2 \times 10^{-7}\,(\Omega_b h^2/0.022)$ cm^{-3} is the mean comoving hydrogen number density. In addition, the recombination timescale reads $t_{\rm rec} \approx 3.2$ Gyr $[(1+z)/7]^{-3}\, C_{\rm HII}^{-1}$, where the case B coefficient for an IGM temperature of 2×10^4 K has been used; this timescale crucially depends on the clumping factor of the ionized hydrogen, for which a fiducial value $C_{\rm HII} \approx 3$ is usually adopted [see 172].

The electron scattering optical depth is proportional to the integrated electron density along the line-of-sight:

$$\tau_{\rm es}(z) = c\,\sigma_{\rm T}\,\bar{n}_{\rm H} \int_t^{t_0} {\rm d}t'\, f_e\, Q_{\rm HII}(z')(1+z')^2; \tag{2.5}$$

here $dt = \frac{dz}{H(z)}$ and $H(z) = H_0\,[\Omega_M\,(1+z)^3 + 1 - \Omega_M]^{1/2}$ is the Hubble parameter, c is the speed of light, $\sigma_{\rm T}$ the Thomson cross section and f_e the number of free-electrons per ionized hydrogen atom (assuming double Helium ionization at $z \lesssim 4$.).

Figure 2.4 shows the cosmic reionization history computed from our global SFR function integrated down to different $M_{\rm UV}^{\rm lim}$, on assuming a conservative value $f_{\rm esc} \approx 0.1$ for the escape fraction of ionizing photons. When adopting $M_{\rm UV}^{\rm lim} \approx -13$, the outcome (black dot-dashed line) agrees with the value of the optical depth for electron scattering $\tau \approx 0.058$ recently measured by the *Planck* mission. For reference, the dotted line represents the optical depth expected in a fully ionized Universe up to redshift z; this is to show that the bulk of the reionization process occurred at $z \sim 8-9$ and was almost completed at $z \sim 6$ [see 173]. Note that from this perspective, the detailed behaviour of the SFR functions at $z \lesssim 6$ and at $z \gtrsim 10$, and the related ionizing background, are only marginally relevant. Remarkably, the evolution of the ionized fraction $Q_{\rm HII}$ illustrated in the inset is fully consistent with upper and lower limits from the plethora of independent observations collected by [169].

When adopting $M_{\rm UV}^{\rm lim} \approx -17$, that corresponds to the observational limits of current blank-field UV surveys at $z \gtrsim 6$ (cf. Figure2.3), the outcome on the optical depth (solid black line) touches the lower boundary of the 1σ region allowed by *Planck* data, and the evolution of the $Q_{\rm HII}$ parameter is inconsistent with the aforementioned observational limits. At the other end, going much beyond $M_{\rm UV}^{\rm lim} \approx -13$ is not allowed, since already for $M_{\rm UV}^{\rm lim} \approx -12$ the resulting optical depth (black dashed line) touches the upper boundary of the 1σ region from *Planck* data.

Note that these outcomes suffer to some extent of parameter degeneracy, as highlighted by the expression

$$f_{\rm esc}\, k_{\rm ion}\, C_{\rm HII}^{-0.3}\, \Gamma[2-\alpha; \dot{M}_\star^{\rm lim}/\dot{M}_{\star,c}] \approx {\rm const}, \tag{2.6}$$

where $\Gamma[a;z] \equiv \int_z^\infty {\rm d}x\; x^{a-1}\, e^{-x}$ is the incomplete $\Gamma-$function; the parameters involved are the escape fraction $f_{\rm esc}$, the ionizing rate per unit SFR $k_{\rm ion}$ associated mainly to the IMF, the clumping factor $C_{\rm HII}$, the faint-end slope of the SFR function α, and the UV magnitude limit $M_{\rm UV}^{\rm lim}$. The strongest dependencies are on $f_{\rm esc}$ and on the limiting magnitude $M_{\rm UV}^{\rm lim}$. For example, to reproduce the *Planck* best estimate $\tau_{\rm es} \approx 0.058$ for $M_{\rm UV}^{\rm lim} \approx -17$, it would be necessary to force $f_{\rm esc}$ to implausible values $\gtrsim 0.2$; at the other end, setting $M_{\rm UV}^{\rm lim} \approx -12$ would require $f_{\rm esc} \lesssim 0.05$, but at the cost of worsening the agreement with the observational constraints on $Q_{\rm HII}$.

Thus the combined constraints on the cosmic reionization history from Planck and the

Experiment name	Sensitivity Δ_T [μK arcminute]	θ_f [arcminute]
CMB-S4 (a)	1	1
CMB-S4 (b)	0.5	1
Litebird	1.8	16

Table 2.1: θ_f is the full width half maxima of the incident beam. CMB-S4 (a) case is the configuration taken from the CMB-S4 first science book [54] but as it is not still built up, just to be optimistic we are considering higher sensitive configuration in S4 (b) case.

cosmic SFR density measured at high redshifts $z \gtrsim 6$ from galaxy surveys (see Figure 2.3) point toward a limiting UV magnitude $M_{\rm UV}^{\rm lim} \approx -13$ and to an escape fraction $f_{\rm esc} \approx 10\%$.

Figure 2.4 shows the reionization history computed from our cosmic SFR density integrated down to different UV magnitude limits $M_{\rm UV}^{\rm lim}$, on assuming a standard value $f_{\rm esc} \approx 0.1$ for the escape fraction of ionizing photons. When adopting $M_{\rm UV}^{\rm lim} \approx -13$, the outcome (black dot-dashed line) agrees with the value of the optical depth for electron scattering $\tau \approx 0.058$ recently measured by the *Planck* mission. For reference, the dotted line represents the optical depth expected in a fully ionized Universe up to redshift z; this is to show that the bulk of the reionization process occurred at $z \sim 8-9$ and was almost completed at $z \sim 6$ [see 173]. The thin lines in the same Figure show the outcome when the SFR density is truncated for $z > 8$. Note that from these perspectives, the detailed behaviour of the cosmic SFR density at $z \lesssim 6$ and its extrapolation beyond at $z \gtrsim 10$ are only marginally relevant.

2.3 CMB effects from Reionization

The cosmological reionization process makes its signatures in the observed CMB sky. If the reionization process did not take place, CMB photons could free-stream preserving their spectral shape originated at the time of recombination. The CMB spectral shape changes due to the y-type distortion by Comptonization process during reionization epoch [174]. The Compton y parameter is of the order of 1.93×10^{-7} for $\tau = 0.058$ and electron temperature $T_e = 2 \times 10^4$ K [175]. Rich groups at $z \sim 1$ will produce a larger y distortion signal, $\sim 1 - 2 \times 10^{-6}$ [82]. Due to the generation of free electrons along the line of sight, CMB photons scattered off by those electrons during the reionization epoch, and Thomson scattering generates new polarization at the large angular scales which adds up with the polarization induced at the last scattering surface. Primary CMB anisotropies are damped in all scales by a factor $e^{-\bar{\tau}}$, where $\bar{\tau}$ is the mean reionization optical depth across the sky. Similar to CMB lensing, reionization also creates non-Gaussianity on CMB by correlating different Fourier modes. In this Section we will discuss reionization morphology effects on the CMB by taking into account the reionization model discussed in the previous Section and hereafter labelled as Empirical Extended Reionization Model (EERM). Throughout this Chapter, we adopt two foreseen experiments representing the constraining capability of the CMB in the next decade. The first is represented by the network of ground-based observatories mounting $\sim 10^4$ detectors, known as stage-IV experiment (CMB-S4) and the second one is the LiteBIRD satellite from the Japanese space agency, optimized for large scale CMB polarization observations [176]. The main features of the probes in terms of angular resolution and sensitivity are summarized in Table 2.1.

2.3.1 Sky-averaged effect

The sky-averaged reionization optical depth has been defined in Eq. (2.5) and can be also written as

$$\tau(z) = c\sigma_T \int_0^z \bar{n}_e(z')dz' \frac{dt}{dz'}, \tag{2.7}$$

Where c is the velocity of light in free space, σ_T is the Thomson scattering cross section and $\bar{n}_e(z)$ is the mean free electron number density. As in Eq. (2.5) we express $\bar{n}_e(z)$ in terms of present number density of protons n_{p0} and ionization fraction $x_e(z)$ so that $\bar{n}_e(z) = n_{p0}(1+z)^3 x_e(z)$ and $dt/dz = [H(z)(1+z)]^{-1}$, where $H(z)$ is the Hubble parameter.

The tanh reionization model [177] is most commonly used to parametrize the reionization history of the universe and it is implemented inside Boltzmann equation solver codes like CAMB , CLASS [177, 35]:

$$x_e(z) = \frac{1}{2}\left[1 + \tanh\left(\frac{y_{re} - y(z)}{\Delta_y}\right)\right], \tag{2.8}$$

where $y(z) = (1+z)^{\frac{3}{2}}$, $y_{re} = y(z_{re})$ and $\Delta_y = 1.5\sqrt{(1+z)}\Delta_z$. Two free parameters of the model are the redshift z_{re} at which ionization becomes at the 50% level and Δ_z, the width of the transition from neutral to fully ionizing state in redshift units.

We implement our reionization model, EERM by modifying CLASS code to check to which extent the EE and BB power spectrum sensitive to different ionization histories. In Figure 2.5 we compare the ionization history for EERM and the tanh reionization model corresponding to $\tau = 0.070$ (green), 0.058 (blue) and 0.044 (red), together with upper and lower limits from various observations collected by [169, empty circles]. EERM predicts more extended reionization process roughly in between the redshift range 10 to 6 corresponding to $\tau = 0.058$ (solid blue line) whereas for the tanh case x_e changes more sharply at around $z \approx 7-8$ (dashed blue line). In Figure 2.6 EE spectra show the effect of the optical depth τ as the amplitude of the bump increases with higher τ value. Size of the horizon at the time of reionization is much larger than the horizon size at the time of the last scattering, hence the ℓ range at which the EE spectra become maximum is sensitive to mean redshift of reionization. The height of the reionization bump in the EE spectra is maximum around $\ell \approx 4$ for EERM whereas for tanh reionization model it is around $\ell \approx 3$. The shift is due to slight anticipation of the reionization process in the tanh model. However, the difference between EERM ad the tanh model is difficult to probe at the power spectrum level, as shown by the error bars on the EE spectra for the LiteBIRD sensitivity.

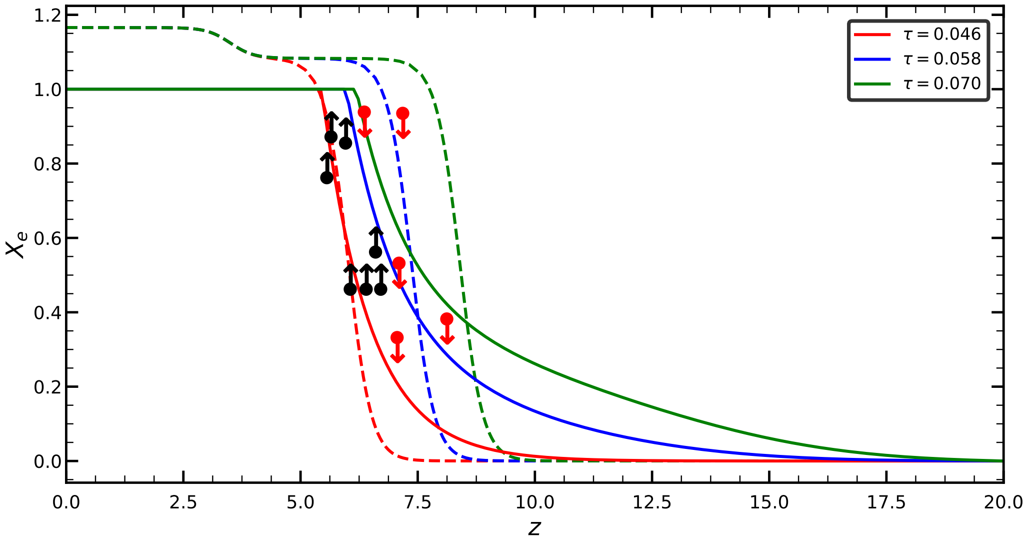

Figure 2.5: Solid lines represent the ionization history of the universe for three different optical depths considering EERM; the dashed lines are reionization histories calculated by the CLASS code using the tanh model for the same optical depths. Upper (red) and lower (black) observational limits from various data collected by [169].

2.3.2 Patchy Reionization

We now focus on morphological aspects of the reionization process, the three most new effects with respect to those discussed previously are the following.

First, since we are considering the inhomogeneous reionization, optical depth τ will be direction-dependent quantity in the CMB sky, and the temperature and polarization anisotropy from the last scattering surface gets screened by a factor of $e^{-\tau(\hat{n})}$ [178].

Second, new large scale polarization is generated as CMB local temperature quadrupole is scattered by the ionized regions, thereafter dubbed bubbles.

Third, the peculiar motion of the ionized bubbles induces additional temperature fluctuations by KSZ during the epoch of reionization. KSZ effect due to patchy reionization will generate new power on small scales (around $l \approx 3000$) [179, 66] in temperature power spectrum. In this Chapter, we will not consider KSZ contribution as our interest is investigating the polarization anisotropy due to patchy reionization.

We assume the reionization happened by the percolation of ionized HII bubles as well as the the growth in R [180, 181] inside the neutral intergalactic medium. We consider the size R of ionized bubbles following a log-normal distribution with two free parameters, the characteristic bubble size $\bar{R}$ (in Mpc) and the standard deviation σ_{lnr}, given by

$$P(R) = \frac{1}{R}\frac{1}{\sqrt{2\pi\sigma_{lnr}^2}} \exp\left[-\frac{\{\ln\left(R/\bar{R}\right)\}^2}{2\sigma_{lnr}^2}\right]. \tag{2.9}$$

A bias b in the dark matter halo distribution will also influence the number density

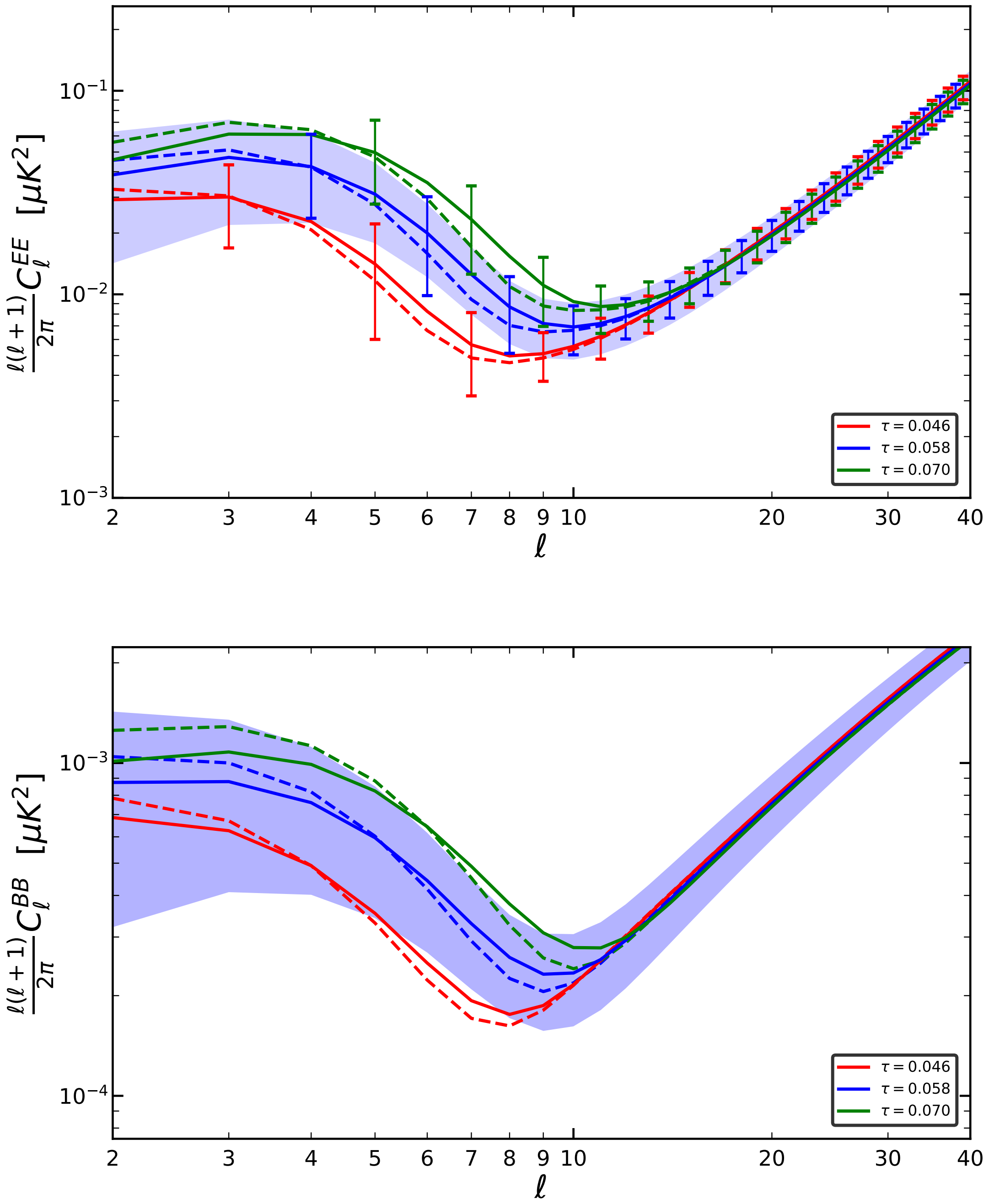

Figure 2.6: Upper panel: solid lines describe the EE power spectra for EERM and dashed lines for the tanh model, on adopting $\tau = 0.046$ (red), 0.058 (blue) and 0.070 (green). Shaded area shows the 1σ cosmic variance limit corresponding to $\tau = 0.058$. Errorbars refer to the LiteBIRD sensitivity. In the bottom panel we plot the corresponding BB spectra.

of ionized bubbles, but for simplicity we assume the bubble bias to be not evolving with

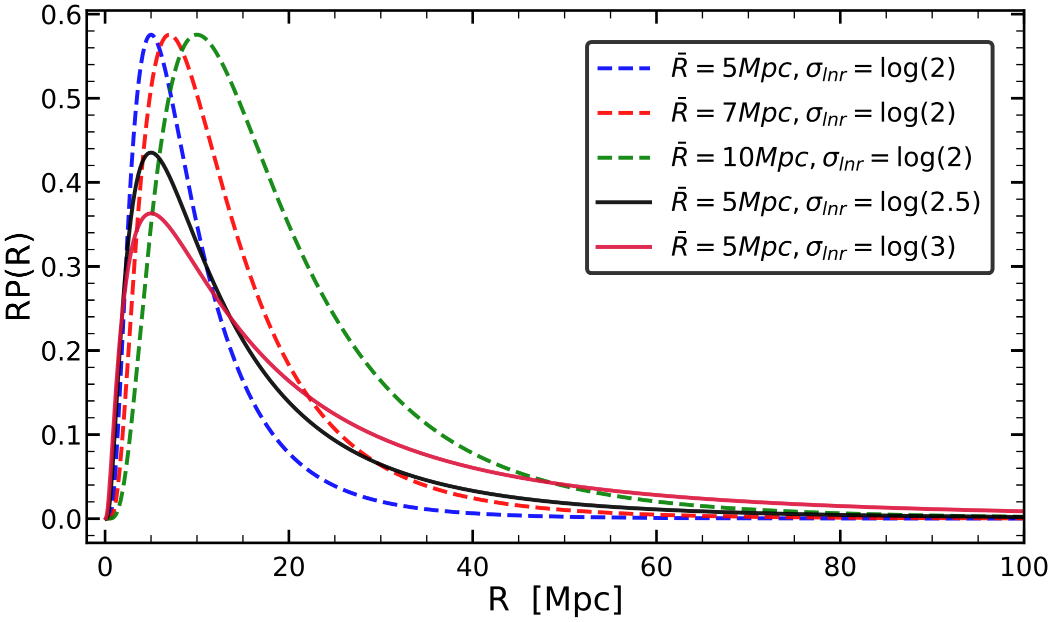

Figure 2.7: Distribution of bubble radius for different $\bar{R}$ and σ_{lnr} as reported.

redshift and independent of the bubble radius (in the redshift range of our interest); in this Chapter, we use $b = 6$. In Figure 2.7 we show the radial distribution of ionized bubbles for EERM where we consider various values of $\bar{R}$ and σ_{lnr}, be exploited in Section 2.5 to investigate how the reionization model affects the observables of patchy reionization. We stress that the radii distribution of bubbles strongly depends on the overall reionization history. For higher reionization, optical depth w.r.t the present case, the distribution of bubbles has been studied numerically considering the complicated evolution of ionized bubbles during the reionization epoch[182]. We will comment more on this point in the conclusion section.

The merging of ionization bubbles creates fluctuations in ionization fraction, $\delta x_e(\hat{\mathbf{n}}, \chi)$ over the mean ionization fraction $\bar{x}_e(\chi)$ during the inhomogeneous reionization epoch, so that

$$x_e(\hat{\mathbf{n}}, \chi) = \bar{x}_e(\chi) + \delta x_e(\hat{\mathbf{n}}, \chi), \tag{2.10}$$

$$\tau(\hat{\mathbf{n}}, \chi) = c\sigma_T n_{p0} \int_0^{\chi} \frac{d\chi}{a^2} \left[\bar{x}_e(\chi) + \delta x_e(\hat{\mathbf{n}}, \chi)\right]. \tag{2.11}$$

In order to quantify the fluctuations in the ionization fraction, three dimensional power spectrum is expressed by the sum of the 1-bubble and 2-bubble contributions in total power spectrum corresponding to the scales in which r≪R (1b) and r≫R (2b), respectively. The main assumption for calculating the power spectrum of δx_e is that fluctuations in free electron density trace the fluctuations in dark matter density [180]. We take analytic expressions of 1b and 2b contributions from [127], given by:

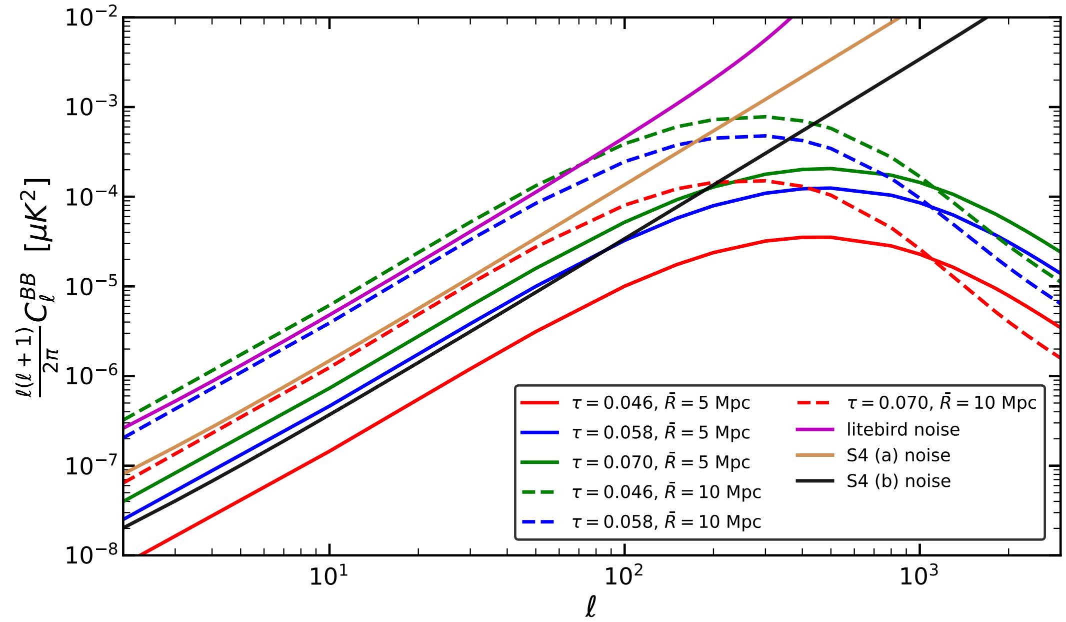

Figure 2.8: Green, Blue and red solid and dashed lines are B mode power spectrum generated due to patchy reionization for different values of τ and $\bar{R}$ as reported for EERM. Purple, orange and black solid lines are the noise level for the experimental configurations of LiteBIRD, CMB-S4 (a) and CMB-S4(b) respectively.

$$P^{1b}_{\delta x_e \delta x_e}(k) = x_e(1 - x_e)\left[\alpha(k) + \beta(k)\right], \tag{2.12}$$

where the functional forms of $\alpha(k)$ and $\beta(k)$ are given by

$$\alpha(k) = \frac{\int dRP(R)[V(R)W(KR)]^2}{\int dRP(R)V(R)}, \tag{2.13}$$

$$\beta(k) = \int \frac{d^3\mathbf{k}'}{(2\pi)^3} P\left(|\mathbf{k} - \mathbf{k}'|\right)\alpha(k'). \tag{2.14}$$

The volume of the bubble is $V(R) = \frac{4}{3}\pi R^3$ and matter power spectrum is P(k). $W(kR)$ is the Fourier transform of the tophat window function with radius R, given by

$$W(kR) = \frac{3}{(kR)^3}\left[\sin(kR) - kR\cos(kR)\right]. \tag{2.15}$$

We adopt the approximation from [181] to calculate $\beta(k)$ numerically, given by

$$\beta(k) = \frac{P(k)\sigma_R^2 \int dRP(R)V(R)}{[P^2(k) + \{\sigma_R^2 \int dRP(R)V(R)\}^2]^{1/2}}. \tag{2.16}$$

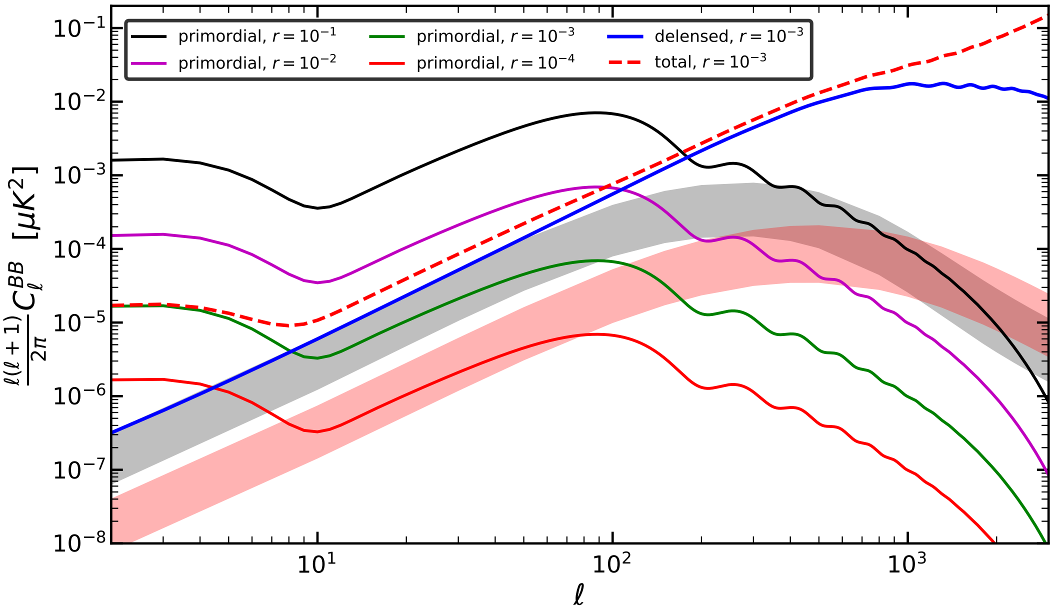

Figure 2.9: Black, magenta, green and red lines are the primordial B mode power spectrum for r=10^{-1}, 10^{-2}, 10^{-3},10^{-4} respectively. The blue solid line shows the de-lensed B-mode power spectrum for CMB-S4(a) sensitivity and $r = 10^{-3}$; the red dashed line adds the primordial signal and instrumental noise to the former.

The 2b contribution is given by

$$P^{2b}_{\delta x_e \delta x_e}(k) = \left[(1 - x_e)\ln(1 - x_e)\gamma(k) - x_e\right]^2 P(k), \tag{2.17}$$

where $\gamma(k)$ is defined by

$$\gamma(k) = b \cdot \frac{\int dRP(R)V(R)W(KR)}{\int dRP(R)V(R)}. \tag{2.18}$$

Therefore the total three dimensional power spectrum of δx_e can be written as

$$P_{\delta x_e \delta x_e}(k) = P^{1b}_{\delta x_e \delta x_e}(k) + P^{2b}_{\delta x_e \delta x_e}(k). \tag{2.19}$$

Now the optical depth power spectrum $C_\ell^{\tau\tau}$ can be constructed from Eq.(2.19). In the flat sky approximation it can be written using Limber approximation as

$$C_\ell^{\tau\tau} = \sigma_T^2 n_{p0}^2 \int \frac{d\chi}{a^4\chi^2} P_{\delta x_e \delta x_e}\left(\chi, k = \frac{\ell}{\chi}\right). \tag{2.20}$$

Inhomogeneous reionization is also the source of secondary anisotropies in the B mode polarization and the power spectrum can be connected also with $P_{\delta x_e \delta x_e}$ [183, 184] as

$$C_\ell^{BB-patchy} = \frac{3\sigma_T^2 n_{p0}^2}{100} \int \frac{d\chi}{a^4\chi^2} e^{-2\tau(\chi)} Q^2_{rms} P_{\delta x_e \delta x_e}\left(\chi, k = \frac{\ell}{\chi}\right). \tag{2.21}$$

,

Here Q_{rms} is the r.m.s temperature of the local quadrupole and we used $Q_{rms} = 22\ \mu K$ during the patchy reionization epoch to calculate $C_\ell^{BB-patchy}$. In Figure 2.8 we compare BB spectra from patchy reionization with the foreseen sensitivities from CMB-S4 and LiteBIRD. As it can be seen, the signal is at the noise level in both cases, requiring additional steps for increasing the signal to noise ratio, described in the next section. We can see in the figure that CMB-S4(a) sensitivity is a bit lower in $\ell \lesssim 200$ than the patchy BB signal both for $\tau = 0.070$ and $\tau = 0.058$ with $\bar{R} = 10$ Mpc. On the other hand, the LiteBIRD sensitivity is a bit higher than patchy BB signal for the same configuration. CMB-S4(b) noise level is almost the same with respect to the Patchy BB signal even with $\bar{R} = 5$ Mpc. This can be very useful in near future to constrain the morphology of the reionization by observing the patchy B mode signal. We also consider the contamination from patchy reionization to the B-mode power spectrum in figure 2.9. Adopting the model discussed in the present chapter and the 1σ bounds on τ from Planck, the contribution from patchy reionization is significant for $r < 10^{-3}$.

2.4 Reconstruction of τ along the line of sight

In Section 2.3.2 we discussed how patchy reionization induce additional structure in the observed CMB sky through τ fluctuations. We consider that T and $(Q \pm iU)$ are the temperature and polarization Stokes parameters before the start of reionization; then, at the end of the reionization, CMB temperature and polarization parameters will be changed as follow [127]:

$$T(\hat{\mathbf{n}}) = T_0(\hat{\mathbf{n}}) + \int \delta\tau T_1(\hat{\mathbf{n}}), \tag{2.22}$$

$$(Q \pm iU)(\hat{\mathbf{n}}) = (Q \pm iU)_0(\hat{\mathbf{n}}) + \int \delta\tau (Q \pm iU)_1(\hat{\mathbf{n}}), \tag{2.23}$$

Fluctuations in optical depth is given by:

$$\delta\tau = \int_{\chi_{start}}^{\chi_{end}} \frac{d\chi}{a^2} \delta x_e(\hat{\mathbf{n}}, \chi). \tag{2.24}$$

Where χ_{start} and χ_{end} are the comoving distances to the start and end of reionization respectively. $T_0(\hat{\mathbf{n}})$ and $(Q \pm iU)_0(\hat{\mathbf{n}})$ are the contributions coming from recombination and homogeneous reionization and $T_1(\hat{\mathbf{n}})$ and $(Q \pm iU)_1(\hat{\mathbf{n}})$ are the contribution from patchy reionization as defined in [127].

Separately we can write inhomogeneous screening terms as

$$T^{scr} = T_0(\hat{\mathbf{n}}) e^{-\delta\tau(\hat{\mathbf{n}})}, \tag{2.25}$$

$$(Q \pm iU)^{scr} = (Q \pm iU)_0(\hat{\mathbf{n}}) e^{-\delta\tau(\hat{\mathbf{n}})}, \tag{2.26}$$

accounting for the damping of anisotropies along the line of sight due to patchy reionization.

We now make a parallelism with the formalism applying to CMB lensing. The lensed field $S_{len}(\hat{\mathbf{n}})$ is related with the unlensed field $S_{unl}(\hat{\mathbf{n}})$ and the lensing potential ϕ as [48]

$$S_{len}(\hat{\mathbf{n}}) = S_{unl}(\hat{\mathbf{n}}) + (\nabla\phi)\nabla S_{unl}(\hat{\mathbf{n}}) + O[(\nabla\phi)^2], \tag{2.27}$$

so, it modulates both the CMB polarization and temperature by correlating different Fourier modes. In flat sky approximation, after the lensing reconstruction method [48, 127], this correlation for patchy reionization can be written as

$$\langle S(\vec{\ell}_1)S'(\vec{\ell}_2)\rangle = (2\pi)^2 C_\ell^{SS'}\delta(\vec{L}) + f^{\tau}_{SS'}(\vec{\ell}_1,\vec{\ell}_2)[\delta\tau(\vec{L})], \tag{2.28}$$

where S, S' can be any combinations of T,E and B and $\vec{L} = \vec{\ell}_1 + \vec{\ell}_2$. We use only EB minimum variance quadratic estimator since it provides the highest signal to noise ratio to patchy reionization [185, 127]. f^{τ}_{EB} for flat sky is given by [182]

$$f^{\tau}_{EB} = \left(\bar{C}^{EE}_{\ell_1} - \bar{C}^{BB}_{\ell_2}\right)\sin 2(\phi_{\ell_1} - \phi_{\ell_2}), \tag{2.29}$$

where $\bar{C}^{EE}_{\ell_1}$ and $\bar{C}^{BB}_{\ell_2}$ are the EE and BB power spectra which include patchy reionization and $\phi_\ell = \cos^{-1}(\hat{\mathbf{n}}\cdot\hat{\ell})$. To satisfy Eq.(2.28) we can write minimum variance quadratic estimator of $\tau(\vec{L})$ as

$$\widehat{\tau}_{EB}(\vec{L}) = \widetilde{N}^{\tau}_{EB}(\vec{L})\int\frac{d^2\vec{\ell}_1}{(2\pi)^2}\left[E(\vec{\ell}_1)B(\vec{\ell}_2)\right]F^{\tau}_{EB}(\vec{\ell}_1,\vec{\ell}_2), \tag{2.30}$$

where $\widetilde{N}^{\tau}_{EB}(\vec{L})$ is the zeroth order bias for τ reconstruction which can be thought in analogy to the $N^{(0)}_{EB}$ bias for lensing potential reconstruction, given by

$$\widetilde{N}^{\tau}_{EB}(\vec{L}) = \left[\int\frac{d^2\vec{\ell}_1}{(2\pi)^2}f^{\tau}_{EB}(\vec{\ell}_1,\vec{\ell}_2)F^{\tau}_{EB}(\vec{\ell}_1,\vec{\ell}_2)\right]^{-1}. \tag{2.31}$$

The CMB instrumental noise power spectrum for a Gaussian symmetric beam can be written as

$$N^P_\ell = \Delta^2_P \exp\left[\frac{\ell(\ell+1)\Theta^2_f}{8\ln 2}\right], \tag{2.32}$$

where Δ_P is the noise of the detector for polarization in μK-arcmin; This is $\sqrt{2}$ times bigger than the detector noise for temperature and Θ_f is the full width half maxima of the beam in arcmin units.

In order to minimize the variance of $\langle\widehat{\tau}_{EB}(\vec{\ell}_1)\widehat{\tau}_{EB}(\vec{\ell}_2)\rangle$, the optimal form of filter $F(\vec{\ell}_1,\vec{\ell}_2)$ for EB estimator is given by

$$F^{\tau}_{EB}(\vec{\ell}_1,\vec{\ell}_2) = \frac{f^{\tau}_{EB}(\vec{\ell}_1,\vec{\ell}_2)}{(C^{EE}_{\ell_1} + N^{EE}_{\ell_1})(C^{BB}_{\ell_2} + N^{BB}_{\ell_2})}, \tag{2.33}$$

So that the expectation value of the estimator for τ will reduce to

$$\langle \widehat{\tau}_{EB}(\vec{\ell}_1)\widehat{\tau}_{EB}(\vec{\ell}_2)\rangle = (2\pi)^2\delta(\vec{\ell}_1,\vec{\ell}_2)\left[C_L^{\tau\tau} + \widetilde{N}_{EB}^{\tau}(\vec{L})\right]. \tag{2.34}$$

We will use this technique in the next section to reconstruct the power spectrum of τ using EERM prescription.

2.5 Detectability of τ reconstruction in CMB-S4 CMB experiments

In this Section, we discuss the capabilities of future CMB polarization experiments to detect the angular pattern of τ. In order to do so we have modified the publicly available `Lenspix`[9] algorithm [186] to reconstruct τ instead of the GL potential ϕ following the algebra discussed in the previous Section. We focus on Eq.(2.20) in order to calculate the $C_\ell^{\tau\tau}$ for our reionization model, EERM.

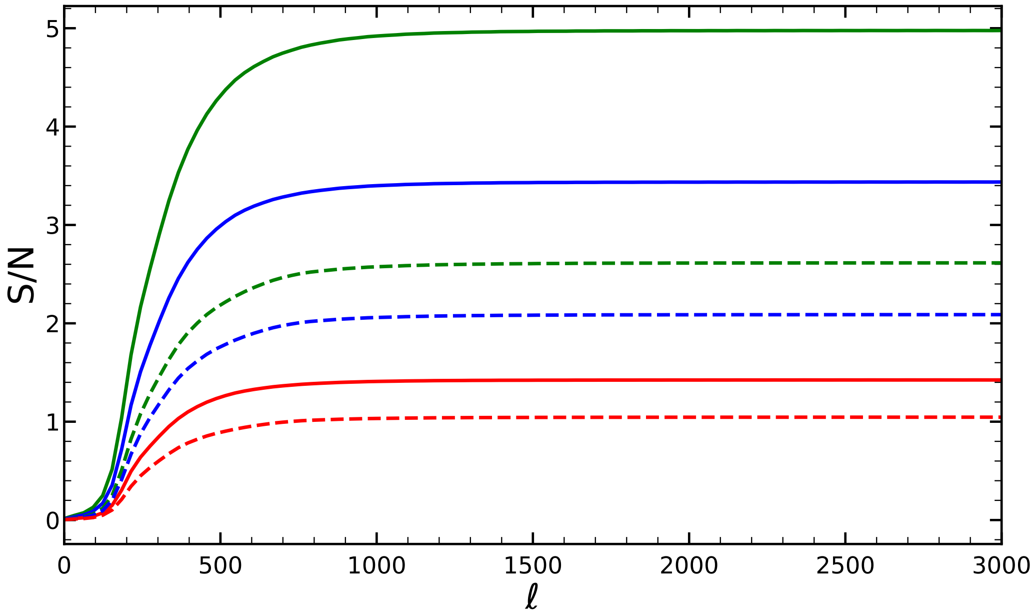

Figure 2.10: Solid lines represents the cumulative SNR for EERM and dashed lines for the tanh model with τ= 0.070 (green), 0.058 (blue) and 0.046 (red) respectively.

The uncertainty in the power spectrum of τ comes from both the astrophysical modelling of the source of reionization and the uncertainty due to the modelling of reionization morphology. The first source of uncertainty is connected with the mean (sky averaged) optical depth $\bar{\tau}$, escape fraction f_{esc} and the source of reionization, which in our case is

---

[9] cosmologist.info/lenspix

the star formation rate functions of high redshift galaxies. The morphology of reionization depends on the bias factor, the mean radius of bubbles $\bar{R}$ and also the spread of the distribution of bubbles radii which are quantified by σ_{lnr} for a log-normal distribution. We will consider the effects of $\bar{R}$, $\bar{\tau}$, and σ_{lnR} uncertainties on the power spectrum of τ for EERM, implementing a minimum variance quadratic estimator.

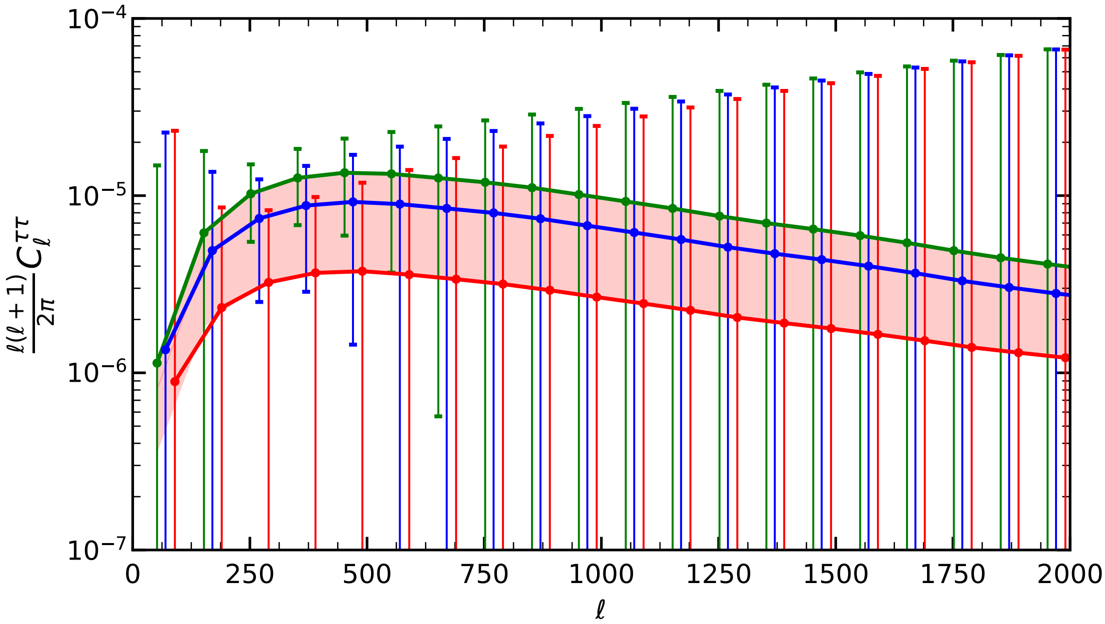

Figure 2.11: Green, blue and red solid lines represent the τ angular power spectra corresponding to $\bar{\tau} = 0.07, 0.058$ and 0.044, respectively with $\bar{R} = 5$ Mpc and $\sigma_{lnr} = \ln(2)$. We bin the each spectrum with $\Delta\ell = 100$ and show the error bars accordingly. The error bars are located at $l_{error} = (\ell_{min} + \frac{(2n-1)\Delta\ell}{2})$, where ℓ_{min} is the value of minimum ℓ and n is the bin index; we fix ℓ_{min} =2 (green curve), 20 (blue curve), 40 (red curve). Shaded pink area represents due to the 1σ error of the $\bar{\tau}$ measurement by Planck [159].

We calculate the Signal to Noise Ratio (SNR) to quantify the detectability of the patchy reionization:

$$\left(\frac{S}{N}\right) = \left[\frac{f_{sky}}{2}\sum_{l_{min}}^{l_{max}}(2\ell+1)\left(\frac{C_\ell^{\tau\tau}}{\widetilde{N}_\ell^{\tau\tau}}\right)^2\right]^{1/2}. \tag{2.35}$$

Here f_{sky} is the observed sky fraction for a particular experiment. We mainly focus on instrumental specifications corresponding to CMB-S4, for which we use $\Theta_f = 1$ arcmin and $\Delta_T = 1$ μK-arcmin, i.e $\Delta_P = \sqrt{2}$ μK-arcmin. We found that SNR for τ-reconstruction does not strongly depend on Θ_f as SNR changes a factor ≈ 3 when Θ_f increased from $1'$ to $5'$ but SNR increases by a factor of ≈ 80 by the decrease of Δ_T from 2 μK-arcmin to 0.5 μK-arcmin. We found and shown in Figure 2.10 that the EERM, featuring a more

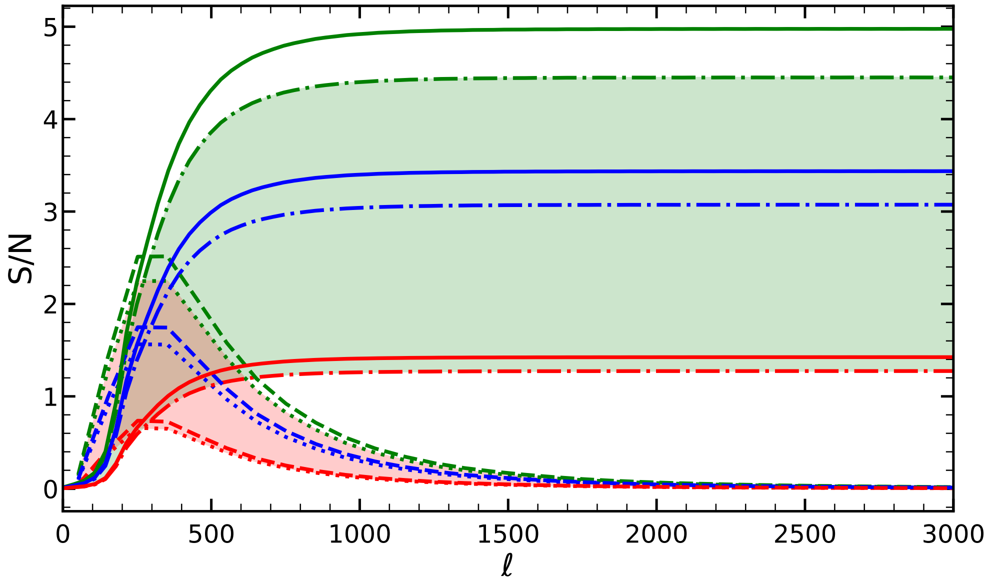

Figure 2.12: The binned and integrated SNR for the cases in Figure 2.12. Solid green, blue and red curve represent the integrated SNR for CMB-S4 sensitivity with $f_{sky} = 0.5$ for $\bar{\tau} = 0.07, 0.058, 0.044$, respectively, while the dashed dotted curves are for $f_{sky} = 0.4$. Dashed green, blue and red lines represent the SNR in each bin for $f_{sky} = 0.5$, while dotted lines are for $f_{sky} = 0.4$.

extended patchy reionization history, tend to yield higher SNR with respect to the tanh model.

2.5.1 Dependence on $\bar{\tau}$

In Figure 2.11 we compute $C_l^{\tau\tau}$ for three different optical depths, corresponding to the central value and $\pm 1\sigma$ of the most recent measurements from Planck, and with fixed reionization parameters $\bar{R} = 5\ Mpc$ and $\sigma_{lnr} = \ln(2)$. For $\bar{\tau} = 0.044$, the errors are too large at all scales for detectability, even for $f_{sky} = 0.4$. For $\bar{\tau} = 0.070$ and 0.058, an CMB-S4 experiment would be capable of probing τ fluctuations in multipole range $170 \lesssim \ell \lesssim 720$ and $190 \lesssim \ell \lesssim 630$, respectively, roughly corresponding to an interval from 1 to 1/3 of a degree. For a fixed detector sensitivity and beam resolving power, a measurement of the reionization morphology through $C_\ell^{\tau\tau}$ is simply proportional to the value of mean optical depth $\bar{\tau}$. If LITEBIRD [176] achieves its sensitivity goal of $\sigma(\bar{\tau}) = 0.002$, then this would provide an important prior for detecting and interpreting the inhomogeneous reionization signal.

In Figure 2.12, we plot the binned and integrated SNRs. Depending on the values of $\bar{\tau}$, the CMB-S4 specification should allow a $1.4 - 5\sigma$ detection of the signal. For $\tau = 0.44$, the SNR<1 at all ℓs in the binned spectra. For $\bar{\tau} = 0.7$ and $\bar{\tau} = 0.58$, S/N is greater than 1 in $152 \lesssim \ell \lesssim 752$ and $170 \lesssim \ell \lesssim 570$, respectively.

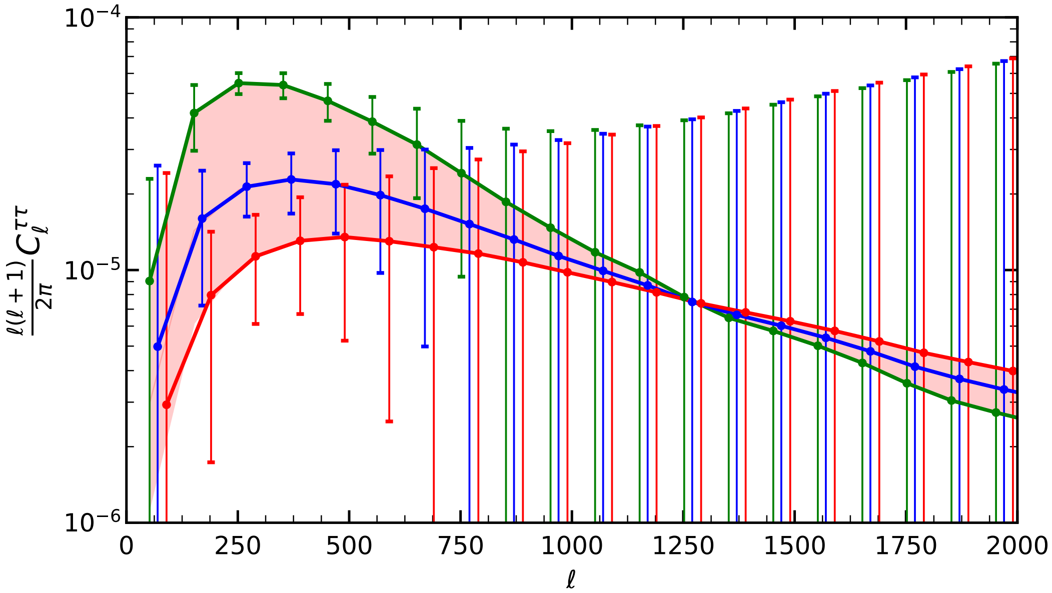

Figure 2.13: Green, blue and red solid lines are the τ spectra with $\bar{R} = 10, 7, 5$ Mpc, respectively, with $\sigma_{lnr} = \ln 2$ for $\bar{\tau} = 0.070$. The binning scheme is as in the previous figures.

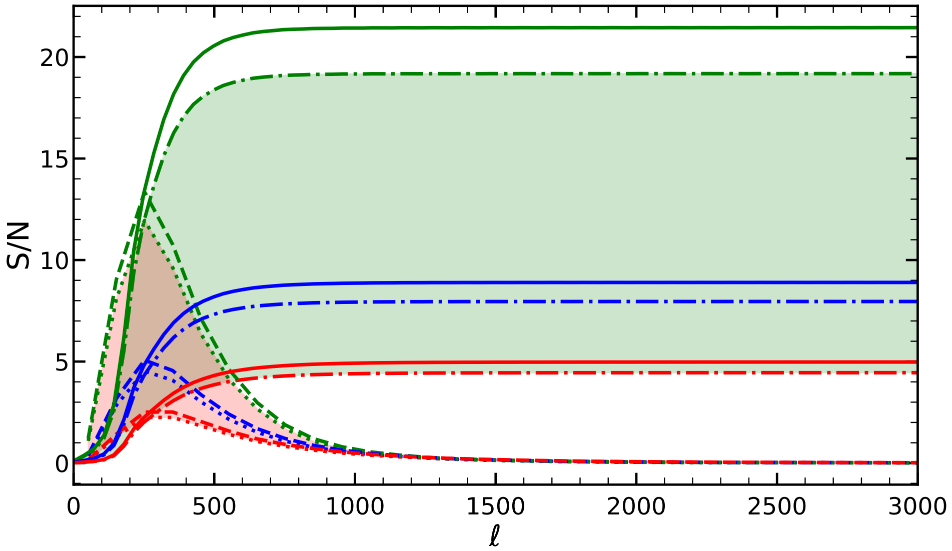

Figure 2.14: Binned and integrated SNR for the cases in Figure 2.13. Solid green, blue and red curve represent the integrated SNR for CMB-S4 sensitivity with $f_{sky} = 0.5$ for three optical depths ,$\bar{\tau} = 0.07, 0.058, 0.044$, respectively; dashed dot curves are for $f_{sky} = 0.4$ with the same configuration. Dashed green, blue and red lines are SNR in each bin for $f_{sky} = 0.5$, while dotted lines for $f_{sky} = 0.4$.

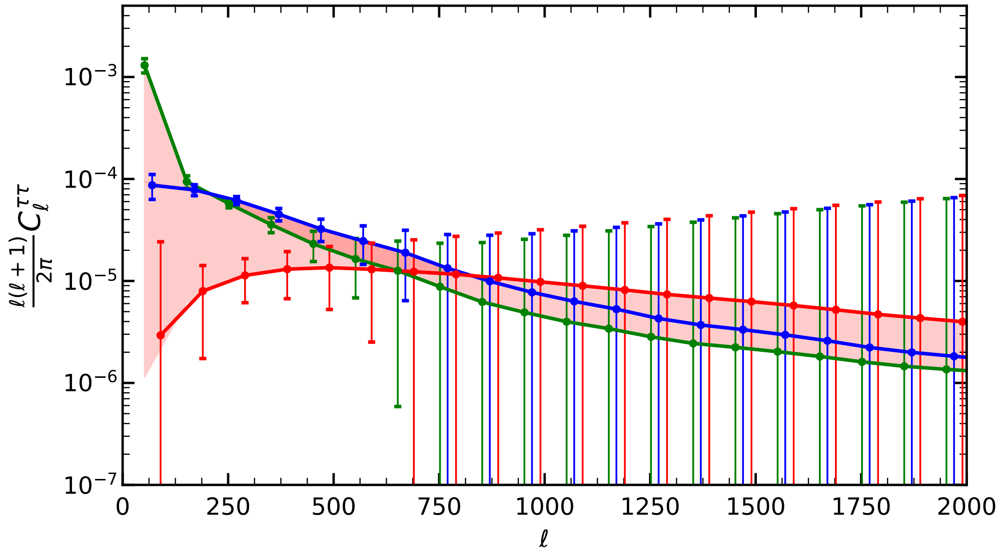

Figure 2.15: Green, blue and red solid lines are the τ spectra for $\sigma_{lnr} = ln3, ln2.5, ln3$, respectively, with $\bar{R} = 5$ Mpc for $\bar{\tau} = 0.070$. The binning scheme is as in the previous figures.

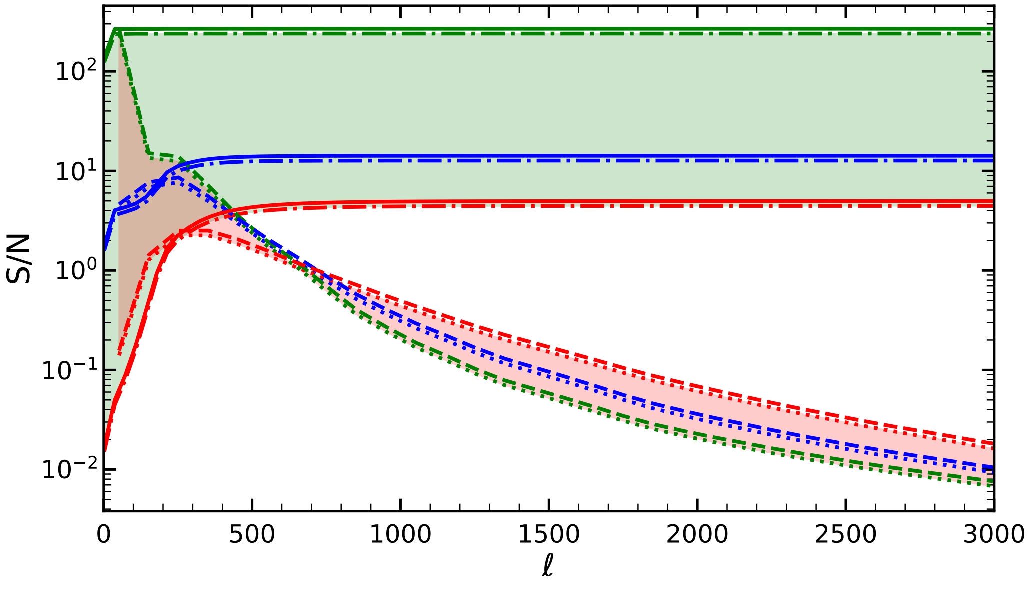

Figure 2.16: Binned and integrated SNR for the case in Figure 2.13. Solid green, blue and red curves represent the integrated SNR for CMB-S4 sensitivity with $f_{sky} = 0.5$ for three optical depths $\bar{\tau} = 0.07, 0.058, 0.044$, respectively, and dashed dotted curves are for $f_{sky} = 0.4$ with the same configuration. Dashed green, blue and red lines are SNR in each bin for $f_{sky} = 0.5$, while dotted lines for $f_{sky} = 0.4$.

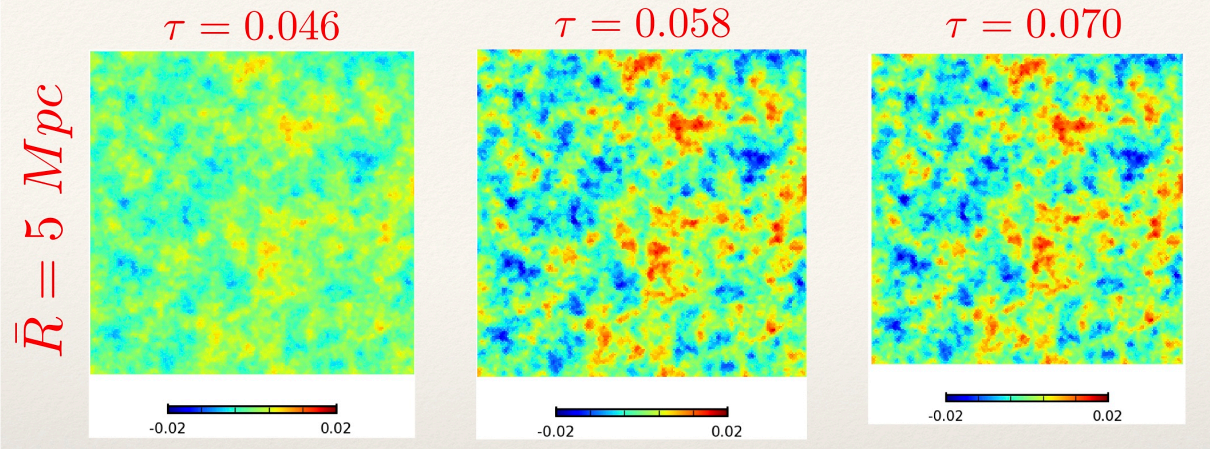

Figure 2.17: These maps show the fluctuations in optical depth. We fixed the parameters for bubble distribution, $\bar{R} = 5$ MPc and $\sigma_{\ln r} = \ln(2)$. We vary optical depths from $\tau = 0.046$ to $\tau = 0.070$. We used Healpy (https://healpy.readthedocs.io) package to produce these maps [187].

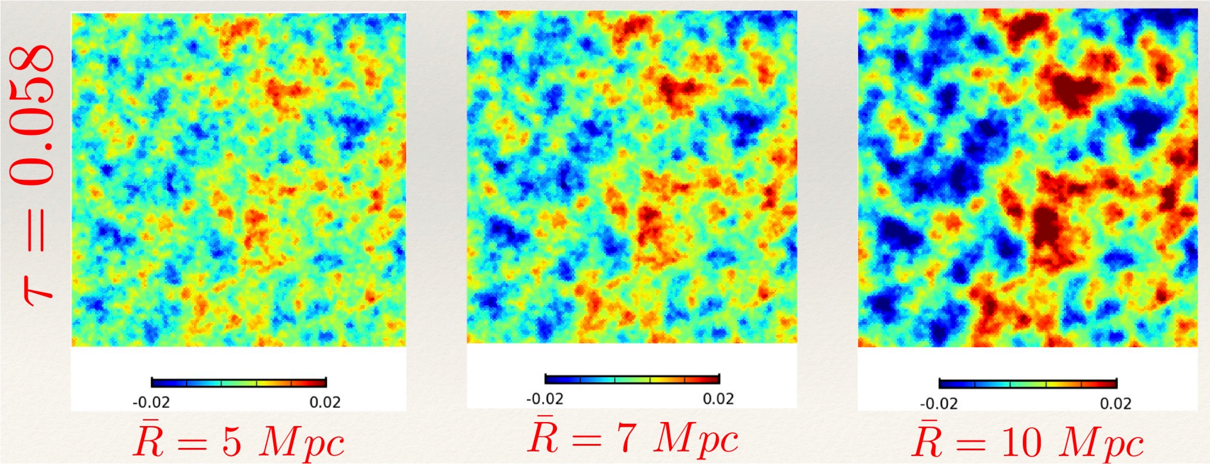

Figure 2.18: We show three optical depth fluctuation maps using Healpy package [187]. In this case, we fixed reionization history corresponding to $\tau = 0.058$. Then, We change the characteristic bubble sizes from $\bar{R} = 5$ Mpc to $\bar{R} = 10$ Mpc while keeping fixed the spread of bubble distribution, $\sigma_R = \ln(2)$.

2.5.2 Dependence on $\bar{R}$ and σ_{lnr}

The size and merger history of ionized bubbles is poorly understood. We consider the variation of reionization bubble radius $\bar{R}$ and the standard deviation of the log-normal distribution of σ_{lnr}.

If the bubbles are larger ($\bar{R} \approx 10$ Mpc), then the CMB-S4 can probe τ spectra in a wide range of ℓs as error bars are small in $52 \lesssim \ell \lesssim 852$ compared with the signal level. Whereas for $\bar{R} = 7$ Mpc and $\bar{R} = 5$ Mpc error bars are considerably larger than the signal level in the range of multipoles $70 \lesssim \ell \lesssim 770$ and $90 \lesssim \ell \lesssim 690$, respectively.

In Figure 2.14 we can see that as $\bar{R}$ increases, the integrated SNR also increases. In the range of $5 \lesssim \bar{R} \lesssim 10$ Mpc, the signature of patchy reionization can be measured with 4.3σ to 19.2σ by covering 40% of the sky and 4.8σ to 21.3σ by observing 50% of the sky.

In Figure 2.15 we can see that for $\sigma_{lnr} = \ln 3$ and $\sigma_{lnr} = \ln 2.5$, $C_\ell^{\tau\tau}$ can be measured in the range $52 \lesssim \ell \lesssim 652$ and $70 \lesssim \ell \lesssim 670$. In the Figure 2.16, the integrated SNR reaches 267 which is much larger than the variation of $\bar{R}$ and $\bar{\tau}$. Thus, due to the variation of σ_{lnr} in between $\ln 2$ to $\ln 3$,the CMB-S4 specifications would allow to detect patchy reionization with a confidence ranging from 4.8σ to 267σ.

We show the fluctuations of τ considering different reionization histories and the ionized bubble size distribution in Figure 2.17 and 2.18. The increase in τ increases the amplitude of the tau power spectra for fixed $\bar{R}$ and σ_{lnr}. The question comes if we can make a map of τ following the reconstruction method using data from the future CMB experiments. If SNR is sufficiently high τ map will be a direct probe of reionization. A map of τ will act as a template of the electron distribution in this Universe. Similar to the Compton y parameter map, τ map will also have the contributions from reionization (early time) and clusters (late time). In Figure 2.18 we can visualize that the τ fluctuations appears on the large scales with increase of $\bar{R}$. Making a map of τ will be able to constrain parameters of reionization such as $\bar{R}$, σ_{lnr} and $\bar{\tau}$.

2.6 Summary and Outlook

Cosmic reionization should be inhomogeneous with large ionized regions embedded in a shrinking neutral phase. This inhomogeneous reionization should produce a detectable signal. With its unprecedented sensitivity, CMB-S4 should be capable of detecting the signal at a minimum, constraining the physics of reionization.

In this Chapter, we have constructed an ionizing background history that is based on recent astrophysical observations. We have adopted a simple parametrization of the size distribution of the early ionized regions; specifically, we use a log-normal distribution in radius, characterized by a mean radius and a spread. The sky pattern of the reionization in such a picture is commonly known as patchy.

Following earlier works, we have implemented a procedure for the extraction of the patchy reionization signal analogue to the one exploited for CMB lensing and evaluated the signal to noise ratio achievable by CMB experiments reaching the CMB-S4 capabilities. The angular power spectrum is distributed broadly around the degree scale, with a long tail at higher multipoles. We have studied the amplitude of the signal as a function of the overall properties of the bubbles, and in particular on the abundance of the largest ones. If the bubble distribution has a tail with bubble size extending to tens of Mpc, then CMB-S4 SNR could be in the many tens to hundreds.

Because our predicted signal is one order of magnitude larger than that estimated by [182], lensing noise contamination should be a less relevant issue for us. Since the lensing behaviour is known for a given set of cosmological parameters, we can remove its contamination from our signal. These results demonstrate the capability of future CMB experiments to detect patchy reionization contribution to the CMB anisotropies. We will come back to the future perspectives of these studies in the last Chapter.

Chapter 3

Detectability of τ-21cm cross-correlated signal

> Science doesn't always go forwards.
> It's a bit like doing a Rubik's cube.
> You sometimes have to make more of
> a mess with a Rubik's cube before
> you can get it to go right.
>
> *Jocelyn Bell Burnell*

3.1 Introduction

In the present Chapter, we forecast the future detectability of the cross-correlation between fluctuations in τ as probed by CMB experiments, and fluctuations in the 21cm brightness at a given redshift as probed by radio interferometers. We also investigate the power of such $\tau - 21$ cross-correlation in probing tomographically the patchiness of the cosmic reionization.

The most recent measurements from the experiment provide increasingly tight constraints on the optical depth to reionization: $\tau = 0.058 \pm 0.012$ and $\tau = 0.054 \pm 0.0073$ according to the 2016 and 2018 Planck data releases [188, 13], respectively, and suggest that the reionization process has been completed at redshift $z \sim 6-8$. However, such a quantity probes the integrated effect of the ionization history along the line of sight, but it can constrain neither the detailed physics of the reionization process nor its temporal evolution and duration.

Recent determinations of the UV luminosity function out to $z \sim 10$ strongly suggest that faint high-redshift galaxies constitute the main sources of cosmic reionization. [119] have shown that, integrating the observed galaxy luminosity function down to a UV magnitude limit $M_{UV} \sim -13$ and assuming a standard initial mass function as well as reasonable values of the escape fraction $f_{\rm esc} \lesssim 10\%$ for ionizing photons from primeval galaxies yields a reionization history consistent with Planck's optical depth measurements and by several other independent astrophysical observables (e.g., Lyman-α forest transmission profiles, sizes of quasar near zones, gamma-ray bursts (GRB) damping wing absorption profiles, abundance and clustering of Lyman-α emitters, size evolution of Lyman-α halos, photoionization rates inferred from quasar proximity effect). Additional sources like AGNs and quasars may provide a minor contribution, since the number density of bright ones falls quickly above $z > 6$ and the ionization power of fainter ones is insufficient to ionize the Intergalactic Medium (IGM), unless extreme values of the associated escape fraction (around 100%) are adopted [117, 118].

During the EoR the gas distribution is expected to be highly inhomogeneous [189, 190, 191]. These inhomogeneities imply that the ionization fraction is a spatially varying quantity at a given redshift. As τ depends on the column density of free electrons along the line of sight, the patchy nature of reionization generates fluctuations in the optical depth. Patchy reionization also produces secondary anisotropies in the CMB via kSZ effect, related to the peculiar motion of ionized bubbles [192, 127]. Investigating the patchiness and morphology of the reionization process could provide crucial information on the astrophysical properties of the primeval galaxies, and on the distribution of ionized and neutral matter during the cosmic dawn.

Future CMB experiments will significantly surpass the Planck mission in sensitivity for temperature and polarization. These experiments have the potential to directly probe the patchiness in cosmic reionization by measuring non-Gaussian features imprinted on the CMB polarization [127, 107, 193]. Complementary observations from radio-arrays like Hydrogen Epoch of Reionization Array[1](HERA) and Square Killiometer Array[2](SKA) operating in the MHz frequency range, will measure the 21cm angular distribution and power, so providing robust constraints on the distribution of HI gas out to very high redshifts.

Since 21cm observations trace the evolution of neutral hydrogen HI and CMB observations of τ trace the evolution of ionized hydrogen, it is expected that these probes are complementary to each other [194, 195, 196], and that their cross-correlation can greatly improve our knowledge of the cosmic reionization process. Cross-correlating τ and 21cm observations can reduce the impact on systematic effects (e.g., related to foregrounds), and provide a tomographic mapping of the reionization process, allowed by the narrow frequency resolution of the 21cm radio arrays.

The plan of the chapter is the following: in Section 3.2 we describe our model of reionization; in Section 3.3 we define the observables entering our analysis, i.e., the 21cm brightness temperature fluctuations δT_b and the optical depth for electron scattering τ, and provide the theoretical background for the $\tau-21$ cross correlation in terms of reionization morphology and of angular power spectrum; in Section 3.4 we discuss the detectability of the $\tau - 21$ cross correlation by future CMB experiments and radio arrays, and its dependence on various parameters describing reionization history and morphology; we calculated angular cross power spectra of tSZ and τ in Section 3.5 and finally, in Section

---

[1] https://reionization.org/

[2] https://www.skatelescope.org/

3.6 we summarize our findings.

3.2 Reionization model

Figure 3.1 shows the reionization history computed from our SFR density integrated down to different UV magnitude limits $M_{\rm UV}^{\rm lim}$, assuming a standard value $f_{\rm esc} \approx 6\%$ for the escape fraction of ionizing photons. For $M_{\rm UV}^{\rm lim} \approx -13$, the result (black dot-dashed line) agrees with the UV value of the optical depth for electron scattering $\tau \approx 0.054$ recently measured by the Planck [13]. For reference, the dotted line represents the optical depth expected in a fully ionized Universe up to redshift z; this is to show that the bulk of the reionization process occurred at $z \sim 6-8$ [see 173].

Adopting $M_{\rm UV}^{\rm lim} \approx -17$ corresponds to the observational limits of current blank-field UV surveys at $z \gtrsim 6$ and the optical depth (solid black line) approaches the lower boundary of the 2σ region allowed by Planck data. On the other end, assuming $M_{\rm UV}^{\rm lim} \approx -12$ makes the resulting optical depth (black dashed line) to approach the upper boundary of the 2σ region from Planck measurements. We will exploit these three reionization histories, bracketing the Planck measurements, in the $\tau - 21$ cross-correlation analysis.

3.3 τ-21 cross correlation

In this Section we discuss how patchy reionization generates fluctuations in the optical depth as well as in the 21 cm brightness temperature.

3.3.1 Basic quantities: $\delta\tau$ and δT_b

The optical depth of the neutral hydrogen medium to the hyperfine transition,τ_{21}, is given by [197],

$$\tau_{21} = \frac{3c^3\hbar}{16k\nu_{21}^2}\frac{A_{10}n_H x_H}{T_S H(z)}\,. \tag{3.1}$$

Here ν_{21} is the rest-frame frequency of the 21cm hyperfine transition line, $A_{10} = 2.85 \times 10^{-15}\ s^{-1}$ is the spontaneous emission coefficient, T_S is the spin temperature which regulates the intensity of the radiation, n_H is the neutral hydrogen density and x_H is the neutral hydrogen fraction.

The 21cm brightness temperature fluctuation, δT_b, is the difference between the redshifted 21cm brightness temperature, $T_b(z)$, and the redshifted CMB sky-averaged temperature, $T_{CMB}(z) = T_0\,(1+z)$ K, where $T_0 \approx 2.73$ K is the CMB temperature at $z = 0$. For small values of the optical depth δT_b is given by [198]

$$\delta T_b \approx \frac{T_S - T_{CMB}}{1+z}\,\tau_{21}\,. \tag{3.2}$$

During the reionization process, both the neutral hydrogen fraction, n_H, and the optical depth, τ_{21}, depend on the line of sight direction, $\hat{\mathbf{n}}$, implying the same for δT_b. Eq. (3.2)

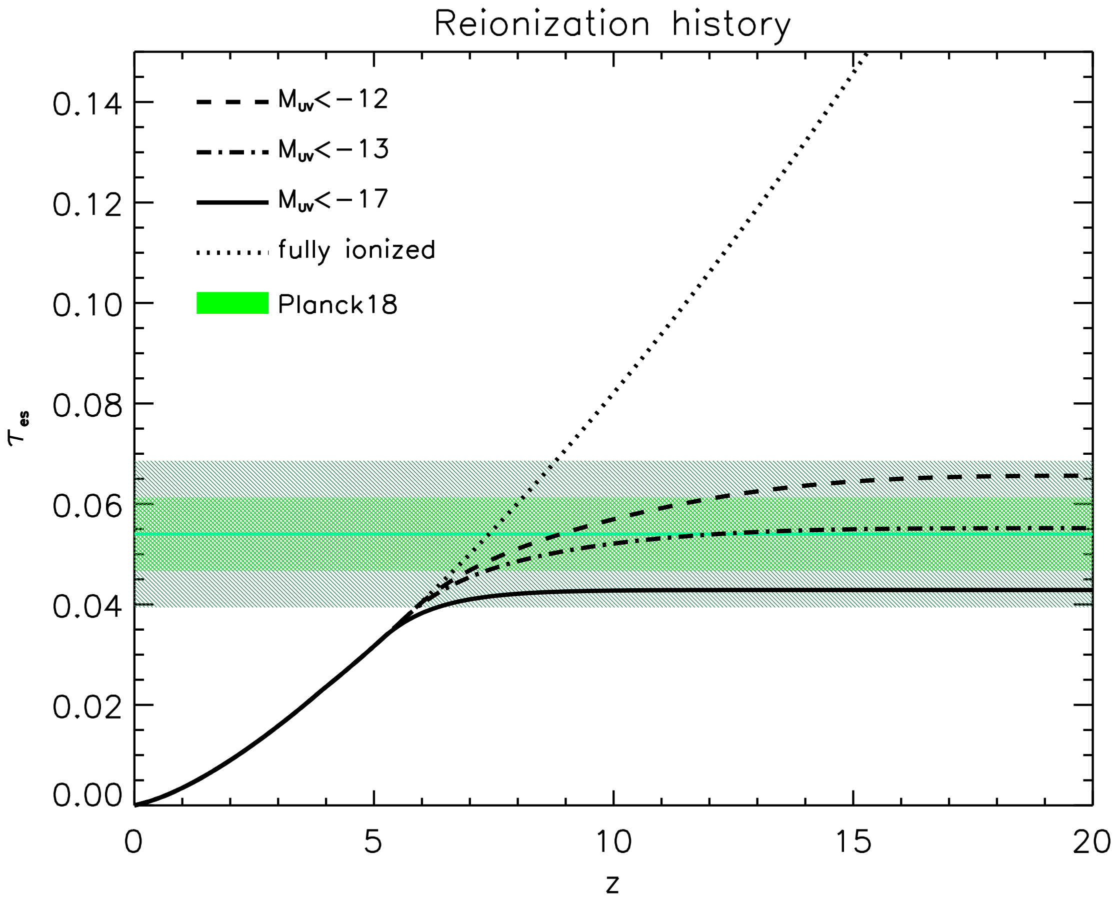

Figure 3.1: Reionization history of the Universe, in terms of the redshift evolution of the optical depth τ for electron scattering. Thick solid, dot-dashed and dashed lines represent our fiducial model for the SFR density integrated down to UV-magnitude limits $M_{UV} \approx -17$, -13, and -12, respectively. For reference, the dotted line refers to a fully ionized universe up to redshift z. The green line shows the measurement (with the 1σ and 2σ uncertainty regions highlighted by the dark and light green areas respectively) from the Planck collaboration 2018 [13].

can be recast into [199]

$$\delta T_b(z,\hat{\mathbf{n}}) = 27\,\mathrm{mK}\,(1{+}\delta_b)\,x_H(z,\hat{\mathbf{n}})\,\left[\frac{T_S - T_{CMB}}{T_S}\right]\left[\frac{1-Y_P}{1-0.248}\right]\left[\frac{\Omega_b}{0.044}\right]\left[\left(\frac{0.27}{\Omega_m}\right)\left(\frac{1+z}{10}\right)\right]^{1/2}, \tag{3.3}$$

here δ_b is the baryon overdensity and Y_P is the primordial helium fraction. Free electrons generated at the reionization epoch come from both hydrogen and helium ionization, so that $x_e(z) = n_e/[n_b(1-Y_P)]$.

On the other hand, the CMB sky-averaged optical depth for electron-scattering is proportional to the free electron density along the line of sight:

$$\tau(z) = c\sigma_T \int_0^z \bar{n}_e(z')dz' \frac{dt}{dz'} \,, \tag{3.4}$$

where $dt/dz = [H(z)(1+z)]^{-1}$ holds in terms of the Hubble parameter $H(z) = [\Omega_M\,(1+z)^3 + \Omega_\Lambda]^{1/2}$, and $\bar{n}_e(z) = n_{p0}\,(1+z)^3\,x_e(z)$ is the mean free electron number density in terms of the present number density of protons n_{p0}.

From the physical point of view τ probes the free electron density (via x_e) whereas δT_b probes the neutral hydrogen density (via x_H) along the line of sight; thus it is easily understood that these quantities are complementary to each other and and are related by $x_e(z) = 1 - x_H(z)$. As a consequence, fluctuations δT_b in the 21cm brightness temperature are connected to fluctuations $\delta\tau$ in the optical depth; such a link can be expressed for $T_S > T_{CMB}$ as [200, 199]

$$\delta\tau = \left(1 - \frac{3}{4}Y_P\right) \frac{\sigma_T \rho_{b0}}{m_p H_0 \Omega_m^{-0.5}} \int dz \left[(1+z)^{\frac{1}{2}}\delta_b - \frac{\delta T_b(z)}{8.5MK}\right] . \tag{3.5}$$

This relation is routinely exploited to build the halo model of the $\tau - 21$ cross-correlation presented below, that we will then use to forecast the detectability of the signal.

3.3.2 Morphology of reionization

In order to express the fluctuations $\delta\tau$ and δT_b in a dimensionless way, we introduce the brightness temperature field Ψ and ionization fraction field X:

$$\Psi(z, \hat{\mathbf{n}}) = \frac{T_S(z) - T_{CMB}(z)}{T_S(z)}\,(1+\delta_b)x_H(z, \hat{\mathbf{n}})\,, \tag{3.6}$$

$$X(z, \hat{\mathbf{n}}) = (1+\delta_b)\,x_e(z, \hat{\mathbf{n}})\,. \tag{3.7}$$

We assume the standard picture envisaging that ionizing sources (e.g., galaxies in our framework) start to ionize the surrounding regions via closely spherical bubbles. As time passes, ionized bubbles progressively overlap and then merge, inducing a complete reionization of the Universe. For the sake of definiteness and simplicity, we describe the morphology of the process by assuming a log-normal distribution of the bubble sizes, characterized by a mean $\bar{R}$ and by a 1σ dispersion $\sigma_{\rm lnr}$; in formulas, the size distribution reads

$$P(R) = \frac{1}{R}\frac{1}{\sqrt{2\pi\sigma_{\rm lnr}^2}} \exp\left[-\frac{\{\ln\left(R/\bar{R}\right)\}^2}{2\sigma_{\rm lnr}^2}\right] . \tag{3.8}$$

The three-dimensional power spectrum of the cross correlation between the fluctuation field $\delta\Psi$ and δX can be decomposed into two terms:

$$P_{\delta X \delta\Psi}(k) = P^{1b}_{\delta X \delta\Psi}(k) + P^{2b}_{\delta X \delta\Psi}(k)\,, \tag{3.9}$$

where $P^{1b}_{\delta X\delta\Psi}$ is the 1-bubble contribution coming from the distribution of neutral and ionized regions inside an individual bubble, and $P^{2b}_{\delta X\delta\Psi}$ is the 2-bubble contribution from regions located in different bubbles.

The 1-bubble term can be expressed as [201]

$$P^{1b}_{\delta X\delta\Psi}(k) = -x_e(1-x_e)\left[\alpha(k)+\beta(k)\right], \tag{3.10}$$

where the quantity $\alpha(k)$ and $\beta(k)$ are given by

$$\alpha(k) = \frac{\int dRP(R)[V(R)W(KR)]^2}{\int dRP(R)V(R)}, \tag{3.11}$$

$$\beta(k) = \int \frac{d^3\mathbf{k}'}{(2\pi)^3} P\left(|\mathbf{k}-\mathbf{k}'|\right)\alpha(k'), \tag{3.12}$$

and involve the matter power spectrum $P(k)$, the volume of $V(R) = \frac{4}{3}\pi R^3$ of a bubble with size R, and a filtering window function (Fourier transform of a tophat in real space) expressed as;

$$W(kR) = 3\,(kR)^{-3}\left[\sin(kR) - kR\cos(kR)\right]. \tag{3.13}$$

We adopt the approximation from [201] and calculate $\beta(k)$ as

$$\beta(k) = \frac{P(k)\sigma_R^2\int dRP(R)V(R)}{[P^2(k) + \{\sigma_R^2\int dRP(R)V(R)\}^2]^{1/2}}, \tag{3.14}$$

in terms of the mass variance σ_R of the matter power spectrum filtered on the scale R.

In addition, the 2-bubble term is given by

$$P^{2b}_{X\Psi}(k) = \left[(1-x_e)\ln(1-x_e)\gamma(k) - x_e\right]^2 P(k), \tag{3.15}$$

where $\gamma(k)$ is defined as

$$\gamma(k) = b\cdot\frac{\int dRP(R)V(R)W(KR)}{\int dRP(R)V(R)}, \tag{3.16}$$

and involves the clustering bias b of the ionized bubble with respect to the spatially-average matter density. Hereafter we consider a linear bias with a fixed value $b \approx 6$ [201].

3.3.3 Angular Power Spectrum

We now translate the above three-dimensional expressions into an angular power spectrum on the sky, by the usual multipole expansions via spherical harmonics $Y_{\ell m}$.

For the 21cm brightness temperature fluctuations the harmonic coefficients are given by

$$a^{21}_{\ell m} = 4\pi(-i)^\ell \int \frac{d^3k}{(2\pi)^3}\,\delta\Psi(k)\,I^{21}_\ell(k)Y^\star_{lm} \tag{3.17}$$

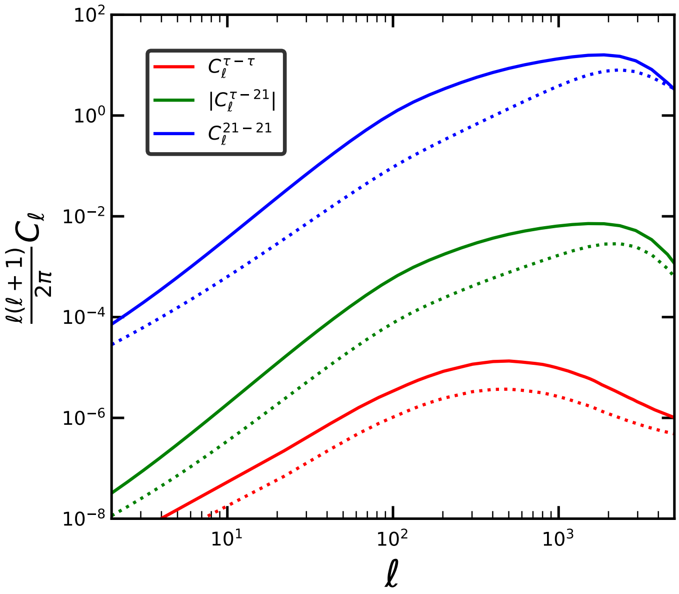

Figure 3.2: Auto and cross power spectra of the τ and 21cm fluctuations, by adopting a spatially-averaged value of the optical depth $\tau = 0.054$, and bubble size distribution parameters $\bar{R} = 5$ Mpc and $\sigma_{\rm lnr} = log(2)$, see the text for details. For the cross spectrum, the 1- and 2-bubble contributions are highlighted as dashed and dotted lines, respectively.

where

$$I_\ell^{21}(k) = T_0(z) \int_0^\infty d\chi' W_\chi(z_{obs}, \chi') J_\ell(k\chi') \, ; \tag{3.18}$$

here χ is the comoving distance to redshift z, and $W_\chi(z_{obs})$ is an observational Gaussian band filter centered at $z = z_{obs}$. It accounts for the fact that any ground-based radio array has a narrow frequency resolution, that in turn determines a resolution in redshift or comoving distance

$$d\chi = \left(\frac{\Delta\nu}{0.1MHZ}\right)\left(\frac{\Omega_m \, h^2}{0.15}\right)\left(\frac{1+z_{obs}}{10}\right)^{1/2} , \tag{3.19}$$

this is relevant in empowering a tomographic analysis of the cross-correlation signal. In the Limber approximation the auto-power spectrum is written then as

$$C_\ell^{2121} = T_0^2(z) \int \frac{d\chi}{\chi^2} W_\chi^2(z_{obs}, \chi') \, P_{\delta\Psi\delta\Psi}\left(\chi, k = \frac{\ell}{\chi}\right) , \tag{3.20}$$

where $P_{\delta\Psi\delta\Psi}$ is the power spectra of the 21cm fluctuations $\delta\Psi$. For the optical depth field the harmonic coefficients are given by

$$a_{\ell m}^\tau = 4\pi i^\ell \int \frac{d^3k}{(2\pi)^3} X(k) I_\ell^\tau(k) Y_{lm}^\star \tag{3.21}$$

where

$$I_\ell^\tau(k) = n_{p0}\sigma_T \int \frac{d\chi'}{a^2} J_l(k\chi')\,. \tag{3.22}$$

The related angular auto power spectrum can be written as:

$$C_\ell^{\tau\tau} = \sigma_T^2 n_{p0}^2 \int \frac{d\chi}{a^4\chi^2}\, P_{\delta X\delta X}\left(\chi, k = \frac{\ell}{\chi}\right)\,, \tag{3.23}$$

where $P_{\delta X\delta X}$ is the power spectra of the free electron density fluctuations δX.

Finally, the cross-correlation angular power spectrum reads

$$\langle a_{\ell m}^{\tau} a_{\ell m}^{21*}\rangle = \int \frac{dk}{k}\left[\frac{k^3 P_{X\Psi}}{2\pi^2}\right] I_\ell^\tau(k) I_\ell^{21}(k) \tag{3.24}$$

and in terms of the usual C_ℓ coefficients can be written as [199]

$$C_\ell^{\tau 21} = T_0(z) n_{p0}\sigma_T \int_0^\infty \frac{dz'}{H^2(z)}\left|\frac{d\chi}{dz}\right|^{-1}\left(\frac{1+z'_{obs}}{10}\right)^2 W(z_{obs}, \chi(z')) P_{X\Psi}\left(k = \frac{\ell}{\chi}, z'\right)\,. \tag{3.25}$$

We show in Figure 2 the auto and angular power spectra $C_\ell^{\tau\tau}$, C_ℓ^{2121} and $|C_\ell^{\tau 21}|$ at redshift $z \approx 7$ for the Planck best fit determination of the spatially-averaged optical depth $\tau \approx 0.054$, and bubble size distribution with parameters $\bar{R} = 5$ Mpc and $\sigma_{\mathrm{lnr}} = \log(2)$. In the cross-correlation, we have highlighted the 1-and 2-bubble contribution, that dominates the overall power spectrum at small (large) and large (small) scales (multipoles), with a crossing around the multipole corresponding to the average bubble size divided by cosmological distances.

In Figure 3, the $\tau - 21$ cross spectrum is illustrated as a function of redshift, for the same parameters reported above. The cross-correlation signal is negative, featuring an inverse bell shape with a minimum at around the multipole corresponding to the average size of the ionizing bubbles, and a width mirroring that of the bubble size distribution. The depth of the minimum is maximal at the redshift where the ionizing fraction is around 50% and then becomes shallower in moving at lower and at higher redshift; the cross power spectrum vanishes in a wholly neutral or completely ionized Universe. These two figures show that measurements of the cross-spectrum would yield the detailed ionization history of the Universe.

3.4 Detectability of $\tau - 21$ cross correlation

We now turn to discuss the detectability of the $\tau - 21$ cross correlation. The uncertainty of the angular cross power spectrum can be calculated as

$$(\Delta C_\ell^{\tau 21})^2 = \frac{1}{(2\ell+1)f_{sky}}\left[(C_\ell^{\tau 21})^2 + (C_\ell^{\tau\tau} + N_\ell^{\tau\tau})(C_\ell^{2121} + N_\ell^{2121})\right]\,; \tag{3.26}$$

where f_{sky} is the observed sky fraction, $C_\ell^{\tau\tau}$ and C_ℓ^{2121} are the optical depth and 21cm brightness temperature fluctuation auto power spectra, corresponding to the reionization history and morphology described in previous Sections, and $N_\ell^{\tau\tau}$, N_ℓ^{2121} are the corresponding noise power spectra.

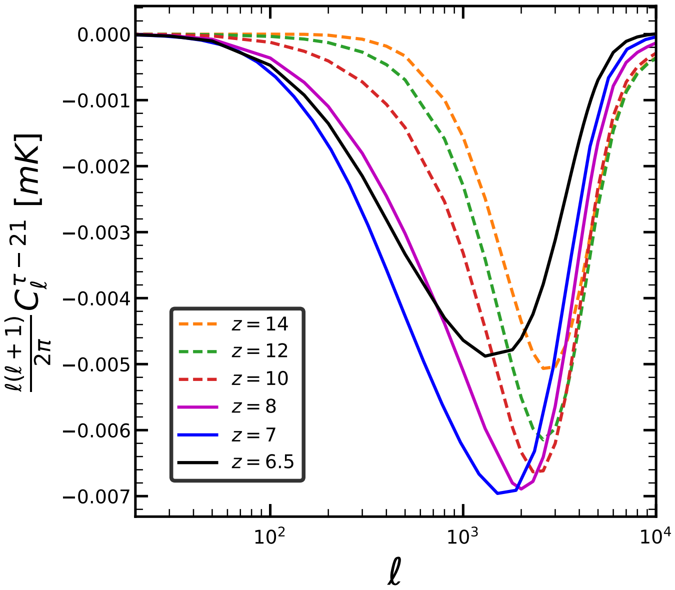

Figure 3.3: Redshift evolution of the cross power spectrum $C_\ell^{\tau-21}$, around the reionization redshift $z \approx 7$; parameters are as in previous Figure.

Fluctuations in τ are probed through measuring the amplitude of $E - B$ polarization correlations: the noise associated with this term is expressed by the reconstruction noise $N_\ell^{\tau\tau}$. Following [127], we compute $N_\ell^{\tau\tau}$. This term depends on both the reionization history and morphology, as well as on the instrumental noise of a given CMB experiment. The latter is given by

$$N_\ell^P = \Delta_P^2 \exp\left[\frac{\ell(\ell+1)\Theta_f^2}{8\ln(2)}\right] , \tag{3.27}$$

where Δ_P is the noise of the polarization detector in units of μK-arcmin (which is $\sqrt{2}$ times bigger than the detector noise for temperature), and Θ_f is the FWHM of the beam. Using this instrumental noise, we compute $N_\ell^{\tau\tau}$ following the prescription by [127].

N_ℓ^{2121} should include both the radiometer noise and a noise contribution from 21cm foreground. Since the foreground noise is poorly understood, we will ignore it here. This makes our signal to noise ratio (SNR) estimates optimistic and dependent on the ability of the 21cm experiment to remove foregrounds.

The Signal to Noise Ratio (SNR) for the detectability of the $C_\ell^{\tau-21}$ cross correlation signal is computed, in cumulative terms, as [202]

$$\left(\frac{S}{N}\right)^2_{z\approx z'} = f_{sky} \sum_{\ell_{min}}^{\ell_{max}} (2\ell+1) \int_z dz' \frac{|C_\ell^{\tau 21}(z')|^2}{(C_\ell^{\tau\tau} + N_\ell^{\tau\tau})(C_\ell^{2121}(z') + N_\ell^{2121}(z'))} , \tag{3.28}$$

CMB Experiment	Sensitivity Δ_T [μK arcminute]	θ_f [arcminute]
CMB-S4	1	1
PICO	0.6	2
Simons Observatory	3	2

Table 3.1: Configurations of CMB experiments considered in our analysis (see text).

21cm Experiment	A_{eff} [m^2]	t_{int} [hours]	$\Delta\nu$ [Mhz]
HERA 350	53878	1080	0.1
SKA	41659	1080	0.2

Table 3.2: Configurations of 21cm observatories considered in our analysis (see text).

at the redshift z' where the $C_\ell^{\tau-21}$ is probed, that is determined by the observational frequency of the 21cm experiment.

The detectability of the $\tau - 21$ power spectrum is investigated for the experiments listed in Table 1 (CMB) and Table 2 (radio arrays). All the following plots refer to redshift $z \sim 7$ and the reference combination of CMB-S4 plus SKA experiments.

In Figure 3.4, we show the detectability of the cross-correlation signal as a function of the observed sky fraction. While future CMB experiments will observe more than 40% of the sky, 21cm observations will be limited to a smaller portion of it ($\approx 1-10\%$). The SNR of the cross-correlation increases as $\sqrt{f_{sky}}$ in terms of the common sky fraction, so it is limited by the 21cm observations and amounts to SNR $\sim 5.5 - 24.6$ for $f_{sky} \sim 1\% - 20\%$. Even with a sky fraction of a few percents, the global cross-correlation signal is detectable at more than 5σ; for sky fractions larger than 10% it will be possible to pick up the signal in the multipole range around the minimum of the cross-correlation at more than 3σ.

In Figure 3.5 and 3.6 we illustrate how the detectability of the $\tau - 21$ cross-correlation depends on the parameters describing the reionization morphology, i.e the mean bubble size $\bar{R}$ and the variance of its (Gaussian) distribution $\sigma_{\rm lnr}$. Figure 3.5 shows that the cumulative SNR is marginally affected by those parameters; e.g., the SNR changes by $\sim 3\%$ when $\bar{R}$ increases from 1 to 10 Mpc. However, the distribution of bubbles imprints clear signatures in the cross power spectrum $\ell(\ell+1)\, C_\ell^{\tau 21}$; as already mentioned, the position of the minimum occurs at a multipole corresponding to the average bubble size, and its extent scales proportionally to the width of the bubble distribution. From this point of view, precision measurements of the cross power spectrum can pose constraints to the morphology of the reionization history.

In Figure 3.7, we investigate how the detectability of the cross-correlation is affected by assuming different values of the spatially-averaged optical depth for electron scattering. Specifically, we vary τ in the range $0.047 - 0.054 - 0.061$ that brackets the 1σ constraints by the Planck experiment. The cross power spectrum and cumulative SNR are slightly modified for $\tau > 0.054$ while they drastically change for $\tau < 0.05$ since for such low values of the optical depth the reionization process is far from being completed at the redshift

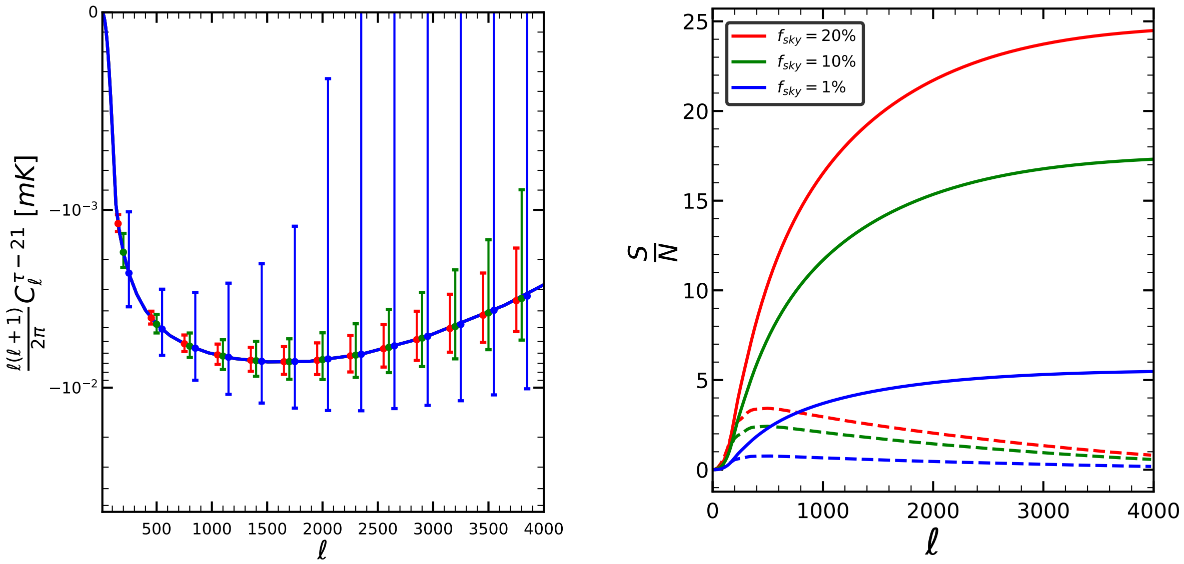

Figure 3.4: Dependence of the forecasted $C_\ell^{\tau-21}$ (left panel) and related SNR (right panel) on the observed sky fraction. In the right panel, solid lines refer to cumulative SNR while dashed lines to SNR in the binned spectra with $\Delta_\ell \approx 100$. The experiments considered here are CMB S4 and SKA.

$z \approx 7$ plotted here.

In Figure 9 we forecast the detectability of the $\tau - 21$ cross-correlation for a different combination of future CMB (CMB-S4, PICO, Simon Observatory) and 21cm experiments (HERA, SKA), whose features are listed in Table 1 and 2. The computed SNR is well above 5σ for almost all the combinations, with the best sensitivity achieved from PICO plus SKA.

21cm Experiment	S/N
CMB-S4 × SKA	17
CMB-S4 × HERA	4.5
PICO × SKA	19.5
PICO × HERA	5.9
SO × SKA	11.5
SO × HERA	3.8

Table 3.3: Forecasted cumulative SNR of the $\tau - 21$ cross correlation by combining different CMB and 21cm experiments.

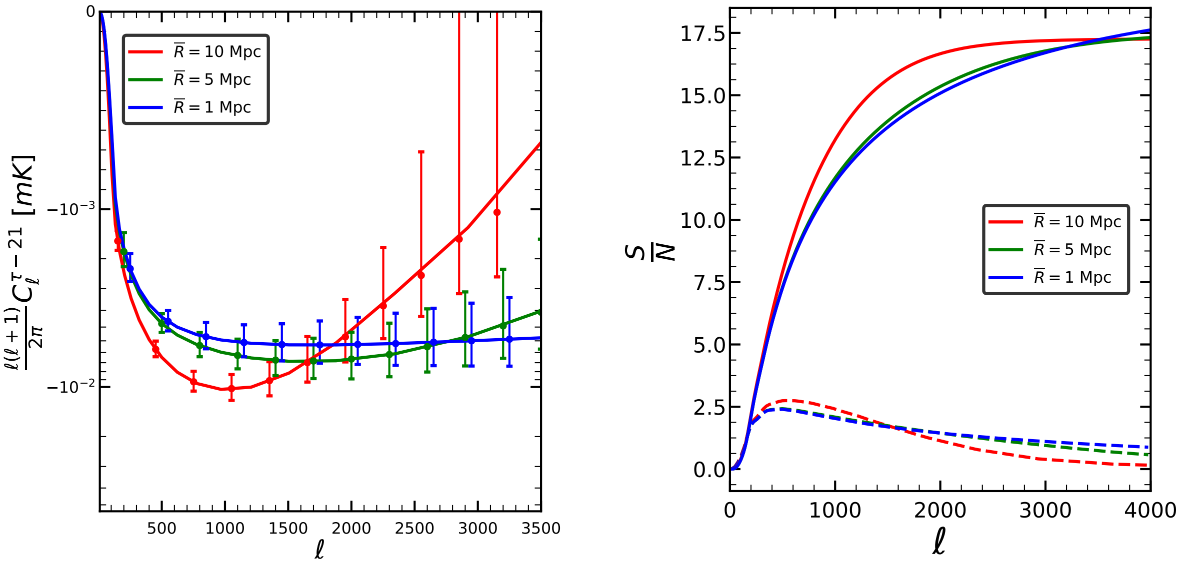

Figure 3.5: Same as previous figure for the average bubble size.

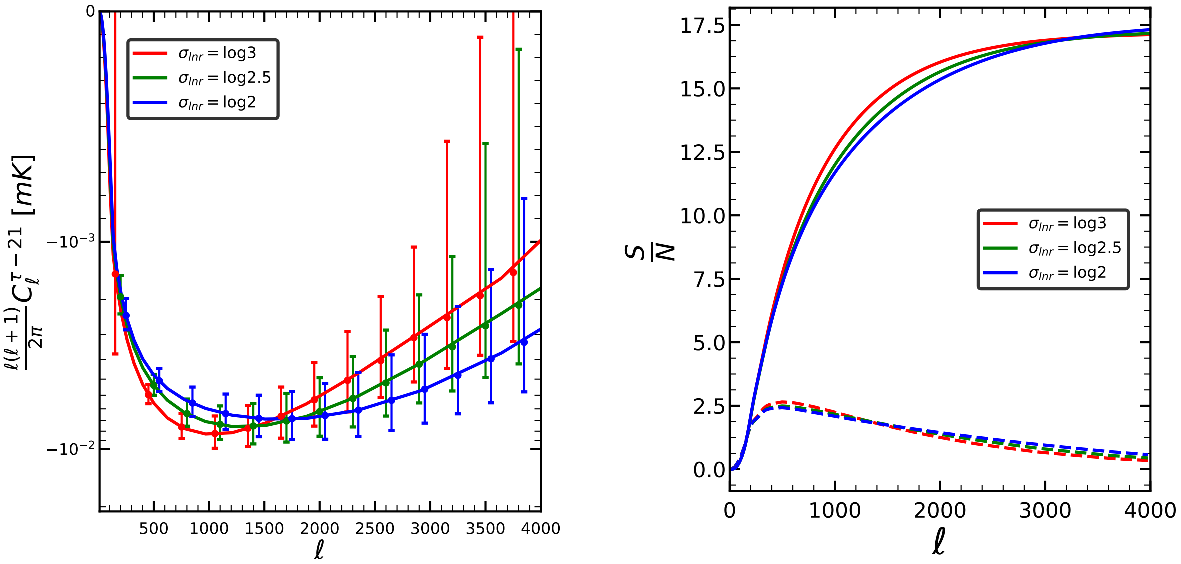

Figure 3.6: Same as previous figure for the dispersion of the bubble size distribution.

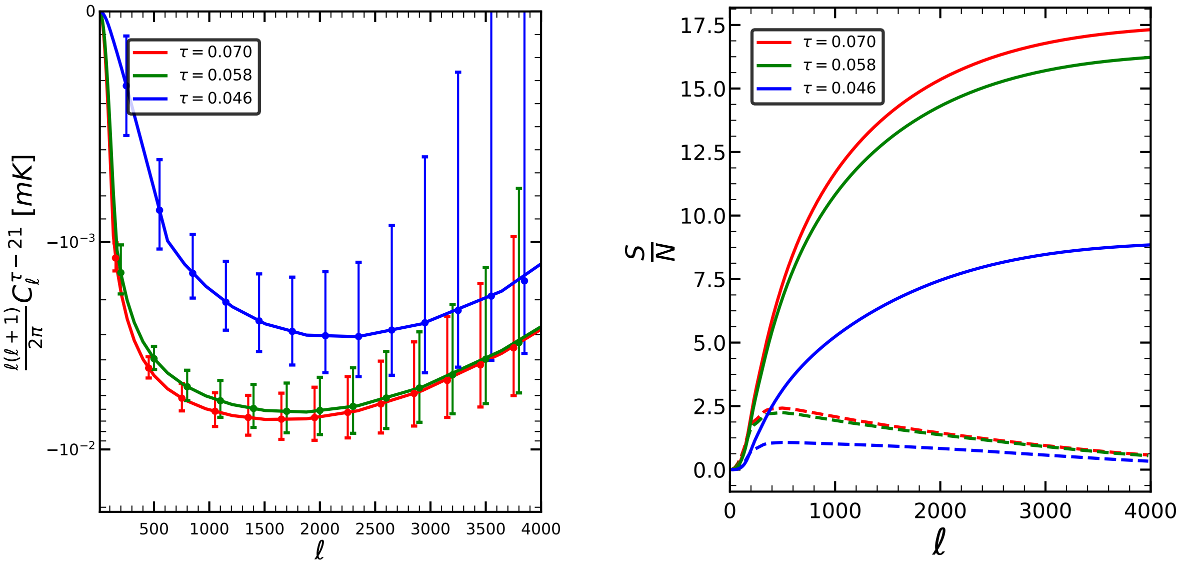

Figure 3.7: Same as previous figure for the spatially-averaged optical depth τ.

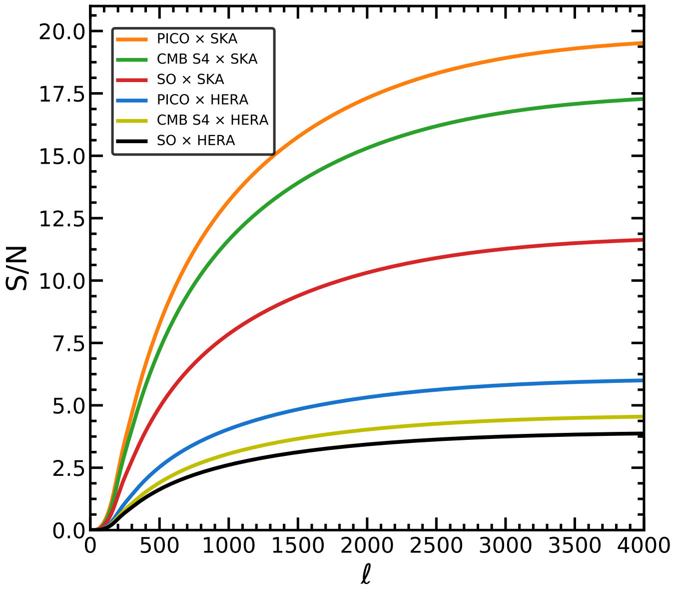

Figure 3.8: Forecasted cumulative SNR of the $\tau - 21$ cross correlation by combining different CMB and 21cm experiments, listed in Tables 3.1 and 3.2.

3.5 Cross correlation between tSZ and τ field

The tSZ effect depends on the light of sight integral of the pressure profile. The Compton y parameter for the tSZ can be written as

$$y = \frac{\sigma_T}{m_e c^2} \int k_B T_e n_e d\ell \,, \tag{3.29}$$

T_e and n_e are the temperature of electron gas and electron number density.

The tSZ effect will have contributions both from reionization (early time) and clusters (late time). Gas inside the Ionized bubbles can be parameterized by temperature T_e, density n_e and pressure p_e. We rewrite the equation 3.29 only considering the reionization contribution into the Compton y parameter as,

$$y = \frac{c\sigma_T}{m_e c^2} \int \frac{dz}{H(z)(1+z)} k_B T_e(z) n_e(z) \,. \tag{3.30}$$

We have $n_e(z) = n_{p0}(1+z)^3 x_e(z)$, and $x_e(z) = n_e/n_H$ is the ionization fraction at the redshift z and n_{p0} is the present number density of protons. We replace $n_e(z)$ in the above equation by x_e,

$$y = \frac{c\sigma_T}{m_e c^2} \int \frac{dz}{H(z)} (1+z)^2 n_{p0} k_B x_e(z) T_e(z) \,. \tag{3.31}$$

From Equations (3.29) and (3.31), we can calculate the pressure as

$$P_e(z) = k_B n_{p0} (1+z)^3 x_e(z) T_e(z) \; ev/k \,. \tag{3.32}$$

Our goal is to estimate the temperature fluctuations in CMB by tSZ effect for the patchy reionization only. Rather than calculating pressure profile, we have calculated $\eta_e(z) = x_e(z)T_e(z)$ in each redshift. Hence, we can write y in spherical harmonics space as:

$$y_{\ell m} = 4\pi(-i)^\ell \int \frac{d^3k}{(2\pi)^3} \eta_e(k) \alpha_\ell(z) \,, \tag{3.33}$$

In the above equation, we have

$$\alpha_\ell(z) = \frac{\sigma_T K_B n_{p0} c}{m_e c^2} \int \frac{(1+z)^2}{H(z)} dz \,. \tag{3.34}$$

We can construct the expression for the angular auto power spectra of the y parameter as

$$< y_{\ell m} y^*_{\ell' m'} >= \delta_{\ell m} \delta_{\ell' m'} C_\ell^{yy} \,, \tag{3.35}$$

$$C_\ell^{yy} = \int \frac{dk}{k} \Delta^2_{\eta\eta}(k) \alpha_\ell(k)^2 \,. \tag{3.36}$$

Here $\Delta^2_{yy}(k) = k^3 P_{\eta\eta}(k)/2\pi^2$, which leads to

$$C_\ell^{yy} = \frac{\sigma_T^2 K_B^2 n_{p0}^2}{m^2 c^4} \int \frac{d\chi}{a^4 \chi^4} P_{\eta\eta} \,. \tag{3.37}$$

In a similar way, we can decompose the τ field in spherical harmonics and write

$$\tau_{\ell m} = 4\pi(-i)^{\ell} \int \frac{d^3k}{(2\pi)^3} \eta_e(k)\beta_\ell(z)\,, \tag{3.38}$$

where,

$$\beta_\ell(z) = \sigma_T n_{p0} \int \frac{(1+z)^2}{H(z)} dz\,. \tag{3.39}$$

Now we can calculate the $\tau - y$ angular spectra using the equation (3.33) and (3.38) which is

$$C_\ell^{\tau y} = \frac{K_B \sigma_T^2 n_{p0}^2}{mc^2} \int \frac{d\chi}{a^4\chi^2} P_{\eta\eta}. \tag{3.40}$$

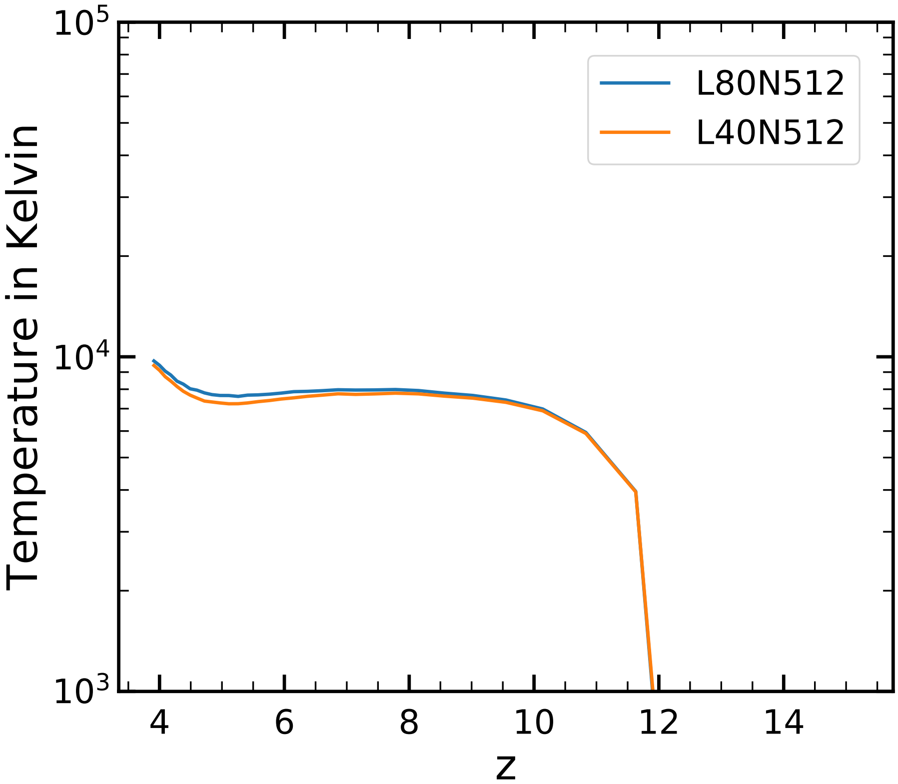

Figure 3.9: Plot for the T_e evolution for the L80N512 and L40N512 Radiative transfer simulations.

We calculated n_e, T_e and P_e in boxes with side 40 cMpc/h (labeled as L40N512) and 80 cMpc/h (L80N512) using radiative transfer simulation of reionization. We describe the simulations of reionization in Chapter 4. In this Section we will discuss the $\tau - y$ signal from patchy reionization.

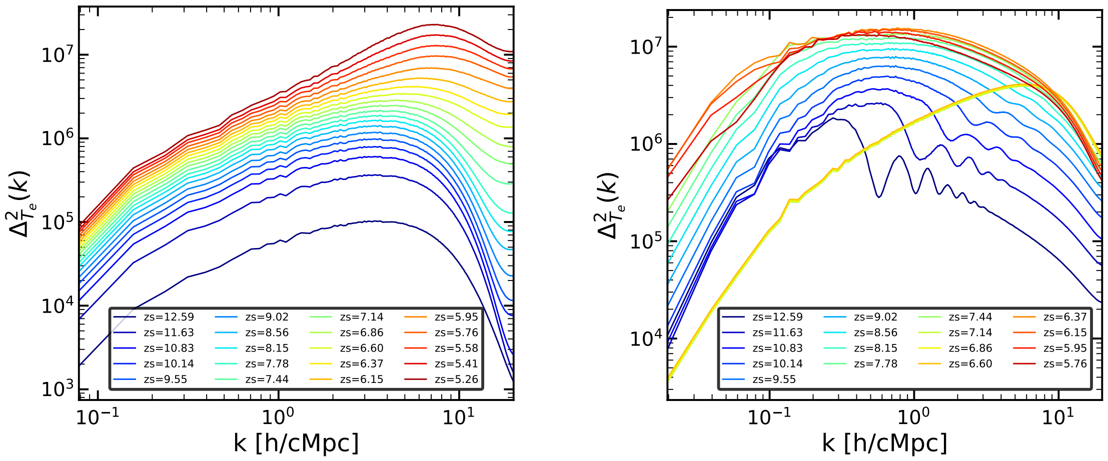

Figure 3.10: This plot shows the temperature power spectra in different redshifts for the L80N512 (left) and L320N2048 (right) radiative transfer simulations. This and the plots in this Section have not appeared in paper yet, and was done for the writing of this Thesis

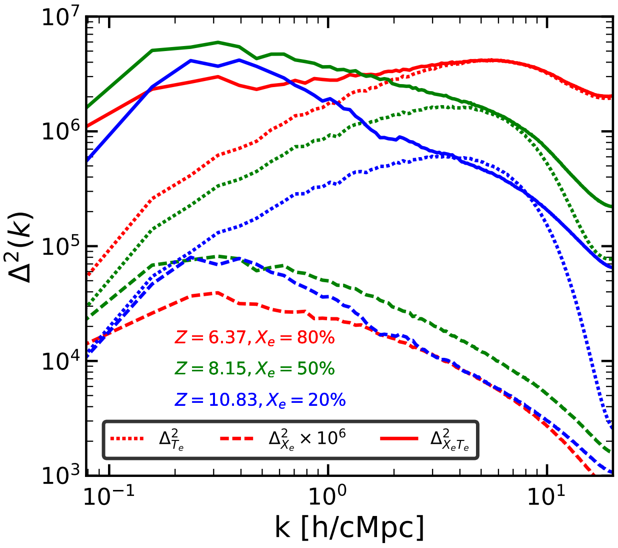

Figure 3.11: T_e, x_e and x_eT_e power spectra for the redshifts correspondiong to reionization is at the 20%, 50% and 80% level of completion.

Figure 3.9 shows the temperature evolution of the IGM in different redshifts. We show the temperature power spectra for L80N512 and L320N2048 in Figure 3.10. As the average temperature of the IGM increases with the ionization fraction (x_e) $\Delta^2_{T_e}$ also increases. For the L320N2048 simulation, reionization is driven by massive haloes; hence, the peak of the $\Delta^2_{T_e}$ shifts towards smaller k (large scale).

We compare power spectra of different thermodynamic quantities such as T_e, x_e and their product in Figure 3.11. When the Universe is neutral, the amplitude of x_e power

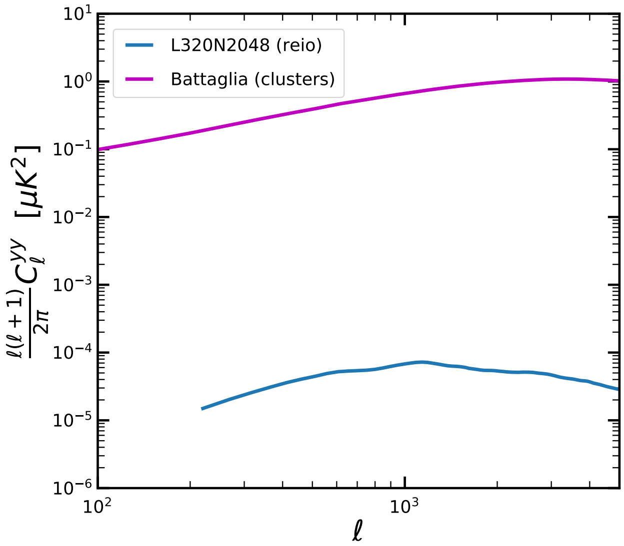

Figure 3.12: We showed tSZ power spectra due to the patchy reionization only for 80–512 and 320–2048 simulations. We compared it with the tsz power spectra for the galaxy clusters (Battaglia et al. 2012).

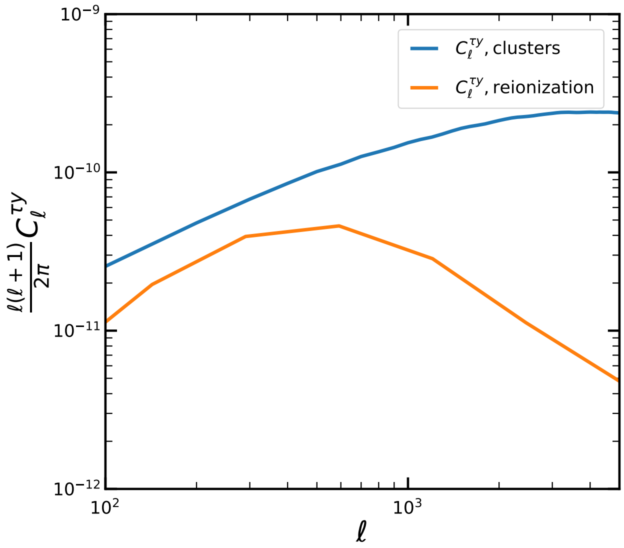

Figure 3.13: $\tau - y$ power spectra due to the patchy reionization.

spectra is very small, and it reaches its maximum value when the Universe is almost 50% ionized; after that, it again falls as Universe becomes almost ionized. x_eT_e is modulated by the x_e power spectra on a large scale and by the temperature power spectra on the small scales. The pressure P_e will have the same shape but different amplitude. We finally calculate the $y - y$ signal from reionization using the $\eta = n_eT_e$ template calculated from the radiative transfer simulations of patchy reionization. tSZ due to patchy reionization is a second-order effect in the CMB. We compare it with the tSZ profile for clusters determined by [203], and we find that the tSZ from reionization is more than three orders of magnitude lower than the tSZ signal from galaxy clusters. It is practically impossible to detect the tSZ signal coming from the reionization.

We show the $\tau - y$ cross-correlated signal in Figure 3.13 and we compare it with the τy signal due to the clusters. We will consider it as future work to explore the detectability of the τy signal. The main problem is that the primary CMB anisotropies are much larger than this signal and also we need to take into account the residual foreground contamination; these two things can make lower the signal to noise significantly.

3.6 Summary and Outlook

We have investigated the future detectability of the cross-correlation between fluctuations in the electron scattering optical depth τ as probed by CMB experiments, and fluctuations in the 21-cm brightness temperature, as probed by ground-based radio interferometers.

Future measurements of the $\tau - 21$cm cross-correlation will probe the evolution of the morphology of the cosmic reionization process, thus, shedding light on the properties of the primeval astrophysical sources, and the distribution of ionized and neutral matter. The $\tau - 21$cm cross-correlation features an inverse bell shape with a minimum at around the multipoles corresponding to the projection on the sky of the average size of the ionizing bubbles, and a width resulting from the bubble size distribution. The depth of the minimum is maximal at the redshift where the ionizing fraction is around 50% and then becomes shallower at lower and at higher redshift. The cross power spectrum vanishes in a completely neutral or completely ionized Universe.

We have computed the cumulative SNR expected for the $\tau - 21$cm cross-correlation by combining future CMB experiments probing τ (specifically, CMB-S4, PICO and Simons Observatory) with ground-based radio-arrays probing 21cm brightness temperature (specifically, HERA and SKA). We have obtained cumulative SNR larger than 5 for most of the cross configurations, with an optimal SNR around 20 from PICO and SKA. The detectability of the cross-spectrum is weakly dependent on the parameter specifying the reionization morphology (the bubble size distribution), and on the spatially- averaged value of τ (at least for $\tau > 0.05$). On the other hand, the SNR is strongly sensitive to the sky fraction f_{sky} commonly covered by CMB and 21cm experiments; for $f_{sky} \sim 1 - 20\%$, the cumulative SNR increases from values around 5 to about 25. The detailed shape around the minimum can be probed with significances greater than 3σ only when f_{sky} exceed 10%.

As we will outline in the final Chapter, future developments of this work concern: (i) detailed modeling of the foregrounds affecting the 21cm observations; (ii) using state-of-the-art numerical simulations to describe the reionization morphology in place of our simple analytic bubble size distribution; and (iii) MCMC analysis to quantitatively address the potential of $\tau - 21$cm cross-correlation in reconstructing the parameters describing the astrophysics of primeval ionizing sources and the reionization morphology.

Chapter 4

Revised estimates of reionization-induced B modes

> Look up at the stars and not down at
> your feet. Try to make sense of what
> you see, and wonder about what
> makes the Universe exist. Be curious.
>
> *Stephen Hawking*

4.1 Introduction

As we mentioned in Chapter 1, an important goal for the next-generation CMB experiments is the detection of B-mode polarization of the CMB induced by primordial gravitational waves [37]. We stress again how many such experiments are currently underway, such as the BICEP Array [204], SPT-3G [205], Simons Observatory [85], or proposed such as CMB-S4 [206], LiteBIRD [207], PICO [52], and CMB-Bharat [51]. These experiments hope to build on the successes of past experiments, such as Planck [87], ACT [208], SPT [209], BICEP2/Keck [210] either to detect or significantly reduce the upper limit on the tensor-to-scale ratio parameter r by one or two orders of magnitude from the current $r < 0.06$ (95% confidence) [98]. A particularly compelling threshold is $r \gtrsim 10^{-3}$ in single-field slow-roll inflation [54]. It was shown in Ref. [54] only two classes of single-field inflation models are consistent with current measurements of the primordial power spectrum. On of the two classes has a characteristic scale over which the potential driving inflation varies. $r \lesssim 10^{-3}$ presents a threshold which excludes all models in this class with a characteristic scale that exceeds the Planck scale [54]. Detection of primordial B modes at this level will thus constitute an exciting test of the single-field slow-roll paradigm, while also pushing cosmological constraints to higher energy scales and closer to the Big Bang.

As we stressed in Chapter 1, in order to succeed, these experiments will have to confront foreground B-mode polarization. The dominant part of these foregrounds is created by polarised diffuse synchrotron emission and polarised dust emission from the Galaxy [211], which can be handled by means of avoidance and/or removal strategies [212, 211, 213]. Foregrounds, with respect to the primary signal from inflation, also consist of secondary B-mode polarization anisotropies that can potentially have a significantly larger amplitude than primordial B modes. These include secondary B modes induced by gravitational lensing [214, 46], the thermal and kinetic Sunyaev-Zel'dovich effect [215, 216], and by fluctuations in the Thomson scattering opacity of the Universe during the epoch of reionization [217, 218, 183, 127, 178]. Lensing-induced B modes have now been detected by several experiments [209, 219, 220, 221, 97, 99]. While this signal can dominate over the primordial B modes for small values of r, it is possible to disentangle the two B modes by using lensing deconstruction algorithms that exploit higher-order temperature-polarization correlations introduced by lensing to delens the polarization map [222, 223, 224]. Compared to the lensing-induced B modes, the B modes created due to patchy reionization are more difficult to disentangle from the primordial signal. This is mainly because of the uncertainty in the amplitude of the reionization-induced B modes.

A further complication is that the level of reionization-induced B-mode anisotropy also depends on the morphology of the ionized regions created during reionization. As we explained in Chapter 2, reionization is thought to occur due to the formation and eventual overlap of ionized regions around sources of hydrogen-ionizing radiation such as galaxies or quasars. The size and evolution of these ionized regions depend on the mass and brightness of these sources. However, what these sources remain unclear. Bright quasars are efficient sources of hydrogen-ionizing radiation, but their abundance at high redshifts is probably too low [225]. Galaxies are known to exist at redshifts as high as $z \sim 11$ but it is unclear if hydrogen-ionizing photons produced by young stars within these galaxies can escape into the intergalactic medium without being absorbed by the in situ hydrogen [e.g., 226, 227, 228, 229]. For a given reionization history, reionization by quasars instead of galaxies can result in a larger amplitude of the induced secondary B modes due to the enhanced clustering of quasars [230]. Similar changes in the B-mode anisotropy amplitude can occur due to different relative contribution of bright and faint galaxies to reionization. Brighter galaxies typically reside in highly-clustered massive haloes, which can increase the anisotropy amplitude on certain scales.

Given these uncertainties, a reliable estimate of reionization-induced B modes are of obvious interest to next-generation CMB experiments. We consider this issue in this Chapter. It has traditionally been difficult to get tight constraints on the redshift of reionization because the pre-eminent probe of the high-redshift intergalactic medium, the Lyman-α Forest, saturates already when the neutral hydrogen fraction is $\sim 10^{-4}$. In recent years, however, excellent constraints on the redshift at which reionization ended have come from a somewhat unexpected direction. It has been noted that the Lyman-α forest at $z \sim 5.5$ exhibits spatial fluctuations that are significantly larger than those expected due to density inhomogeneities in a post-reionization Universe [112, 231, 232, 233, 234]. Recently, it was shown that these fluctuations are a signature of the last stages of reionization [235]. In this picture, large patches (of sizes of up to 100 comoving Mpc) neutral hydrogen exist in low-density regions of the Universe at $z \sim 5.5$. It is these “neutral islands” that cause the observed spatial scatter in the Lyman-α forest. This interpretation yields a rather tight constraint on the redshift of the end of reionization of $z = 5.2$. The reionization history at higher redshifts is less well-constrained. However, some constraints do result due to radiative transfer from these redshifts down to redshifts at which observations exist. This results in a redshift for the mid-point of reionization at $z = 7$. In this Chapter, we draw implication of these new constraints for the CMB B-mode signal.

We use hydrodynamic cosmological simulations post-processed for radiative transfer. These simulations have a large dynamic range (from ~ 100 comoving kpc to 160 comoving Mpc) that allows us to model the effect of small-scale reionization sources while deriving the large-scale CMB signal. They are carefully calibrated to reproduce the Lyman-α forest data, including the spatial fluctuations in the Lyman-α forest opacity. In the process, these simulations also yield a value of the Thomson scattering optical depth to the last scattering surface that is remarkably close to the measured value reported by Planck 2018 [13]. We extrapolate these simulations to even larger length scales (1 cGpc) by using the excursion set method of modelling ionized regions in the epoch of reionization (EoR)[180]. After presenting predictions for the B-mode signal in our fiducial reionization model, we also consider the effect on this signal of the uncertainty in the first half of the reionization history and the uncertainty regarding the masse of reionizing sources. Finally, we consider the range of values of the tensor-to-scalar ratio, r that can be reliably probed by various upcoming CMB experiments in the presence of the secondary B modes from reionization. Throughout this work, we assume $\Omega_\mathrm{b} = 0.0482$, $\Omega_\mathrm{m} = 0.308$, $\Omega_\Lambda = 0.692$, $h = 0.678$, $n_\mathrm{s} = 0.961$, $\sigma_8 = 0.829$, and $Y_\mathrm{He} = 0.24$ [236]. The units 'ckpc' and 'cMpc' refer to comoving kpc and comoving Mpc, respectively.

This Chapter is organized as follows. In Chapter 4.2, we review mechanisms behind the B-mode signal due to patchy reionization. We discuss the radiative transfer simulation of reionization in Chapter 4.3. We also describe the method of having ionization field at large scales in this Chapter. We discuss our results in Chapter 4.4.

4.2 Secondary B-mode anisotropies from reionization

After decoupling at $z \sim 1100$, baryons evolve in a predominantly neutral universe. Eventually, the first bound objects will appear in the form of proto-stars around $z \sim 50$ [237]. The photons produced by these objects reionize the Universe by $z \sim 5$ [117, 235, 13]. Because of the matter field is inhomogeneous, different parts of the Universe will reionize at different moments in time; this results in patchy reionization, where the optical depth τ, as measured to the last scattering surface is a function of position on the sky, i.e. $\tau(\hat{\mathbf{n}}, \chi)$. Patchy reionization will produce secondary fluctuations in the anisotropies of the CMB polarization through (a); scattering of free electrons of the local CMB quadruple during reionization and (b); screening of the CMB photons due to a finite optical depth. While both effects are present without patchiness, in the absence of fluctuations in the free electron density, B modes will not be generated. Patchy reionization will thus produce a unique signal in the B-mode polarization pattern of the CMB. Thomson scattering of free electrons mixes the CMB photons coming from different line of sights while screening acts along the same line of sight [178, 178, 107].

The free electron density generated at the time of reionization varies along different line of sight. The ionization fraction, x_e at comoving distance χ can be expressed as,

$$x_e(\hat{\mathbf{n}}, \chi) = \bar{x}_e(\chi) + \Delta x_e(\hat{\mathbf{n}}, \chi), \tag{4.1}$$

where $\Delta x_e(\hat{\mathbf{n}}, \chi)$ is the fluctuations in x_e along direction $\hat{\mathbf{n}}$ at conformal distance χ. The optical depth measures the line of sight integral of x_e and therefore also becomes a direction dependent quantity in the sky. We write

$$\tau(\hat{\mathbf{n}}, \chi) = c\sigma_T n_{p0} \int_0^{\chi} \frac{d\chi}{a^2} \left[\bar{x}_e(\chi) + \Delta x_e(\hat{\mathbf{n}}, \chi)\right], \tag{4.2}$$

where, c is the speed of light in free space, σ_T is Thomson scattering cross section, 6.652×10^{-29} m^2, n_{p0} is the present number density of protons and a is the scale factor. We can then derive a τ power spectrum. In the Limber approximation (valid for $\ell \gtrsim 20$) [238, 239, 240]

$$C_\ell^{\tau\tau} = \sigma_T^2 n_{p0}^2 \int \frac{d\chi}{a^4 \chi^2} P_{x_e x_e}\left(\chi, k = \frac{\ell}{\chi}\right). \tag{4.3}$$

Here, $P_{x_e x_e}$ is the 3D power spectrum of x_e which satisfies, $\langle \Delta x_e(\boldsymbol{k}) \Delta x_e(\boldsymbol{k}') \rangle = (2\pi)^3 \delta^{(3)}(\boldsymbol{k} + \boldsymbol{k}') P_{x_e x_e}(k)$. All the astrophysical aspects of reionization are encoded inside $P_{x_e x_e}$. We note that $C_\ell^{\tau\tau}$ is not directly observable. The τ power spectrum can be thought of as analogous to the lensing potential power spectra, $C_\ell^{\phi\phi}$ [127, 182]. When measured from the CMB, we aim to extract information that renders the primary CMB non-Gaussian. These effects can then be used to reconstruct the τ fluctuations [107, 127, 182].

4.2.1 B-mode signal due to scattering of CMB photons

To calculate the B-mode signal from reionization we need to account for the scattering probability of photons, fluctuations in the free electron density along the line of sight, and the rms value of the quadruple. As the local quadruple has a relatively large correlation length, for simplicity, we can consider a constant Q_{rms} during the EoR. The B modes signal due to the scattering can be expressed as [183]

$$C_\ell^{\text{BB(sca)}} = \frac{3}{100} \int \left[\frac{g(\chi)}{x_e(\chi)}\right]^2 Q_{\text{rms}}^2(\chi) P_{x_e x_e}(k, \chi) d\chi, \tag{4.4}$$

where $g(\chi)$ is the probability of a CMB photon to be scattered by a free electron at angular diameter distance χ. This probability is given by

$$g(\chi) = \dot{\tau} e^{-\tau(\chi)} = \frac{\sigma_T n_{p,0}}{a^2 \chi} x_e(\chi) e^{-\tau(\chi)}. \tag{4.5}$$

Combining the above equations we find

$$C_\ell^{\mathrm{BB(sca)}} = \frac{3\sigma_T^2 n_p^2}{100} \int_{\chi_s}^{\chi_e} \frac{d\chi}{a^4\chi^2} Q_{\mathrm{rms}}^2(\chi) P_{x_e x_e}(k,\chi) e^{-2\tau(\chi)}, \tag{4.6}$$

where χ_s and χ_e are the comoving distance at the start and end of reionization respectively. For the calculation of $C_\ell^{\mathrm{BB(sca)}}$ we will use $Q_{\mathrm{rms}} = 22\ \mu\mathrm{K}$ [127, 183].

4.2.2 B-mode signal due to the screening of CMB photons

Free electrons during the epoch of reionization act as an opaque medium between us and the last scattering surface. The primary anisotropies in the CMB after recombination are screened by an overall factor of $e^{-\tau}$ as

$$T(\hat{\mathbf{n}}) = e^{-\tau(\hat{\mathbf{n}},\chi)} T_p, \tag{4.7}$$

$$(Q \pm iU)(\hat{\mathbf{n}}) = e^{-\tau(\hat{\mathbf{n}},\chi)} (Q \pm iU)_p(\hat{\mathbf{n}}). \tag{4.8}$$

Here, T_p and $(Q \pm iU)_p$ are the primordial (denoted by the superscript p) fluctuation in temperature and polarization fields, respectively. The primordial E modes are screened and modulated by the shape of optical depth power spectrum $C_\ell^{\tau\tau}$. The morphology of reionization affects the shape and amplitude of $C_\ell^{\tau\tau}$ and hence also modulates $C_\ell^{\mathrm{BB(scr)}}$ spectrum accordingly. The B-mode signal due to the screening of electrons at EoR can be expressed as [178]

$$C_\ell^{\mathrm{BB(scr)}} = e^{-\bar{\tau}} \int \frac{d^2\boldsymbol{\ell}_1}{(2\pi^2)} C_{\ell_1}^{EE(p)} C_{\ell_2}^{\tau\tau} \sin^2(2\phi_\ell), \tag{4.9}$$

where $\bar{\tau}$ is the line-of-sight optical depth averaged over the full sky, $C_{\ell_1}^{EE(p)}$ is the primordial E-mode power spectrum, and ϕ_ℓ is the angle between $\boldsymbol{\ell}_1$ and $\boldsymbol{\ell}_2$. For convenience we choose the same axis to define both $\boldsymbol{\ell}$ and Q. In the above equation, $\boldsymbol{\ell} = \boldsymbol{\ell}_1 + \boldsymbol{\ell}_2$, so $\ell_2 = \sqrt{\ell_1^2 + \ell^2 - 2\ell_1\ell_2\cos\phi_\ell}$. Equation (4.9) can then be rewritten as:

$$C_\ell^{\mathrm{BB(scr)}} = e^{-2\tau} \int_{\ell_1^{\mathrm{min}}}^{\ell_1^{\mathrm{max}}} \frac{\ell_1 d\ell_1}{2\pi} \int_{\phi_\ell=0}^{\phi_\ell=2\pi} \frac{d\phi_\ell}{2\pi} C_{\ell_1}^{EE(p)} C_{\ell_2}^{\tau\tau} \sin^2(2\phi_\ell). \tag{4.10}$$

The B-mode power spectrum induced by patchy reionization is then given by the total sum

$$C_\ell^{\mathrm{BB(tot)}} = C_\ell^{\mathrm{BB(sca)}} + C_\ell^{\mathrm{BB(scr)}}. \tag{4.11}$$

4.3 Reionization model calibrated to Lyman-α forest data

As a realistic model for the anisotropic distribution of free electrons during the epoch of reionization, we consider the post-processed cosmological radiation hydrodynamical simulation presented by Kulkarni et al. [235] as our fiducial reionization model. The underlying cosmological hydrodynamical simulation is very similar in set-up to several simulations from the Sherwood Simulation Suite [241]. This simulation was performed using the P-GADGET-3 code, which is derived from the GADGET-2 code [242, 243]. The box size used is 160 cMpc/h. The dark matter and gas distributions are represented by 2048^3 particles each. The resultant dark matter particle mass is $M_{\rm dm} = 3.44 \times 10^7$ M$_\odot/h$ while the gas-particle mass is $M_{\rm gas} = 6.38 \times 10^6$ M$_\odot/h$. Periodic boundary conditions are imposed and the initial conditions are set at $z = 99$. These are identical to the initial conditions of the 160–2048 simulation from the Sherwood simulation suite [241]. These initial conditions are evolved down to $z = 4$. Snapshots of the gas density and other quantities are saved at 40 Myr intervals, which result in 38 snapshots. We simplify galaxy formation in this simulation by using the `QUICK_LYALPHA` option in P-GADGET-3 to speed up the simulation. This removes gas particles with temperature less than 10^5 K and overdensities of more than a thousand from the hydrodynamical calculation by converting them to star particles [244]. This approximation does not affect the reionization process as the mean free path of ionizing photons is determined by self-shielded regions with a typical overdensity of $\Delta = 10$–100 [245, 246]. Before post-processing the results of the hydrodynamic simulation, heat is injected in the gas distribution in the simulation box assuming instantaneous reionization at redshift $z = 15$ assuming ionization equilibrium with the metagalactic UV background modelled according to Haardt and Madau [247], marginally modified to result in inter-galactic medium (IGM) temperatures that agree with measurements [248]. Note that we do not use the ionization and temperature values that result out of this procedure; these values are instead provided by the radiative transfer calculation that is performed subsequently. The on-the-fly assumption of instantaneous reionization is made to simply ensure that the gas distribution at lower redshift has a realistic pressure smoothing, which plays a role while calibrating the simulation to Lyman-α data. An ideal approach would be to perform the radiative transfer itself on the fly, but this is still prohibitively expensive for the large dynamical ranges that we seek here. Fortunately, the absence of coupling between the radiative transfer and the hydrodynamic response to reionization heating is unlikely to affect the calibration of the simulation to the Lyman-α forest data [249] as the pressure smoothing scale at redshifts $z > 5$ for our chosen UV background is less than 100 ckpc/h [250, 251], approximately equal to the cell size of our grid (described below). The hydrogen ionization solver assumes radiative cooling via two-body processes such as collisional excitation of H I, He I, and He II, collisional ionization of H I, He I, and He II, recombination, and Bremsstrahlung [252], and inverse Compton cooling off the CMB [253]. Metal enrichment and its effect on cooling rates is ignored.

We post-process the simulation with the radiative transfer code ATON [254, 255]. In this approach, sources of ionizing radiation are assumed to be present at the location of dark matter haloes in the simulation. We identify dark matter haloes in the output snapshots using the friends-of-friends algorithm. At $z = 7$, the minimum halo mass in our simulation is $2.3 \times 10^8\ h^{-1}$M$_\odot$, which is close to the atomic hydrogen cooling limit. The maximum halo mass at this redshift is $3.1 \times 10^{12}\ h^{-1}M_\odot$. We assume that a halo with mass

M emits hydrogen-ionizing photons at a rate $\dot{N} = \alpha M$, where α is a free parameter that encodes our ignorance of the complex astrophysical processes, such as star formation and interaction with the interstellar medium, that govern the production of ionizing photons from galaxies. Note that the average ionizing photon emissivity of the simulated volume is then $\dot{n} = \alpha \sum M/V_{\mathrm{box}}$ where V_{box} is the volume of the simulation box and the summation is over all haloes. The parameter α is a function of redshift but is independent of halo mass. It is the only parameter that is varied in order to calibrate the simulation to given observations, such as the Lyman-α forest [235]. While performing the radiative transfer, we place sources only in haloes with masses greater than $10^9\,\mathrm{M}_\odot$ as the simulated halo mass function below this mass suffers from incompleteness due to lack of resolution. Further, as ATON solves the radiative transfer equation on a Cartesian grid, we project the smooth particle hydrodynamic (SPH) kernels of the gas particles in our simulation onto such a grid. We choose the number of grid cells equal to the number of gas particles in the simulation, which yields a grid resolution of 78.125 ckpc$/h$. The ATON code uses a moment-based description with the M1 approximation [254] for the Eddington tensor to solve the radiative transfer equation. In order to reduce the computational cost, we use a single photon frequency for the radiative transfer. We assume that all sources have a blackbody spectrum with $T = 70,000$ K [256]. This corresponds to an average photon energy of 23.83 eV in the optically thick limit. The reionization history and the calibration with the Lyman-α forest are both robust to variations in the assumptions regarding the source spectrum and photon frequency. A change in the source spectrum has the effect of changing the resultant temperature of the gas distribution in the simulation. However, any resultant deviations in the Lyman-α forest can be compensated by changing α in the source emissivity above.

The calibration of our simulation with Lyman-α data is demonstrated and discussed by [235]. Here we discuss the reionization history implied by this model. The left panel of Figure 4.1 shows the evolution of the volume-averaged free electron fraction $x_{\mathrm{e}} = n_{\mathrm{e}}/n_{\mathrm{H}}$ in our simulation compared with other models and data. In our model, hydrogen reionization completes rather late, at $z = 5.2$. The Universe is half ionized at $z_{\mathrm{re}} = 7$. We can quantify the duration of reionization Δz as the difference between the redshifts at which the Universe is 5% and 95% reionized. In our model, we have $\Delta z = 5.4$. As Figure 4.1 shows, this reionization history is more gradual than the tanh models considered in the Planck 2018 results [13]. While reionization in our simulations begins earlier compared to the best-fit tanh models from Planck 2018, reionization also ends somewhat later. This reionization history is consistent with recent constraints from the spectra of two highest-redshift quasars [257, 258] and the relatively model-independent constraints from the incidence of dark pixels in Lyα and Lyβ forests [259]. Note that as shown in Figure 4.1, we assume an instantaneous Helium reionization at $z = 2.7$ [260, 261].

The reionization history by [107](see their Section 2 for details) is derived by solving the standard ionization/recombination balance equation for the spatially-averaged ionization fraction, and exploits the cosmic SFR density by [119] based on the most recent determination of the dust-corrected UV, far-IR, and radio luminosity functions out to high redshift. In Figure 4.1 (right panel) we plot the reionization histories corresponding

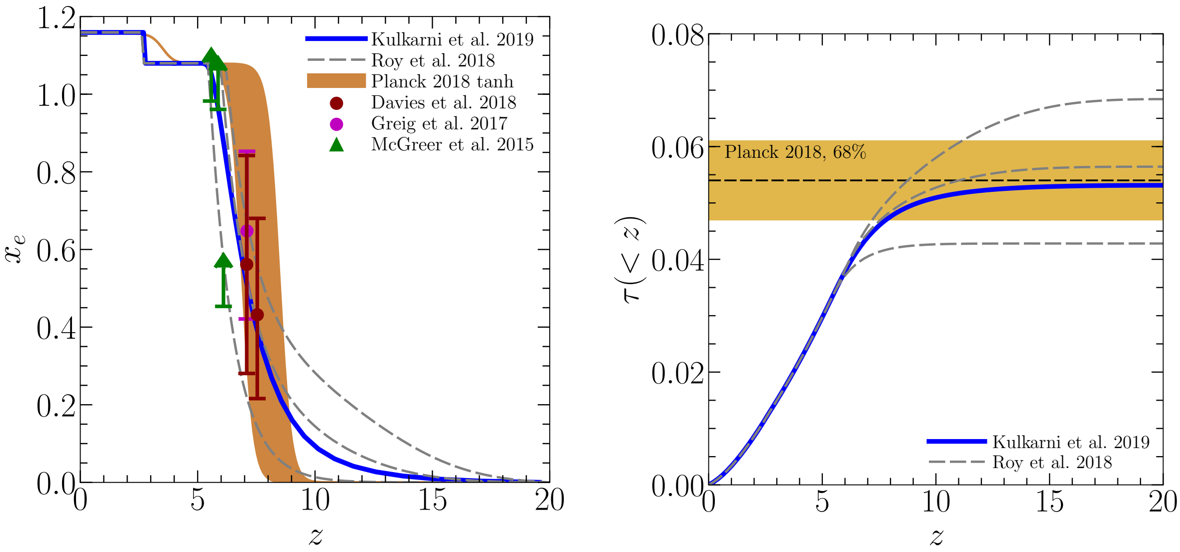

Figure 4.1: Left panel shows the free electron fraction evolution in from radiative transfer simulations of Kulkarni et al. [235] that we consider as our fiducial reionization model in this work. Also shown are constraints from the spectra of two highest-redshift quasars [257, 258] and from the incidence of dark pixels in Lyα and Lyβ forests [259]. The thin grey curves show reionization histories considered in previous work [107, 119]. The brown shaded region shows the 68% confidence region of the tanh reionization model reported in Planck 2018 [13]. The right panel shows the cumulative electron scattering optical depth in various reionization models, compared with the 2018 measurement from Planck [13] of $\tau = 0.054 \pm 0.007$ (68% confidence).

to a conservative value $f_{\rm esc} = 10\%$ of the escape fraction of ionizing photons from primeval galaxies, and to three different values $M_{\rm UV} = -17, -13, -12$ for the faintest UV magnitudes contributing to the ionizing background; in terms of integrated electron-scattering optical depth, the reionization history for $M_{\rm UV} \sim -13$ well reproduce the average Planck 2018 results while also being similar to the output of the detailed numerical simulation by [235].

Figure 4.1 also shows that the reionization history in our radiative transfer simulation is not very different from one of the models considered in previous work [107]. The key difference from that work is that the spatial distribution of the free electrons is now more realistic thanks to the use of the radiative transfer simulations. This has an effect on the derived power spectra, which we will discuss below. The right panel of Figure 4.1 shows the average cumulative Thomson scattering optical depth out to $z = 20$ in our simulation. It is found to agree very well with the 2018 measurement reported by Planck [13] of $\tau = 0.054 \pm 0.007$ (68% confidence).

The box size L determines the largest scale accessible in our reionization model. This corresponds to the fundamental mode of the box, which is given by $k_{\rm f} = 2\pi/L$. For the fiducial simulation described above the box size is 160 cMpc/h, which implies $k_{\rm f} = 0.039\,h$/cMpc. The value of $k_{\rm f}$ determines the minimum multipole, $\ell_{\rm min}$, we can reach in angular power spectra as we have $\ell \sim k/\chi(z)$. This allows us to go down to the $\ell_{\rm min} \sim 430$

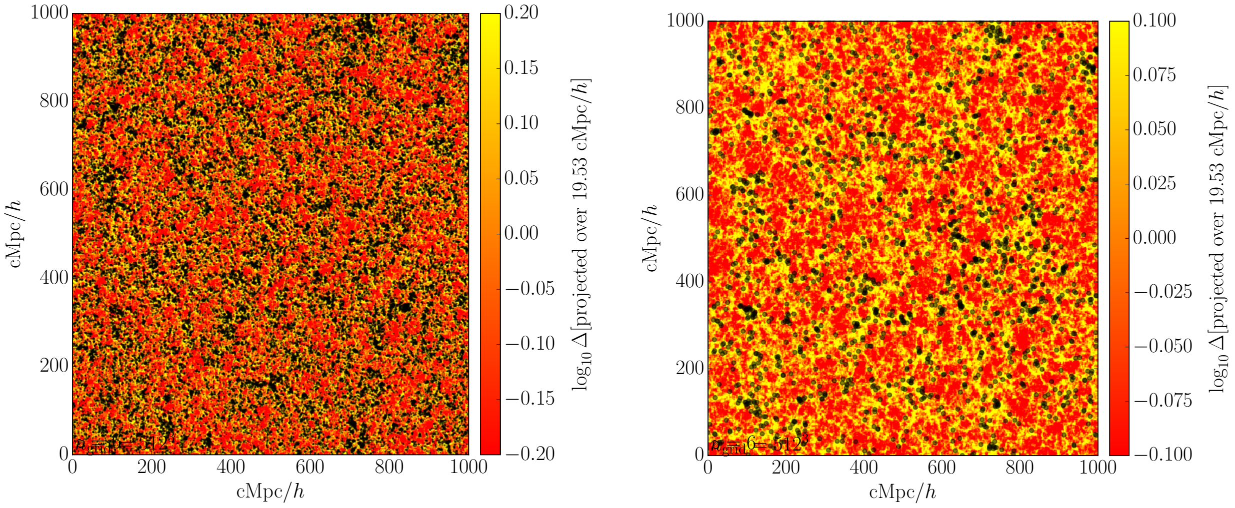

Figure 4.2: Left panel: We show the density slice of 1000 cMpc/h in length with the halos with different masses at $z \sim 7.15$. We only show the halos which has mass in between $10^{10}\ M_\odot$ to $2 \times 10^{10}\ M_\odot$. The yellow regions are the overdense and red regions are underdense compared to the mean density of the Universe. We can see that halos are formed on the overdense regions due to the gravitational collapse and underdense regions do not consist of any halos. Right panel: We show the same as left panel but the masses of halo fall in between $10^{11}\ M_\odot$ to $2 \times 10^{13}\ M_\odot$. It is expected that there will be more low mass halos than the high mass halos due to gravity and that is why there are more halos in the Left panel than the right one.

for 160 cMpc/h radiative transfer simulations. The power spectrum of the primordial B-mode signal peaks at $\ell \sim 100$. As a result, we need to extrapolate the B-mode power spectrum to spatial scales larger than the box size of our simulation. We do so next using a well-known semi-numerical method based on the excursion set approach of modelling reionization. We validate this method by comparing it with our radiative transfer results. Then, for the same reionization history, we use the semi-numerical method to model the ionization structure during the epoch of reionization to 1 Gpc scales, which corresponds to $\ell_{\rm min} \sim 50$, well above the scale at which the primordial signal is expected to peak.

We use the 21cmFAST code [262, 263] to generate the density field from redshift $z_{\rm start} = 19.5$ to $z_{\rm end} = 4.97$ at 40 Myr intervals. Gaussian initial conditions were set on a 3548^3 grid at $z \sim 300$. 21cmFast then calculates the linear velocity field on a coarser 512^3 grid using the Zel'dovich approximation [264, 265]. These velocities are then used to update the particle positions in the initial density field. This method of generating large-scale density fields using the Zel'dovich approximation is computationally efficient and has been validated by several works [e.g., 266, 267, 268, 263]. The coarse resolution of the grid is sufficient for our purposes as we are primarily interested in the large-scale distribution of ionized hydrogen. Next, we identify haloes with masses above $10^9\ \mathrm{M}_\odot$ using the Extended Press-Schechter formalism [269, 270]. 21cmFAST finds haloes iteratively in k-space by first smoothing the density field at a certain scale and identifying locations of haloes as points where the overdensity for the gravitational collapse, $\delta_c = 1.686/D(z)$,

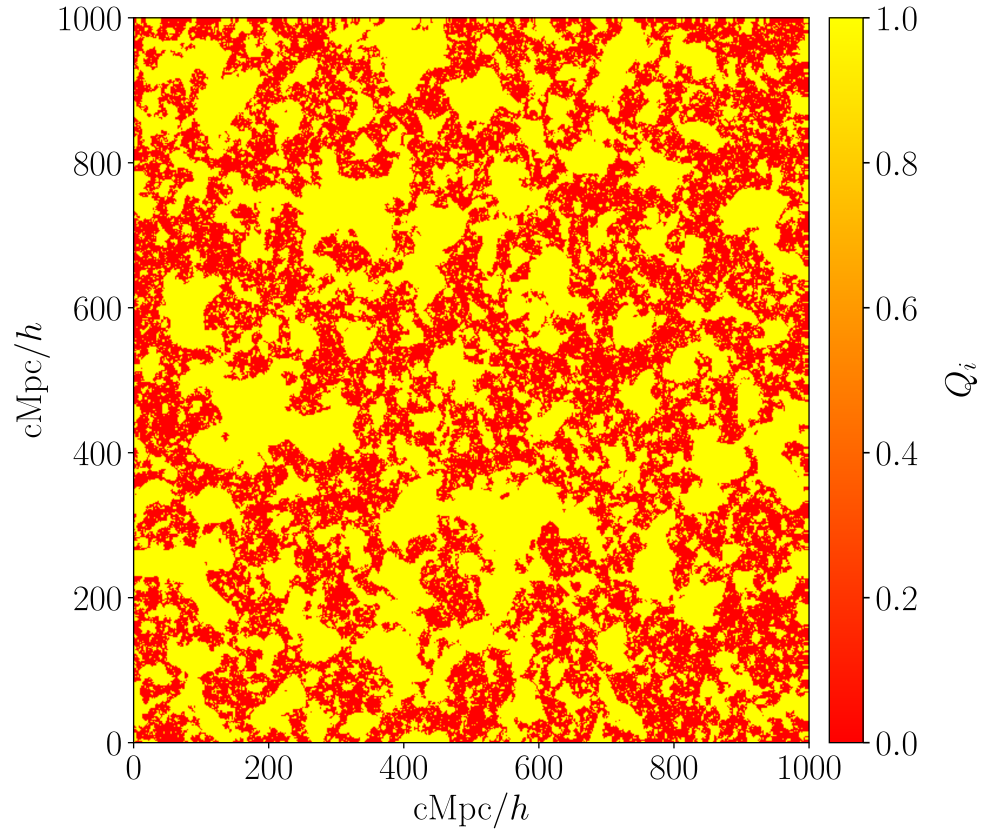

Figure 4.3: We show the ionization slice of 1000 cMpc/h in length. Universe is ionized if $Q_i \sim 1$ and neutral if $Q_i \sim 0$. In this slice, yellow regions are ionized and red regions are neutral. If we compare this slice with Figure 4.2, we see that regions become ionized in the same location where halos are populated. It is because halos act as ionizing sources and which ionized the surrounding regions.

where $D(z)$ is the growth factor. A real space top-hat filter is used for smoothing the density field and assigning masses to the haloes.

Given the density field and halos, we derive the ionization field by placing sources of Lyman-continuum radiation in dark matter haloes and using the well-known excursion set method [271, 272, 273]. Similar to our radiative transfer simulation above, the total number of ionizing photons N_γ produced by a halo is assumed to be proportional to the halo mass [274]

$$N_\gamma(M) = N_\gamma^{\rm LyC} M, \tag{4.12}$$

where the proportionality factor $N_\gamma^{\rm LyC}$ includes the Lyman-continuum escape fraction. A grid cell at position $\mathbf{x}$ is ionized if the condition

$$\langle n_\gamma(\mathbf{x})\rangle_R > \langle n_{\rm H}(\mathbf{x})\rangle_R(1+\bar{N}_{\rm rec}), \tag{4.13}$$

is satisfied in a spherical region centred on the cell for some radius R [275, 272, 273].

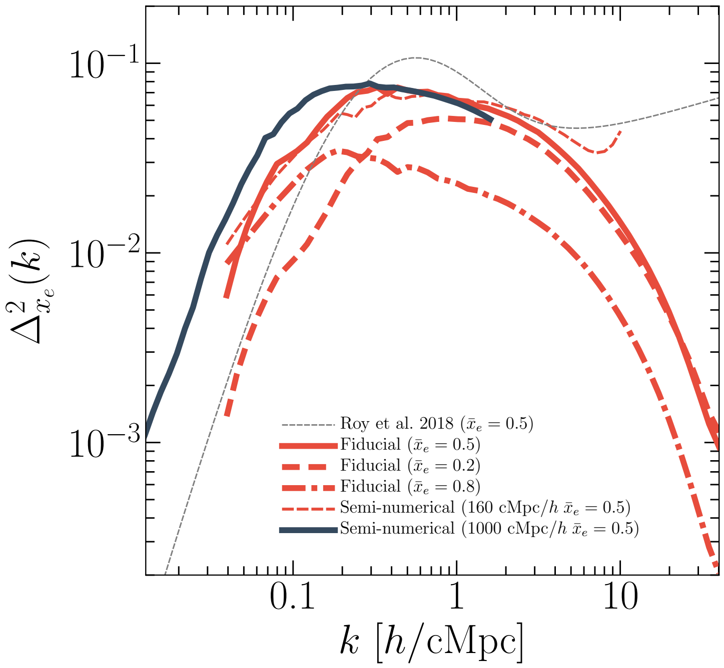

Figure 4.4: Thick solid, dashed, and dot-dashed curves show the power spectra of x_e for different mean ionization fractions from our fiducial radiative simulation. The thin dashed curve shows the same for $\bar{x}_e = 0.5$ from the semi-numerical method implemented on a 160-cMpc/h long box. The thick black curve shows the power spectrum from the semi-numerical method implemented on a 1 cGpc/h box.

Here, the averages are over the spherical region, $n_{\rm H}$ is the hydrogen number density,

$$n_\gamma = \int_{M_{\rm min}}^{\infty} dM \left.\frac{dN}{dM}\right|_R N_\gamma(M), \tag{4.14}$$

where $dN/dM|_R$ is the halo mass function within the spherical region, $M_{\rm min}$ is the minimum halo mass that contributes ionizing photons, and $\bar{N}_{\rm rec}$ is the average number of recombinations per hydrogen atom in the IGM. (Note that the global volume average of $n_{\rm H}$ is n_{p0}.) The condition in Equation (4.13) can be recast as

$$\zeta_{\rm eff} f(\mathbf{x}, R) \geq 1, \tag{4.15}$$

where the quantity

$$f = \rho_m(R)^{-1} \int_{M_{\rm min}}^{\infty} dM \left.\frac{dN}{dM}\right|_R M, \tag{4.16}$$

is the collapsed fraction into haloes of mass $M > M_{\rm min}$, $M_{\rm min}$ is the minimum mass of halos that emit Lyman continuum photons, $\rho_m(R)$ is the average matter density, and $dN/dM|_R$ is the halo mass function in the sphere of radius R. The parameter $\zeta_{\rm eff}$ quantifies the number of photons in the IGM per hydrogen atom in stars, accounting for hydrogen recombinations in the IGM. We can write $\zeta_{\rm eff}$ in terms of the parameters of Equations (4.12) and (4.13) as

$$\zeta_{\rm eff} = \frac{N_\gamma^{\rm LyC}}{1-Y_{\rm He}}(1+\bar{N}_{\rm rec})^{-1}, \tag{4.17}$$

where $Y_{\rm He}$ is the helium mass fraction. This is the only parameter that determines the ionization field in this approach. The volume-weighted ionized fraction in the simulation box is $Q_V \equiv \sum_i Q_i/n_{\rm cell}$, where the ionized volume fraction in a cell i is Q_i and $n_{\rm cell}$ is the total number of grid cells. Note that in this approach, $\zeta_{\rm eff}$ is the only parameter that sets the ionization fraction at a given time. We tune $\zeta_{\rm eff}$ to ensure that out 1 Gpc box has the same reionization history as the radiative transfer simulation described above.

We derive the spherically-averaged power spectrum of the electron fraction in our simulations as

$$P_{x_e x_e}(k) = \frac{\langle \widetilde{x}_e^2(k)\rangle}{V_{\rm box}}, \tag{4.18}$$

where $\widetilde{x}_e(k)$ is the Fourier transform of the electron fraction distribution in the box, $V_{\rm box}$ is the simulation box volume, and the averaging is done over the whole box.

Figure 4.4 shows the dimensionless power spectrum $\Delta^2(k) = k^3 P_{x_e x_e}/(2\pi^2)$ at three different redshifts in our fiducial radiative transfer box. The power spectrum peaks when the ionization fraction is close to 50%. In this figure, we also compare the power spectrum from our fiducial model with an implementation of the semi-numerical scheme in a box 160 cMpc/h on a side. This semi-numerical implementation is tuned to have an identical reionization history as our fiducial radiative transfer model by choosing an appropriate value for the $\zeta_{\rm eff}$ parameter as described above. We find that the power spectrum of the electron fraction from the semi-numerical box agrees very well with the radiative transfer model. The difference in power is less than 10% on most scales. This validates the semi-numerical approach and our calibration of it. We then proceed to consider the electron fraction power spectrum in the semi-numerical method implemented on boxes with lengths 500 cMpc/h and 1000 cMpc/h. These large boxes are also tuned to have the same reionization history as the fiducial model. They have identical power as the fiducial model on small scales but show excess power at large scales. This excess power arises due to ionized regions around high-mass haloes that are not present in the smaller box. The agreement on small scales is good because we use the same minimum halo mass value of 10^9 $\mathrm{M}_\odot$ in every semi-numerical simulation. The Roy et al. 2017 curve is based on a semi-analytical model of reionization in which ionized bubbles follow a log-normal distribution when reionization is at the 50% level [181]. This distribution is characterized by two free parameters: a characteristic bubble radius (R_b) and variance of the log normal distribution (σ_{lnr}). One bubble correlations dominate on scales $k \geq 1$ while large scales are dominated by the correlation between different ionized bubbles.

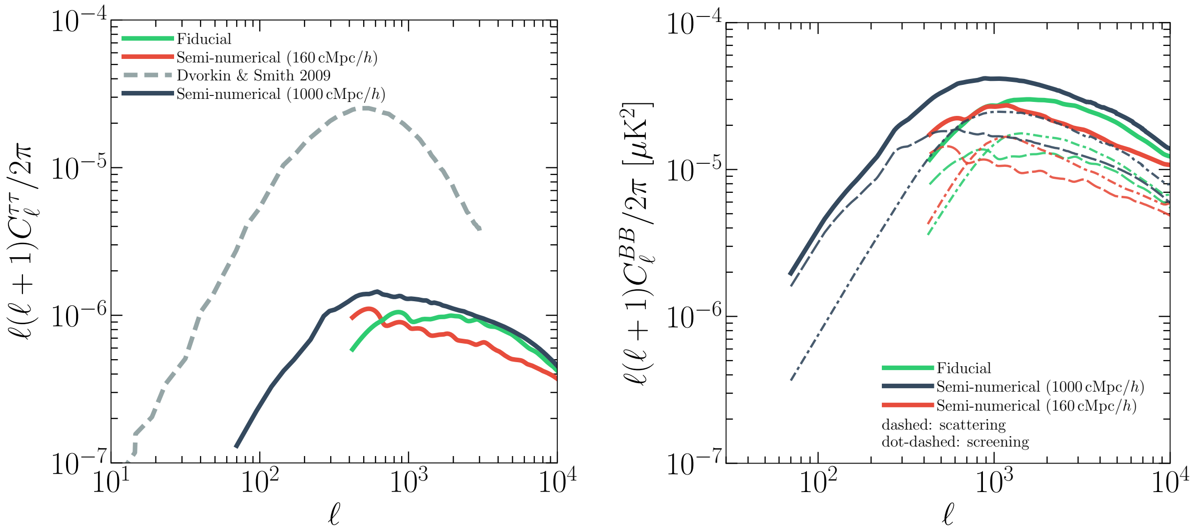

Figure 4.5: Left panel shows the opacity power spectrum in our fiducial radiative transfer simulation (green curve), semi-numerical simulation in the 160 cMpc/h box (red curve), and the semi-numerical simulation in the 1 cGpc/h box (black curve). All three simulation have identical reionization histories. The dashed grey curve in this panel shows the opacity power spectrum from [127] for comparison. The right panel shows the induced B-mode power spectrum in our three simulation boxes. The dashed and dot-dashed curves show the scattering and screening contributions, respectively, to the power spectrum.

4.4 Results

4.4.1 Power spectrum of secondary B-mode anisotropies

In this Section we aim to estimate the B-mode signal from patchy reionization and estimate its contamination in the search for the primordial signal. Figure 4.5 (left panel) shows the optical depth fluctuations from the radiative transfer simulation compared to the simulations using the excursion set algorithm calibrated to the radiative transfer simulation. The simulation larger than 160 cMpc/h is calibrated on scales to the radiative transfer simulations where the angular scales overlap. $C_\ell^{\tau\tau}$ agrees well at $\ell \gtrsim 700$ for the various size simulations. $C_\ell^{\tau\tau}$ from the 1000 cMpc/h box is roughly ~ 20 and ~ 15 times smaller than the signal studied by [127] at $\ell \sim 100$ and $\ell \sim 1000$ respectively. The amplitude of $C_\ell^{\tau\tau}$ strongly depends on the minimum mass of the dark matter halo where the ionizing sources reside. While we use a different reionization history and morphology, the amplitude of $C_\ell^{\tau\tau}$ matches the findings of [182].

The right panel of Figure 4.5 shows the B-mode signal due to patchy reionization. B modes due to scattering have more power on large scales, $\ell \lesssim 600$ for different simulations, compared to the B modes generated by screening. Screening B modes are sourced by a modulation of the primordial E modes and act as white noise on scales where E modes have less power and only have significant modulations by τ fluctuations where E modes have more power. In contrast, B modes due to scattering depends on the large scale power of $C_\ell^{\tau\tau}$ and it increase if $C_\ell^{\tau\tau}$ has more power at those scales.

The total C_ℓ^{BB} peaks on scales between $\ell \sim 1000$ to 2000, where primordial E modes have maximum power and where τ fluctuations are larger. On the other hand, B modes due to scattering are determined by the shape of the τ power spectrum with $Q_{\rm rms}$ assumed to be constant. We show the total power spectrum in Figure 4.5. In the remainder of this Chapter we will always refer C_ℓ^{BB} as the total B-mode signal due to the sum of scattering and screening. The power spectrum amplitude derived from the semi-numerical method for 1 Gpc box is ~ 2 times larger than that in the fiducial box. This is due to the presence of clustering of bubbles around massive haloes that are present in the 1 cGpc box but are absent in the smaller 160 cMpc/h box. Power spectra of x_e on large scales are driven by those massive haloes; hence, the amplitude of the tau and B-mode power spectrum is higher on those scales than for the fiducial simulation.

In Figure 4.6, we show the level of potential contamination of patchy reionization on the primordial B-mode signal from gravitational waves. Instrumental noise power spectra of future CMB experiments are modeled as $N_\ell^{BB} = \Delta_P^2 \exp[(\ell(\ell+1)\Theta_f^2)/8\ln(2)]$ [276]. Here Δ_P is the detector noise in polarization which is related to the detector noise in temperature, Δ_T, as $\Delta_P = \sqrt{2}\Delta_T$ and Θ_f is the fixed full width half maximum (FWHM) of the beam. We consider four instrumental noise curves for the four different future CMB experiments. We consider the $\Delta_T = 2.1$ μK-arcmin and $\Theta_f = 17$ arcmin for the small aperture telescope (SATS) of Simons observatory [53]. For CMB-S4, we show the noise power spectra corresponding to $\Delta_T = 1$ μK-arcmin and $\Theta_f = 3$ arcmin [277, 54]. As these ground-based telescopes will not be able to observe the full sky, they will be able to go down till $\ell \sim 20$. LiteBIRD is the only presently funded satellite mission to measure the temperature and polarization anisotropies of the CMB with 15 frequency bands from 40 GHz to 402 GHz in the multipole range 2 to 200 [176]. For the detection of primordial B modes, the LiteBIRD forecast is $\sigma(r) \lesssim 10^{-3}$ with $r = 0$. For LiteBIRD, the total sensitivity will reach at $\delta_T = 1.7$ μK-arcmin with relatively large beam size, $\Theta_f = 30$ arcmin. There are other proposed CMB experiments which will have more advanced technologies to measure the CMB anisotropies with very high sensitivity. We only plot the instrumental noise of PICO with $\Delta_T = 0.6$ μK-arcmin and $\Theta_f = 7.9$ arcmin. Several ground-based telescopes such as the advanced ACT, SPTpol, BICEP3, Simons array [109, 220, 278, 205] are operating at present. Their sensitivity is less than the four reference noise curves we show in Figure 4.6. Future space CMB missions will aim to measure the primordial B-mode signal by observing the reionization bump at $\ell \leq 20$ as well as the recombination signal at $\ell \geq 20$, while future ground-based experiments, primarily due to atmospheric noise, will target the recombination bump only. Ideally, ground-based experiments are expected to reach a multipole $\ell_{\rm min} \sim 30$ in polarization. We show three primordial B-mode power spectra corresponding to $r = 10^{-2}$, 10^{-3} and 10^{-4}. Joint analysis of CMB data by the Planck and BICEP collaborations have put an upper limit on the amplitude on the tensor-to-scalar ratio, $r \lesssim 0.06$ at 95% confidence [98].

CMB photons are also lensed due to the gravitational potential of matter along the line of sight. Primary E modes are transformed into lensed B modes, even if there is no primordial B-mode signal. B modes due to lensing can be considered as white noise with a corresponding Δ_T =5 μK-arcmin within the scales of interest. Future (grounds-based) CMB experiments will need to remove the lensing B-mode signal using "delensing" techniques to probe primordial gravitational waves for $r \leq 10^{-3}$.

In Figure 4.6 we also show the B-mode signal produced by patchy reionization using the radiative transfer simulation. We compare these with previous studies using a semi-analytic model [181, 127, 107]. On large scales, the x_e power spectra behave as a power law in k because $P_{x_e x_e}$ is shot noise dominated on those scales. As a result, the B-mode power spectrum follows a power law on large angular scales. The signal calculated using the semi-analytic model predicts a larger signal than the radiative transfer simulations. We should note that reionization history used in Ref. [127] is based on the WMAP data for which $\tau = 0.089$. Typically the B-mode signal due to patchy reionization peaks at a scale comparable to the characteristic bubble size. Previous studies considered larger ionized bubbles with a characteristic bubble radius $R_b \sim 5$ Mpc. This shifts the peak of the B-mode spectra towards larger scales ($\ell \sim 100-500$). Instead, our simulation driven results show that B modes peak at scales ($\ell \sim 1000$) where the lensing dominates the polarized sky. The B-mode signal determined using the radiative transfer simulation matches the B-mode signal calculated in Ref. [279], using photon conserving semi-numerical simulations, around $\ell \sim 100$. We compare those results to a simulation where we set $M_{\rm min} = 10^9\ M_\odot$. While Ref. [279] considered only the scattering term we also include the screening term. On large scales, $\ell \lesssim 100$, B modes due to scattering exceed B modes due to screening, so even when we include the screening B modes, the results of these independent studies do not differ significantly.

More quantitatively, in section 4.4.3, we will show that patchy reionization will have a limited impact on the detection of a primordial signal for $r = 10^{-3}$. However, it could bias the amplitude of the primordial B modes for $r = 10^{-4}$ or less. As the patchy signal falls down rapidly below $\ell \lesssim 100$, there will be negligible contamination on the reionization bump ($\ell \lesssim 20$) even if r is as low as 10^{-4} and hence it will not be a concern for future space-based missions such as LiteBIRD [176].

Next, we explore the amplitude of the B-mode signal due to reionization for different reionization histories, with a simple tanh functional behaviour. We consider tanh reionization histories parameterized by the mean redshift of reionization, $z_{\rm re}$ and the width of the reionization, Δz. The ionization fraction evolves as

$$x_e(z) = \frac{1}{2} + \frac{\tanh(y_{\rm re} - y)}{2\Delta y}, \tag{4.19}$$

where $y(z) = (1+z)^{3/2}$, $y_{\rm re} = y(z_{re})$ and $\Delta y = 1.5\sqrt{1+z_{re}}\Delta z$ [280]. In Figure 4.7 we show reionization histories with different $z_{\rm re}$ and Δ_z to explore how the reionization induced B modes change in shape and amplitude.

In Figure 4.7 we show the B-mode signal for a tanh reionization model (see Figure 4.7). The figure also shows a rather unlikely reionization history to show the effect on the B-mode signal. The optical depths for these unlikely reionization histories are excluded by the constraints on τ given by *Planck*.

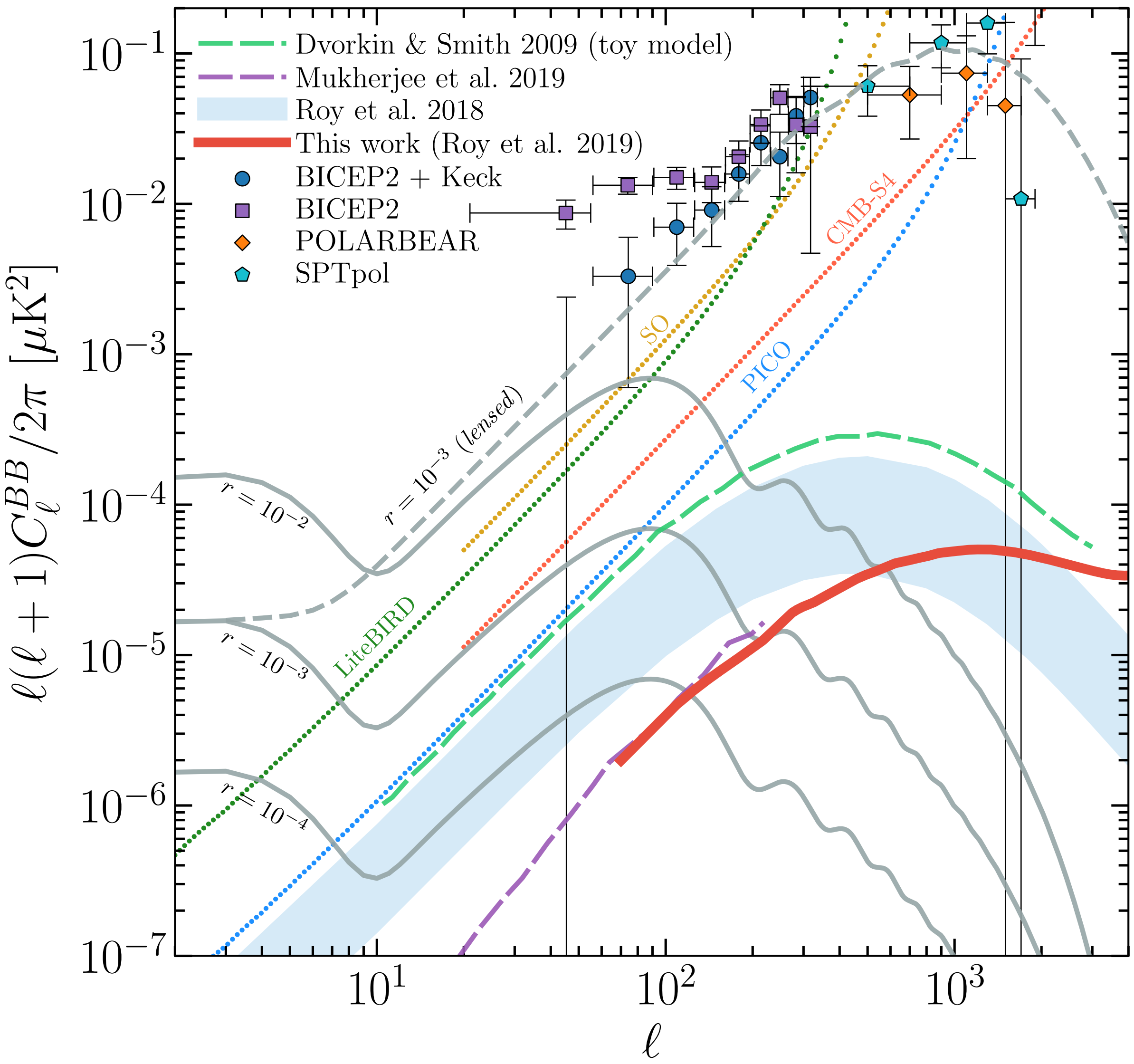

Figure 4.6: The thick red curve shows our prediction for the reionization-induced B-mode power spectrum. This can be compared with the prediction previously reported in the literature ([279, dashed purple curve], [107, blue shaded region], and [127, dashed green curve]). Dotted curves show sensitivities for PICO (blue curve), CMB-S4 (red curve), LiteBIRD (green curve), and Simons Observatory (yellow curve). The three grey curves show the primordial B-mode power spectra corresponding to the tensor-to-scalar ratio $r = 10^{-2}$, 10^{-3}, and 10^{-4}. Secondary B modes induced by lensing are shown by the grey dashed curve for the $r = 10^{-3}$ case. Data points show B-mode measurements by BICEP2 [97], BICEP2+Keck [212], POLARBEAR [100] and SPT [99].

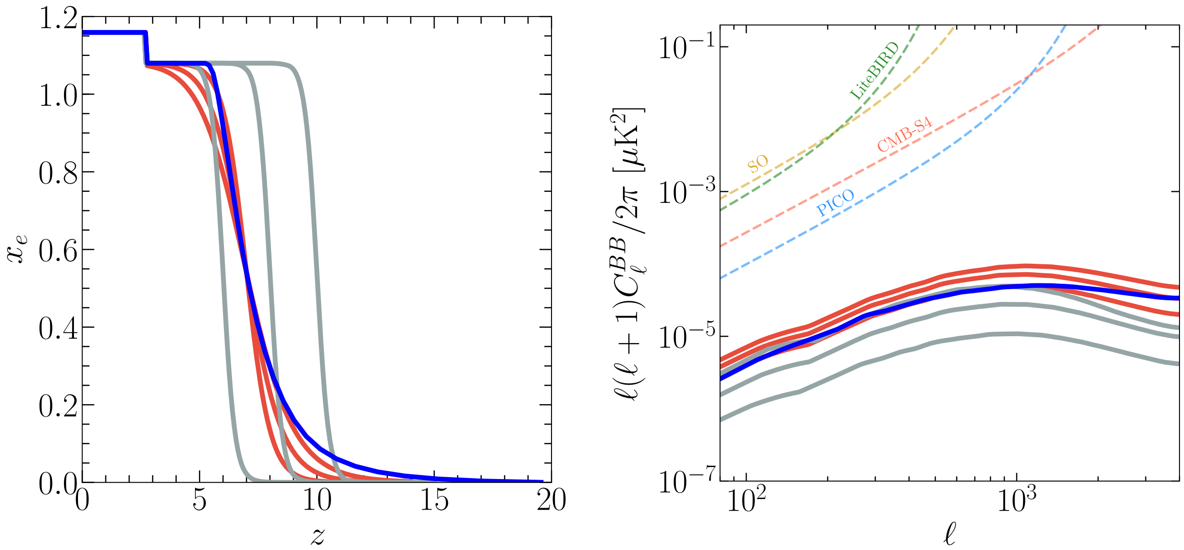

Figure 4.7: Sensitivity of our predicted secondary B-mode signal to the reionization redshift and duration. The blue curve shows our fiducial model. The red curves in the left panel show reionization histories modelled using a tanh function from Equation (4.19) with $z_{\rm re} = 7$ and for $\Delta z = 1, 1.5$, and 2. The corresponding B-mode signal is shown by the red curves in the right panel. The amplitude of the B-mode signal is higher for larger values of Δz. Similarly, the grey curves in the left panel show reionization histories modelled using the same tanh function with $\Delta z = 0.5$ for $z_{\rm re} = 6, 8$, and 10. The corresponding B-mode signal is shown by the grey curves in the right panel. The amplitude of the B-mode signal is higher for larger values of $z_{\rm re}$. The dashed curves in the right panel show sensitivities for PICO (blue curve), CMB-S4 (red curve), LiteBIRD (green curve), and Simons Observatory (yellow curve). The dashed green curve shows the primordial signal for $r = 10^{-3}$.

4.4.2 Minimum mass of reionization sources

In our fiducial simulation, sources of reionizing radiation are placed in haloes with masses down to 10^9 M$_\odot$. The mass of reionization sources will have an effect on the clustering of the free electron distribution during reionization [281, 230], which can, in turn, change the induced secondary B modes. The agreement of our radiative transfer simulation with a variety of data [235, 282] suggests that sources in haloes down to 10^9 M$_\odot$ should be able to reionize the Universe. Still, the mass of reionizing sources is unfortunately unknown. The fraction of hydrogen-ionizing radiation produced in a galaxy that can escape into the intergalactic medium and cause reionization is largely uncertain. This escape fraction has been measured in a handful of relatively bright and low-redshift galaxies [283, 284, 228, 285, 286, 287, 288, 289, 290, 291, 227, 292, 293, 284] and is unknown for the galaxies within the epoch of reionization. This quantity can be a function of halo mass and can decide, e.g., the relative contribution of highly-clustered massive haloes and low-mass haloes to reionization. Further, active galactic nuclei (AGN), which are known to have unit escape fraction, can also reionize the Universe instead of star-forming galaxies. Such a scenario,

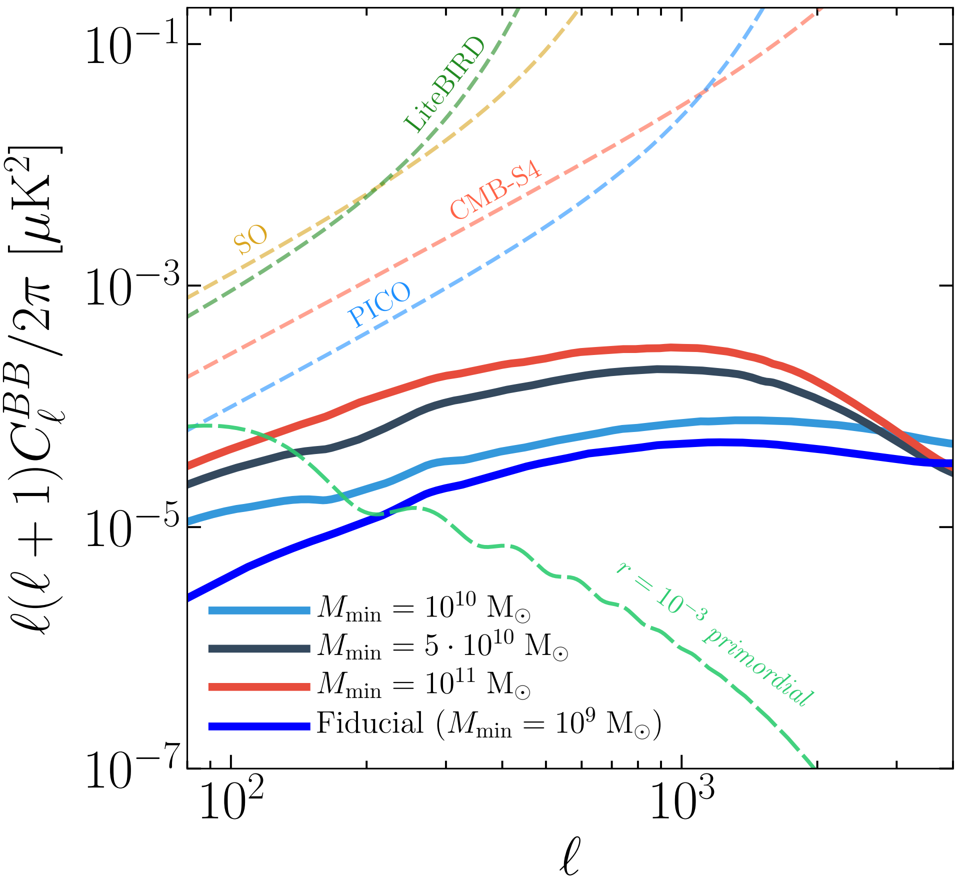

Figure 4.8: Dependence of the induced B-mode power spectrum on the the minimum mass of reionizing sources for a fixed reionization history. Sources in higher-mass haloes induce larger B-mode power due to their stronger clustering. The dashed curves show sensitivities for PICO (blue curve), CMB-S4 (red curve), LiteBIRD (green curve), and Simons Observatory (yellow curve). We also show the primordial signal for $r = 10^{-3}$ with a green dashed line.

although unlikely [225], can potentially have a large effect on the induced B-mode signal as AGN reside in very high mass haloes that are highly clustered [230].

In Figure 4.8, we increase the minimum mass of reionizing sources in our model from $M_{\rm min} = 10^9\ M_\odot$ to a few $10^{11}\ M_\odot$. This is done using the excursion-set-based treatment described above. The reionization history is always kept the same as our fiducial simulation (Figure 4.1) by changing the brightness of each halo suitably, i.e., by tuning the parameter $N_\gamma^{\rm LyC}$ in Equation 4.12. As a result, as $M_{\rm min}$ is increased, the ionized regions increase in size and become more clustered [230]. This results in an enhancement of about an order of magnitude in the induced B-mode power spectrum, as seen in Figure 4.8.

4.4.3 Constraints on the tensor-to-scalar ratio

We now quantitatively consider the effect of reionization-induced secondary B modes on the inference of the tensor-to-scalar ratio from the B-mode power spectrum.

The primordial B-mode power spectrum has a recombination bump at $\ell \sim 100$. Future CMB experiments aim to target this recombination bump in search for primordial gravitational waves. For small values of the tensor-to-scalar ratio, the signal-to-noise ratio (S/N) is expected to $\ll 1$ per mode, but the cumulative S/N could exceed 1 after summing over a few multipoles [53, 54, 52, 294]. Also, foreground contamination exceeds the primordial signal for $r \sim 10^{-3}$ [276, 92, 295]. As a result, the precise the shape of the B-mode power spectrum will be hard to determine and it will be a challenge to distinguish the primordial signal from other sources if the shape of these other sources is not sufficiently dissimilar within the range of multipoles considered.

Let us define an 'effective' tensor-to-scale ratio, r_{eff}, by summing the power spectrum on a range of scales from ℓ'_{min} to ℓ'_{max}, so that

$$\sum_{\ell'_{\text{min}}}^{\ell'_{\text{max}}} C_\ell^{BB}(r_{\text{eff}}) = \sum_{\ell'_{\text{min}}}^{\ell'_{\text{max}}} C_\ell^{BB}(r) + \sum_{\ell'_{\text{min}}}^{\ell'_{\text{max}}} C_\ell^{BB(\text{sec})}. \tag{4.20}$$

Here, $C_\ell^{BB(\text{sec})}$ represents B modes induced by non-primordial sources such as lensing, patchy reionization, and foreground emission. r_{eff} is thus the tensor-to-scalar ratio assigned to a measurement of the mean power measured on a range of scales if all of this measured power is assumed to be primordial; summing over a range of scales allows us to disregard the shape of the power spectrum. The effective tensor-to-scalar ratio r_{eff} is equal to the 'true' r if secondary contamination is negligible; in the presence of secondary contamination $r_{\text{eff}} > r$. For example, if we consider lensing B modes the single source of secondary contamination, i.e., $C_\ell^{BB(\text{sec})} = C_\ell^{BB(\text{lensing})}$, $r_{\text{eff}} > r$ for $r \sim 0.5$ (and for all smaller values of r as the lensing B modes remain unchanged). This is shown in Figure 4.9. Since contamination due to patchy reionization on the primordial signal will only affect ground-based experiments, we limit ourselves in Figure 4.9 to scales targeted from the ground (approximately $80 \leq \ell \leq 120$).

Figure 4.9 also shows how different patchy reionization scenarios discussed in the previous sections can change the value of r_{eff}. The lensing signal is ~ 55 times larger than the primordial signal for $r = 10^{-3}$. Secondary B modes from patchy reionization can bias the tensor-to-scalar ratio r when $r \sim 10^{-3}$ and below. If reionization is driven by rare sources (e.g. $M_{\text{min}} \sim 10^{11}$ M$_\odot$), r_{eff} could be as large as 4×10^{-4} for $r \sim 10^{-4}$. Reionization-induced B modes could generate a 5% to 40% bias on a measurement of $r = 10^{-3}$ if $M_{\text{min}} = 10^9$ M$_\odot$ (our fiducial model) and 10^{11} M$_\odot$, respectively. For a future satellite experiment (e.g. PICO [52] or CMB Bharat [51]), $r = 5 \times 10^{-4}$ could be biased at the $\simeq 10\%$ to $\simeq 75\%$ for $M_{\text{min}} = 10^9$ M$_\odot$ and 10^{11} M$_\odot$, respectively, if these experiments would only measure the recombination bump. The vertical lines show the target of r forecasted for the detection of primordial B modes by Simons Array, BICEP array [204], Simons Observatory [85], by CMB-S4 [206]. We show only the targets of r set by future ground based CMB experiments in this figure as our forecast for r_{eff} is made for the detection of the recombination bump in the primordial B-mode power spectra. Space based missions will constrain r by probing both reionization bump and recombination bump. As the reionization induced B has negligible power on the scales of

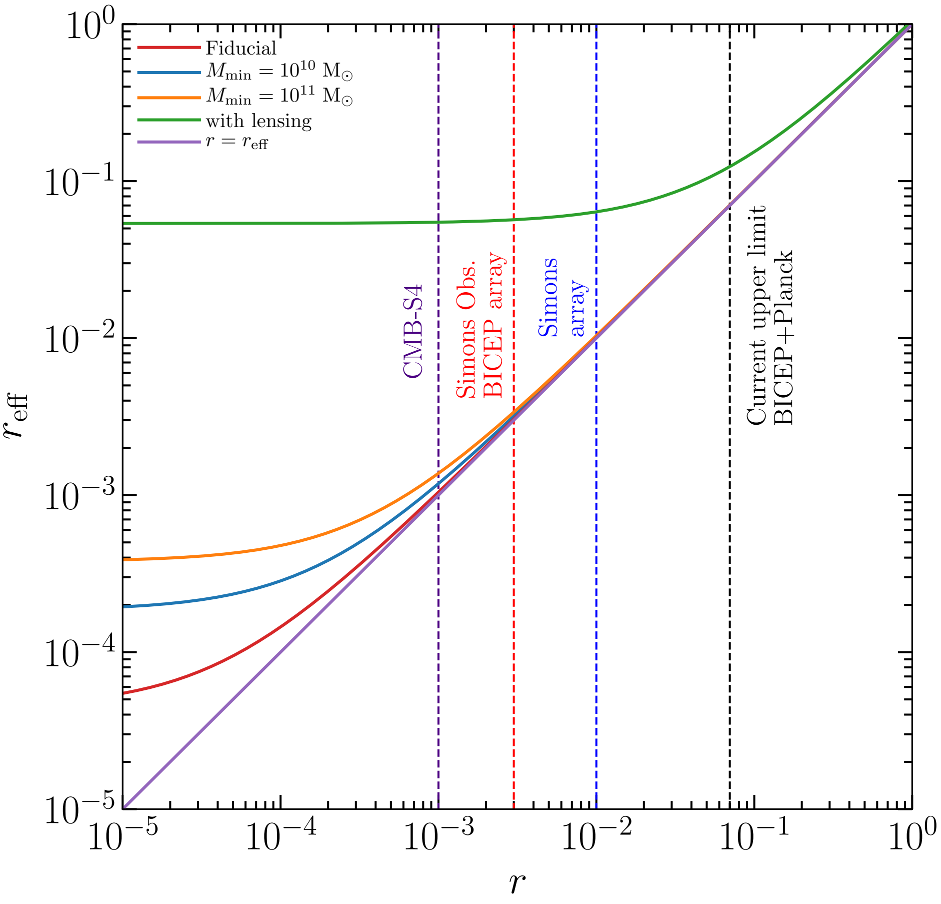

Figure 4.9: Solid lines show the effective tensor-to-scalar ratio $r_{\rm eff}$ that may be inferred in the presence of a secondary B-mode signal as a function of the true tensor-to-scalar ratio r. The red curve corresponds to our fiducial reionization model. Other curves show the change in the result when varying the minimum mass of the ionizing sources. The green curve shows the $r_{\rm eff}$ due to lensing. Vertical lines show the current upper limit on r and predicted experimental sensitivities.

the reionization bump ($\ell < 10$), for the space based experimenters will not be affected by the reionization induced B modes.

We now discuss the effect of patchy reionization on the significance of a potential measurement of the tensor-to-scalar ratio. The observed B-mode power spectrum is given by

$$C_\ell^{BB({\rm total})} = C_\ell^{BB({\rm reion})} + C_\ell^{BB({\rm primordial})} + C_\ell^{BB({\rm res-len})}. \tag{4.21}$$

Here, $C_\ell^{BB({\rm res-len})}$ is the residual lensing B-mode signal after delensing. We set $C_\ell^{BB({\rm res-len})} = 0$ to only check the effects of reionization for the detection of primordial B modes. Therefore, the covariance matrix can be written as

$${\rm Cov}_{BB} = C_\ell^{BB({\rm total})} + N_\ell^{BB}, \tag{4.22}$$

where N_ℓ^{BB} is the instrumental noise for the measurement of B-mode polarization. While

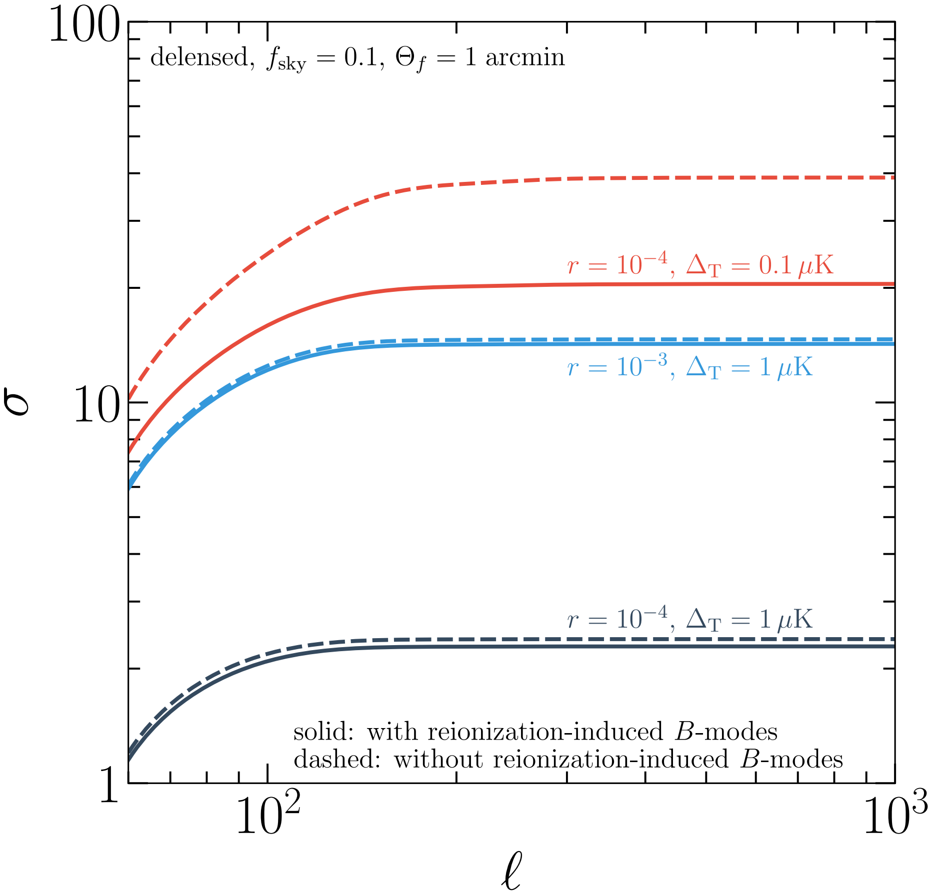

Figure 4.10: Estimated uncertainty σ_r on a measurement of the tensor-to-scalar ratio r in presence of reionization-induced secondary B-modes (solid curves) and without reionization-induced secondary B-modes (dashed curves). The three sets of curves correspond to different values of r and/or instrumental sensitivity. We have assumed a completely delensed signal.

the signal-to-noise ratio (S/N), r/σ_r, is defined so that [296, 297]

$$\sigma_r \equiv \frac{r}{S/N} = \sum_\ell (2\ell+1) f_{\rm sky} \left[\frac{C_\ell^{BB({\rm primordial})}}{r \times {\rm Cov}_{BB}} \right]^2 , \tag{4.23}$$

is the uncertainty on a measurement of r. Here, $f_{\rm sky}$ is the fraction of sky observed by an experiment. We calculate cumulative S/N by fixing the lowest multipole, ℓ_{min} at 70. The result is shown in Figure 4.10, where we demonstrate how the reionization-induced B-mode could change the forecasts for the detection of primordial B modes. In this figure, we assume that there is no residual lensing signal (i.e., we assume 100% delensing) and $f_{\rm sky} = 10\%$. We also assume that foregrounds have been removed using multi-frequency data. The uncertainty σ_r reduces from 14.6 to 14.3 when we include $C_\ell^{BB({\rm reion})}$ with the primordial B-mode power spectra corresponding to $r = 10^{-3}$. The changes are small because of instrumental noise N_ℓ^{BB} with $\Delta_T = 1$ μK-arcmin always dominates over the primordial and reionization induced B modes and also $C_\ell^{BB({\rm reion})}$ is almost one order of magnitude smaller than the primordial B modes at $\ell \sim 100$. With the above mentioned instrumental noise, σ_r changes from 2.4 to 2.25 when we add reionization induced B modes with the primordial B modes corresponding to $r = 10^{-4}$. Next, we consider an experiment operating with $\Delta_T = 0.1$ μK-arcmin to probe the primordial B-mode signal so that instrumental noise becomes comparable with the reionization-induced B modes. For $r = 10^{-4}$, the primordial B modes and reionization-induced B modes are also comparable in amplitude at $\ell \sim 100$. This forecast will be more complicated if we include residuals of complex foreground and residual lensing signal in Equation (4.21). Inclusion of reionization-induced B modes has a large effect on the detectability of primordial B-mode signal for $r = 10^{-4}$ as it could change the detection significance from 37σ to 20σ without including residual foregrounds due to synchrotron and dust emission. This figure shows that we can safely neglect the reionization-induced B modes for the detection of primordial B modes for $r \geq 10^{-3}$.

4.5 Discussion

We have investigated the imprint of patchy reionization on the cosmic microwave background polarization anisotropies by studying the amplitude of the B-mode signal. The amplitude of the B-mode signal for patchy reionization depends on the reionization history and the morphology and clustering of the ionized regions. Compared to previous studies, we used realistic radiative transfer simulations of reionization to estimate the B-mode signal. These simulations are calibrated to match the Thomson scattering optical depth measured by *Planck* and the mean transmission fraction of the Lyα forest. With this calibration, these simulations have been found to successfully match a variety of observations related to reionization, such as the observed spatial fluctuations in the Lyα opacity of the IGM, the ionization fraction inferred from the frequency of dark pixels in Lyα forest spectra, quasar near zones, as well as the Lyβ opacity of the IGM. While these radiative transfer simulations model reionization on scales up to 160 cMpc/h (236 cMpc), we extrapolate them to scales up to 1 cGpc by using an excursion-set-based approach. In this model, reionization begins at redshift $z \sim 15$, is halfway complete at $z = 7$, and finishes at $z = 5.2$.

We find that the B-mode signal due to scattering and screening of CMB photons during reionization is more than one order of magnitude lower than the primordial B modes at $\ell \sim 100$ for $r \sim 10^{-3}$ but the amplitude of the signal is comparable with primordial B modes with $r \sim 10^{-4}$ at those scales.

Two factors play an important role in determining the amplitude of the B-mode power spectra induced by reionization: (a) the ionization history, and (b) the minimum mass of the ionizing sources. For a given minimum mass of ionizing sources, early reionization scenarios give rise to higher amplitudes of the induced B-mode power spectrum, although such early reionization scenarios appear to be ruled out by a variety of astrophysical data. For a given reionization history, the amplitude of the B-mode power spectrum increases with the minimum mass of ionizing sources. At $\ell \sim 100$, even relatively extreme assumptions about the ionization history or the minimum mass of ionizing sources do not increase the B-mode power spectrum beyond the primordial signal for $r \sim 10^{-3}$.

Near-future experiments such as Simons array, Simons observatory, CMB-S4, CLASS [109, 53, 54, 278], aim to reach down to $r \sim 10^{-3}$ for measuring the primordial B-mode power at $\ell \sim 100$. We expect these experimental attempts to detect primordial gravitational waves to be safe from reionization-induced contamination. Future space missions such as LiteBIRD, PICO, CMB-Bharat allow to target both the reionization ($\ell \lesssim 20$) and recombination bump [294, 52, 51]. We confirm that reionization-induced B modes will have little effect on these large scales.

For ground-based experiments that can reach $r < 10^{-4}$, contamination from reionization could become significant and might have to be addressed in order to establish the nature of the measured signal. For these experiments, the reionization-induced B modes can affect the significance of any detection of the primordial signal.

The latter would require both “de-screening" and “de-scattering". All screening does is modulate the spectrum due to patchy reionization captured by $P_{x_e x_e}$. If reionization induced B modes are measured then one can thus reconstruct this map, and de-screen the data very similar to use the lensing map to delens the data. If we have a good proxy for the ionization power spectrum, we can use that (similar to the CIB for lensing). While de-screening would be very similar to de-lensing, de-scattering would be harder. Fortunately, the scattering contribution is sub-dominant on the scales of interest ($1000 \lesssim \ell \lesssim 2000$) for the detection of patchy B modes.

In conclusion, we don’t expect the search for primordial B modes will be hindered by patchy reionization in the near future. For more conventional reionization histories, all currently planned CMB experiments should be safe from significant contamination.

Future Perspectives

> Considerate la vostra semenza:
> fatti non foste a viver come bruti,
> ma per seguir virtute e canoscenza
>
> *Dante Alighieri*

All the chapters described in the thesis address several of the most fundamental questions in Cosmology and extra-galactic astrophysics related to the detection of patchy reionization by probing the optical depth fluctuations and cross-correlation studies with LSS probes, physics of reionization and secondary anisotropies in CMB due to astrophysical phenomena at later time, contamination on the primordial B modes due to the patchy reionization. However, there are still many other reasons to explore the possibilities to probe the signature of patchy reionization, in large part opened by the studies presented here. We plan to investigate these possibilities in future as a continuation of the works done in this thesis.

In Chapter 2 we did all the analysis of optical depth reconstruction without considering the effect of other contamination which can bias our results. Foreground emission due to dust and synchrotron and the lensed B-mode signal could be a major source of contamination. In the near future, we plan to use unbiased hybrid estimator which simultaneously fit both the lensing and patchy τ contributions [182, 298]. The recent synchrotron foreground template based on the SPASS observation is available at 2.3 GHz [299] whereas the dust emissions could be modelled following [300]. So, there is a room for improvement the forecasts of the detectability of τ by future CMB experiments by considering these potential sources of bias.

Cross-correlation studies between CMB and LSS is one of the promising probes to study the morphology of reionization, which we investigated in chapter 3. We can use other probes as well when we have data from the radio surveys. For example, hydrogen intensity mapping is a futuristic probe, but simulations, parameter estimations and data analysis techniques could be followed by the lessons learnt from CMB experiments. It is very interesting to inspect whether we can use upcoming polarization experiments to give us an insight into the optical depth in electrons around quasars and galaxies. One of my interests is to compute the detectability of the cross-correlation of this signal with the electrons around galaxies and quasars between LSST/Euclid and Simons Observatory/CMB-S4. Our ultimate and most optimistic goal is to reconstruct an “optical depth (τ) map” from the observed CMB map, analogous to the "CMB lensing potential" map. This map will be extremely interesting as it will act as an electron density template in the Universe, and it will be beneficial to understand the physics of reionization and galaxy clusters. One of the main scientific goals in measuring the electron optical depth around high-redshift quasars and galaxies (Lyman alpha emitters, Lyman Break Galaxies) is to test whether these sources may be responsible for the cosmic reionization and to constrain the redshift and duration of the reionization itself. In principle, It will put constraints on reionization additional to the standard τ measurement from CMB polarization. On the other side, consistent results are found from the complementary approach, by looking at the production rate of ionizing photons estimated from the "proximity effect", i.e., the relative lack of Lyα absorption in the vicinity of a QSO. Measured electron profile around QSOs will be able to address this issue through an alternative approach.

In chapter 4 Our study shows that B-modes produced through this process could 1) be observed with future B-mode experiments such as CMB-S4 and b) would represent a disturbance in B-mode searches for primordial gravitational waves, possibly generating a signal at $r > 0.001$. Both strongly motivate a careful study of this signal. If detected, the signal would provide us with unique insights into the reionization history as well as the sources that produced the ionizing photons, as we have shown. Meanwhile, if the signal is indeed large enough to be detected, it will become necessary to address mitigation techniques (such as descreening) or joint fitting against the total CMB B-mode signal. Forthcoming projects along these lines are 1) to estimate the amplitude of the patchy B-mode signal by using different simulations of reionization which agrees well with the available data so far; 2) inspection of the level of contamination due to patchy reionization on primordial B-mode signal; 3) exploration of the possibility to detect this new signal which will be direct evidence of reionization; 4) analyzing the CMB polarization data from the Simons Observatory/CCAT-p to extract the patchy reionization signal and constrain reionization parameters and 5) developing algorithms/tools to separate this signal from the primordial B-mode signal.

As a final development following the work in this Thesis, I would like to mention the kSZ signal. It is an excellent probe of the growth factor of the Universe, which could be used to understand the behaviour of dark energy. Recently there is a more than 3.5 σ tension of the measurement of Hubble constant between CMB and low redshift datasets by different probes (such as supernovae and quasars). We would like the investigate whether combined datasets of kSZ and tSZ could be an alternative probe to understand the behaviour of dark energy through the measurement of Hubble constant. In this line of research my goals are as follows: 1) work on simulations and algorithm to check the efficiency to separate early and late time kSZ signal; 2) cross correlate available lensing maps with kSZ maps to study the behaviour of dark of energy and the role of modified gravity in structure formation; 3) using kSZ signal to constrain cosmological parameters such as $\sum m_\nu$, σ_8 and w; 4) check if this can be used as an alternative probe to measure the value of the Hubble constant which could be used to provide further details on the tension between CMB and low redshift data sets. The Simons Observatory and CMB S4 are going to put constraints on patchy reionization by observing patchy kSZ and aims to separate the late and early time kSZ by studying this signal on different scales based on techniques proposed by Smith and Ferraro 2017. CCAT-p could detect the patchy kSZ signal if the signal is large enough and is adequately separated from the early time kSZ signal. However, it is not clear how the different morphological scenarios of the reionization process can change the scale dependencies of the patchy kSZ signal. We plan to investigate this problem in two ways; one is to calculate the kSZ 4-point correlation function by using state of the art simulations of reionization; the same one I used to study the patchy B-mode signal. Alternatively, I plan to cross correlate kSZ^2 signal with redshifted CII observation to probe the epoch of reionization. During the postdoc tenure, we want to take this opportunity to perform this cross-correlation studies as both signals will be measured by CCAT-p experiment.

Bibliography

[1] G. Gamow, *The origin of elements and the separation of galaxies*, *Phys. Rev.* **74** (Aug, 1948) 505–506.

[2] G. Gamow, *Expanding Universe and the Origin of Elements*, *Physical Review* **70** (Oct., 1946) 572–573.

[3] R. A. Alpher, G. Gamow and R. Herman, *Thermal Cosmic Radiation and the Formation of Protogalaxies*, *Proceedings of the National Academy of Science* **58** (Dec., 1967) 2179–2186.

[4] A. A. Penzias and R. W. Wilson, *A Measurement of Excess Antenna Temperature at 4080 Mc/s.*, *ApJ* **142** (July, 1965) 419–421.

[5] E. Hubble, *A Relation between Distance and Radial Velocity among Extra-Galactic Nebulae*, *Proceedings of the National Academy of Science* **15** (Mar., 1929) 168–173.

[6] E. Hubble and M. L. Humason, *The Velocity-Distance Relation among Extra-Galactic Nebulae*, *ApJ* **74** (Jul, 1931) 43.

[7] C. Misner, K. Thorne, J. Wheeler and D. Kaiser, *Gravitation*. Princeton University Press, 2017.

[8] H. P. Robertson, *Kinematics and World-Structure*, *ApJ* **82** (Nov., 1935) 284.

[9] A. Friedmann, *Über die Krümmung des Raumes*, *Zeitschrift fur Physik* **10** (1922) 377–386.

[10] G. Lemaître, *Expansion of the universe, A homogeneous universe of constant mass and increasing radius accounting for the radial velocity of extra-galactic nebulae*, *MNRAS* **91** (Mar., 1931) 483–490.

[11] J. P. Ostriker and P. J. Steinhardt, *Cosmic Concordance*, *arXiv e-prints* (May, 1995) astro–ph/9505066, [`astro-ph/9505066`].

[12] S. Dodelson, *Modern Cosmology*. Academic Press, Elsevier Science, 2003.

[13] Planck Collaboration, N. Aghanim, Y. Akrami, M. Ashdown, J. Aumont, C. Baccigalupi et al., *Planck 2018 results. VI. Cosmological parameters*, *ArXiv e-prints* (July, 2018) , [`1807.06209`].

[14] A. H. Guth and E. J. Weinberg, *Could the Universe Have Recovered from a Slow First Order Phase Transition?*, *Nucl. Phys.* **B212** (1983) 321–364.

[15] A. D. Linde, *Inflationary Cosmology*, *Lect. Notes Phys.* **738** (2008) 1–54, [`0705.0164`].

[16] A. H. Guth, *Inflationary universe: A possible solution to the horizon and flatness problems*, *Phys. Rev. D* **23** (Jan, 1981) 347–356.

[17] A. H. Guth and S. H. H. Tye, *Phase Transitions and Magnetic Monopole Production in the Very Early Universe*, *Phys. Rev. Lett.* **44** (1980) 631.

[18] A. Linde, *A new inflationary universe scenario: A possible solution of the horizon, flatness, homogeneity, isotropy and primordial monopole problems*, *Physics Letters B* **108** (1982) 389 – 393.

[19] A. F. Illarionov and R. A. Siuniaev, *Comptonization, characteristic radiation spectra, and thermal balance of low-density plasma*, *Soviet Astronomy* **18** (Feb., 1975) 413–419.

[20] G. Chabrier, *Galactic Stellar and Substellar Initial Mass Function*, *Publications of the Astronomical Society of the Pacific* **115** (July, 2003) 763–795, [`astro-ph/0304382`].

[21] Y. B. Zeldovich and R. A. Sunyaev, *The Interaction of Matter and Radiation in a Hot-Model Universe*, *Astrophysics and Space Science* **4** (Jul, 1969) 301–316.

[22] J. C. Mather, E. S. Cheng, D. A. Cottingham, R. E. Eplee, Jr., D. J. Fixsen, T. Hewagama et al., *Measurement of the cosmic microwave background spectrum by the COBE FIRAS instrument*, *ApJ* **420** (Jan., 1994) 439–444.

[23] R. Khatri, R. A. Sunyaev and J. Chluba, *Does Bose-Einstein condensation of CMB photons cancel μ distortions created by dissipation of sound waves in the early Universe?*, *A&A* **540** (Apr, 2012) A124, [`1110.0475`].

[24] C. Burigana, G. de Zotti and L. Danese, *Constraints on the Thermal History of the Universe from the Cosmic Microwave Background Spectrum*, *ApJ* **379** (Sep, 1991) 1.

[25] R. Khatri and R. A. Sunyaev, *Beyond y and μ: the shape of the CMB spectral distortions in the intermediate epoch,* $1.5 \times 10^4 < z < 2 \times 10^5$, *JCAP* **1209** (2012) 016, [`1207.6654`].

[26] D. J. Fixsen, E. S. Cheng, J. M. Gales, J. C. Mather, R. A. Shafer and E. L. Wright, *The Cosmic Microwave Background Spectrum from the Full COBE FIRAS Data Set*, *ApJ* **473** (Dec, 1996) 576, [`astro-ph/9605054`].

[27] D. Puy and P. Peter, *Primordial magnetic field and spectral distortion of cosmic background radiation*, *Int. J. Mod. Phys.* **D7** (1998) 489–498, [`astro-ph/9802329`].

[28] J. Chluba, *Science with CMB spectral distortions*, *arXiv e-prints* (May, 2014) arXiv:1405.6938, [`1405.6938`].

[29] S. Mukherjee, R. Khatri and B. D. Wandelt, *Polarized anisotropic spectral distortions of the CMB: Galactic and extragalactic constraints on photon-axion conversion*, *JCAP* **1804** (2018) 045, [1801.09701].

[30] H. Tashiro, E. Sabancilar and T. Vachaspati, *CMB Distortions from Damping of Acoustic Waves Produced by Cosmic Strings*, *JCAP* **1308** (2013) 035, [1212.3283].

[31] P. Pani and A. Loeb, *Constraining primordial black-hole bombs through spectral distortions of the cosmic microwave background*, *Phys. Rev. D* **88** (Aug, 2013) 041301, [1307.5176].

[32] A. Kogut, D. J. Fixsen, D. T. Chuss, J. Dotson, E. Dwek, M. Halpern et al., *The Primordial Inflation Explorer (PIXIE): a nulling polarimeter for cosmic microwave background observations*, JCAP **2011** (Jul, 2011) 025, [1105.2044].

[33] PRISM collaboration, P. André et al., *PRISM (Polarized Radiation Imaging and Spectroscopy Mission): An Extended White Paper*, *JCAP* **1402** (2014) 006, [1310.1554].

[34] U. Seljak and M. Zaldarriaga, *A Line of sight integration approach to cosmic microwave background anisotropies*, *Astrophys. J.* **469** (1996) 437–444, [astro-ph/9603033].

[35] J. Lesgourgues, *The Cosmic Linear Anisotropy Solving System (CLASS) I: Overview*, *ArXiv e-prints* (Apr., 2011) , [arxiv:1104.2932].

[36] D. Blas, J. Lesgourgues and T. Tram, *The Cosmic Linear Anisotropy Solving System (CLASS). Part II: Approximation schemes*, JCAP **2011** (Jul, 2011) 034, [1104.2933].

[37] M. Kamionkowski and E. D. Kovetz, *The Quest for B Modes from Inflationary Gravitational Waves*, *Annual Review of Astronomy and Astrophysics* **54** (Sep, 2016) 227–269, [1510.06042].

[38] L. McAllister, E. Silverstein and A. Westphal, *Gravity waves and linear inflation from axion monodromy*, *Phys. Rev. D* **82** (Aug, 2010) 046003.

[39] E. Silverstein and A. Westphal, *Monodromy in the CMB: Gravity waves and string inflation*, *Phys. Rev. D* **78** (Nov, 2008) 106003, [0803.3085].

[40] A. A. Starobinsky, *A New Type of Isotropic Cosmological Models Without Singularity*, *Phys. Lett.* **B91** (1980) 99–102.

[41] V. F. Mukhanov and G. V. Chibisov, *Quantum fluctuations and a nonsingular universe*, *ZhETF Pisma Redaktsiiu* **33** (May, 1981) 549–553.

[42] S. P. Boughn and R. G. Crittenden, *A detection of the integrated Sachs Wolfe effect*, *New Astronomy Reviews* **49** (May, 2005) 75–78, [astro-ph/0404470].

[43] M. J. Rees and D. W. Sciama, *Large-scale Density Inhomogeneities in the Universe*, *Nature* **217** (Feb., 1968) 511–516.

[44] U. Seljak, *Rees-Sciama effect in a CDM universe*, *Astrophys. J.* **460** (1996) 549, [`astro-ph/9506048`].

[45] R. Tuluie, P. Laguna and P. Anninos, *Cosmic Microwave Background Anisotropies from the Rees-Sciama Effect in* $\Omega_0 \leq 1$ *Universes*, *ApJ* **463** (May, 1996) 15, [`astro-ph/9510019`].

[46] A. Lewis and A. Challinor, *Weak gravitational lensing of the CMB*, *Physics Reports* **429** (June, 2006) 1–65, [`astro-ph/0601594`].

[47] D. Hanson, A. Challinor and A. Lewis, *Weak lensing of the CMB*, *General Relativity and Gravitation* **42** (Sep, 2010) 2197–2218, [`0911.0612`].

[48] W. Hu and T. Okamoto, *Mass Reconstruction with Cosmic Microwave Background Polarization*, *ApJ* **574** (Aug., 2002) 566–574, [`astro-ph/0111606`].

[49] M. Kesden, A. Cooray and M. Kamionkowski, *Lensing reconstruction with CMB temperature and polarization*, *Phys. Rev. D* **67** (Jun, 2003) 123507, [`astro-ph/0302536`].

[50] A. Cooray and M. Kesden, *Weak lensing of the CMB: extraction of lensing information from the trispectrum*, *New Astron.* **8** (Mar, 2003) 231–253, [`astro-ph/0204068`].

[51] CMB-Bharat: An Indian Cosmology Consortium, ““Exploring Cosmic History and Origin: A proposal for a next generation space mission for near-ultimate measurements of the Cosmic Microwave Background (CMB) polarization and discovery of global CMB spectral distortions”.” `http://cmb-bharat.in/wp-content/uploads/2018/06/cmb-bharat-rao-tp-es.pdf`, 2018.

[52] B. M. Sutin, M. Alvarez, N. Battaglia, J. Bock, M. Bonato, J. Borrill et al., *PICO - the probe of inflation and cosmic origins*, in *Space Telescopes and Instrumentation 2018: Optical, Infrared, and Millimeter Wave*, vol. 10698 of *Society of Photo-Optical Instrumentation Engineers (SPIE) Conference Series*, p. 106984F, Jul, 2018, `1808.01368`, DOI.

[53] The Simons Observatory Collaboration, P. Ade, J. Aguirre, Z. Ahmed, S. Aiola, A. Ali et al., *The Simons Observatory: Science goals and forecasts*, *ArXiv e-prints* (Aug., 2018) , [`1808.07445`].

[54] K. N. Abazajian, P. Adshead, Z. Ahmed, S. W. Allen, D. Alonso, K. S. Arnold et al., *CMB-S4 Science Book, First Edition*, *ArXiv e-prints* (Oct., 2016) , [`arxiv:1610.02743`].

[55] J. P. Ostriker and E. T. Vishniac, *Generation of microwave background fluctuations from nonlinear perturbations at the ERA of galaxy formation*, *ApJL* **306** (July, 1986) L51–L54.

[56] A. H. Jaffe and M. Kamionkowski, *Calculation of the Ostriker-Vishniac effect in cold dark matter models*, *Phys. Rev.* **D58** (1998) 043001, [`astro-ph/9801022`].

[57] Y. Rephaeli, *Comptonization Of The Cosmic Microwave Background: The Sunyaev-Zeldovich Effect*, *Annual Review of Astronomy and Astrophysics* **33** (1995) 541–580.

[58] R. A. Sunyaev and Y. B. Zeldovich, *Small-Scale Fluctuations of Relic Radiation*, *Astrophysics and Space Science* **7** (Apr., 1970) 3–19.

[59] R. A. Sunyaev and Y. B. Zeldovich, *The Observations of Relic Radiation as a Test of the Nature of X-Ray Radiation from the Clusters of Galaxies*, *Comments on Astrophysics and Space Physics* **4** (Nov., 1972) 173.

[60] R. A. Sunyaev and I. B. Zeldovich, *The velocity of clusters of galaxies relative to the microwave background - The possibility of its measurement*, *MNRAS* **190** (Feb., 1980) 413–420.

[61] J. Chluba, D. Nagai, S. Sazonov and K. Nelson, *A fast and accurate method for computing the Sunyaev-Zel'dovich signal of hot galaxy clusters*, *MNRAS* **426** (Oct, 2012) 510–530, [`1205.5778`].

[62] E. Audit and J. F. L. Simmons, *The kinematic Sunyaev-Zel'dovich effect and transverse cluster velocities*, *MNRAS* **305** (May, 1999) L27–L30, [`astro-ph/9812310`].

[63] J. E. Carlstrom, G. P. Holder and E. D. Reese, *Cosmology with the Sunyaev-Zel'dovich Effect*, *Annual Review of Astronomy and Astrophysics* **40** (Jan, 2002) 643–680, [`astro-ph/0208192`].

[64] Y. Rephaeli and O. Lahav, *Peculiar Cluster Velocities from Measurements of the Kinematic Sunyaev-Zeldovich Effect*, *ApJ* **372** (May, 1991) 21.

[65] C.-P. Ma and J. N. Fry, *Nonlinear Kinetic Sunyaev-Zeldovich Effect*, *Phys. Rev. Lett.* **88** (May, 2002) 211301, [`astro-ph/0106342`].

[66] K. M. Smith and S. Ferraro, *Detecting Patchy Reionization in the Cosmic Microwave Background*, *Phys. Rev. Lett.* **119** (2017) 021301, [`arxiv:1607.01769`].

[67] N. Hand, G. E. Addison, E. Aubourg, N. Battaglia, E. S. Battistelli, D. Bizyaev et al., *Evidence of Galaxy Cluster Motions with the Kinematic Sunyaev-Zel'dovich Effect*, *Phys. Rev. Lett.* **109** (Jul, 2012) 041101, [`1203.4219`].

[68] S. Bhattacharya and A. Kosowsky, *Dark energy constraints from galaxy cluster peculiar velocities*, *Phys. Rev. D* **77** (Apr, 2008) 083004, [`0712.0034`].

[69] U. Alam, Z. Lukić and S. Bhattacharya, *Galaxy Clusters as a Probe of Early Dark Energy*, *ApJ* **727** (Feb, 2011) 87, [`1004.0437`].

[70] E.-M. Mueller, F. de Bernardis, R. Bean and M. D. Niemack, *Constraints on Gravity and Dark Energy from the Pairwise Kinematic Sunyaev-Zel'dovich Effect*, *ApJ* **808** (July, 2015) 47, [`1408.6248`].

[71] G. J. Stacey, M. Aravena, K. Basu, N. Battaglia, B. Beringue, F. Bertoldi et al., *CCAT-Prime: science with an ultra-widefield submillimeter observatory on Cerro Chajnantor*, in *Proceedings of the SPIE*, vol. 10700 of *Society of Photo-Optical Instrumentation Engineers (SPIE) Conference Series*, p. 107001M, Jul, 2018, `1807.04354`, DOI.

[72] M. Birkinshaw, *The Sunyaev-Zel'dovich effect*, *Physics Reports* **310** (Mar, 1999) 97–195, [`astro-ph/9808050`].

[73] A. Stebbins, *Extensions to the Kompaneets Equation and Sunyaev-Zel'dovich Distortion*, *arXiv e-prints* (Sep, 1997) astro–ph/9709065, [`astro-ph/9709065`].

[74] B. A. Benson, P. A. R. Ade, Z. Ahmed, S. W. Allen, K. Arnold, J. E. Austermann et al., *SPT-3G: a next-generation cosmic microwave background polarization experiment on the South Pole telescope*, in *Millimeter, Submillimeter, and Far-Infrared Detectors and Instrumentation for Astronomy VII*, vol. 9153 of *Proceedings of the SPIE*, p. 91531P, July, 2014, `1407.2973`, DOI.

[75] T. Louis, E. Grace, M. Hasselfield, M. Lungu, L. Maurin, G. E. Addison et al., *The Atacama Cosmology Telescope: two-season ACTPol spectra and parameters*, JCAP **6** (June, 2017) 031, [`1610.02360`].

[76] A. Mittal, F. de Bernardis and M. D. Niemack, *Optimizing measurements of cluster velocities and temperatures for CCAT-prime and future surveys*, JCAP **2018** (Feb, 2018) 032, [`1708.06365`].

[77] A. Challinor and A. Lasenby, *Relativistic Corrections to the Sunyaev-Zeldovich Effect*, *ApJ* **499** (May, 1998) 1–6, [`astro-ph/9711161`].

[78] T. A. Ensslin and S. H. Hansen, *Searching for the relativistic Sunyaev-Zeldovich effect with the PLANCK experiment*, *Submitted to: Astron. Astrophys.* (2004) , [`astro-ph/0401337`].

[79] M. Shimon and Y. Rephaeli, *Quantitative description of the Sunyaev-Zeldovich effect: analytic approximations*, *New Astron.* **9** (Jan, 2004) 69–82, [`astro-ph/0309098`].

[80] N. Itoh, S. Nozawa and Y. Kohyama, *Relativistic Corrections to the Sunyaev-Zeldovich Effect for Clusters of Galaxies. III. Polarization Effect*, *ApJ* **533** (Apr., 2000) 588–593, [`astro-ph/9812376`].

[81] S. M. Molnar and M. Birkinshaw, *Inverse Compton Scattering in Mildly Relativistic Plasma*, *ApJ* **523** (Sep, 1999) 78–86, [`astro-ph/9903444`].

[82] J. C. Hill, N. Battaglia, J. Chluba, S. Ferraro, E. Schaan and D. N. Spergel, *Taking the Universe's Temperature with Spectral Distortions of the Cosmic Microwave Background*, *Physical Review Letters* **115** (Dec., 2015) 261301, [`1507.01583`].

[83] N. Aghanim, S. Majumdar and J. Silk, *Secondary anisotropies of the CMB*, *Reports on Progress in Physics* **71** (Jun, 2008) 066902, [`0711.0518`].

[84] W. Hu, D. Scott and J. Silk, *Power Spectrum Constraints from Spectral Distortions in the Cosmic Microwave Background*, *ApJL* **430** (Jul, 1994) L5, [`astro-ph/9402045`].

[85] P. Ade, J. Aguirre, Z. Ahmed, S. Aiola, A. Ali, D. Alonso et al., *The Simons Observatory: science goals and forecasts*, *Journal of Cosmology and Astro-Particle Physics* **2019** (Feb, 2019) 056, [`1808.07445`].

[86] B. Thorne, J. Dunkley, D. Alonso and S. Næss, *The Python Sky Model: software for simulating the Galactic microwave sky*, *MNRAS* **469** (Aug., 2017) 2821–2833, [`1608.02841`].

[87] Planck Collaboration, Y. Akrami, F. Arroja, M. Ashdown, J. Aumont, C. Baccigalupi et al., *Planck 2018 results. I. Overview and the cosmological legacy of Planck*, *arXiv e-prints* (Jul, 2018) arXiv:1807.06205, [`1807.06205`].

[88] R. Stompor, S. Leach, F. Stivoli and C. Baccigalupi, *Maximum likelihood algorithm for parametric component separation in cosmic microwave background experiments*, *MNRAS* **392** (Jan, 2009) 216–232, [`0804.2645`].

[89] F. Stivoli, J. Grain, S. M. Leach, M. Tristram, C. Baccigalupi and R. Stompor, *Maximum likelihood, parametric component separation and CMB B-mode detection in suborbital experiments*, *MNRAS* **408** (Nov, 2010) 2319–2335, [`1004.4756`].

[90] J. Errard and R. Stompor, *Astrophysical foregrounds and primordial tensor-to-scalar ratio constraints from CMB B-mode polarization observations*, *Phys. Rev.* **D85** (2012) 083006, [`1203.5285`].

[91] Planck Collaboration, Y. Akrami, M. Ashdown, J. Aumont, C. Baccigalupi, M. Ballardini et al., *Planck 2018 results. IV. Diffuse component separation*, *arXiv e-prints* (Jul, 2018) arXiv:1807.06208, [`1807.06208`].

[92] J. Errard, S. M. Feeney, H. V. Peiris and A. H. Jaffe, *Robust forecasts on fundamental physics from the foreground-obscured, gravitationally-lensed CMB polarization*, JCAP **2016** (Mar, 2016) 052, [1509.06770].

[93] G. Hinshaw, D. Larson, E. Komatsu, D. N. Spergel, C. L. Bennett, J. Dunkley et al., *Nine-year Wilkinson Microwave Anisotropy Probe (WMAP) Observations: Cosmological Parameter Results*, *ApJS* **208** (Oct., 2013) 19, [1212.5226].

[94] ACTPOL collaboration, T. Louis et al., *The Atacama Cosmology Telescope: Two-Season ACTPol Spectra and Parameters*, *JCAP* **1706** (2017) 031, [1610.02360].

[95] J. E. Austermann, K. A. Aird, J. A. Beall, D. Becker, A. Bender, B. A. Benson et al., *SPTpol: an instrument for CMB polarization measurements with the South Pole Telescope*, in *Millimeter, Submillimeter, and Far-Infrared Detectors and Instrumentation for Astronomy VI*, vol. 8452 of *Society of Photo-Optical Instrumentation Engineers (SPIE) Conference Series*, p. 84521E, Sep, 2012, 1210.4970, DOI.

[96] Z. Ahmed, M. Amiri, S. J. Benton, J. J. Bock, R. Bowens-Rubin, I. Buder et al., *BICEP3: a 95GHz refracting telescope for degree-scale CMB polarization*, in *Millimeter, Submillimeter, and Far-Infrared Detectors and Instrumentation for Astronomy VII*, vol. 9153 of *Proceedings of the SPIE*, p. 91531N, Aug., 2014, 1407.5928, DOI.

[97] BICEP2 Collaboration, P. A. R. Ade, R. W. Aikin, D. Barkats, S. J. Benton, C. A. Bischoff et al., *Detection of B-Mode Polarization at Degree Angular Scales by BICEP2*, *Physical Review Letters* **112** (June, 2014) 241101, [1403.3985].

[98] BICEP2 Collaboration, Keck Array Collaboration, P. A. R. Ade, Z. Ahmed, R. W. Aikin, K. D. Alexand er et al., *Constraints on Primordial Gravitational Waves Using Planck, WMAP, and New BICEP2/Keck Observations through the 2015 Season*, *Phys. Rev. Lett.* **121** (Nov, 2018) 221301, [1810.05216].

[99] R. Keisler, S. Hoover, N. Harrington, J. W. Henning, P. A. R. Ade, K. A. Aird et al., *Measurements of Sub-degree B-mode Polarization in the Cosmic Microwave Background from 100 Square Degrees of SPTpol Data*, *ApJ* **807** (July, 2015) 151, [1503.02315].

[100] POLARBEAR Collaboration, P. A. R. Ade, M. Aguilar, Y. Akiba, K. Arnold, C. Baccigalupi et al., *A Measurement of the Cosmic Microwave Background B-mode Polarization Power Spectrum at Subdegree Scales from Two Years of polarbear Data*, *The Astrophysical Journal* **848** (Oct, 2017) 121, [1705.02907].

[101] The Simons Observatory Collaboration, M. H. Abitbol, S. Adachi, P. Ade, J. Aguirre, Z. Ahmed et al., *The Simons Observatory: Astro2020 Decadal Project Whitepaper*, *arXiv e-prints* (Jul, 2019) arXiv:1907.08284, [1907.08284].

[102] N. Galitzki, A. Ali, K. S. Arnold, P. C. Ashton, J. E. Austermann, C. Baccigalupi et al., *The Simons Observatory: instrument overview*, in *Proceedings of the SPIE*, vol. 10708 of *Society of Photo-Optical Instrumentation Engineers (SPIE) Conference Series*, p. 1070804, Jul, 2018, `1808.04493`, DOI.

[103] DESI Collaboration, A. Aghamousa, J. Aguilar, S. Ahlen, S. Alam, L. E. Allen et al., *The DESI Experiment Part I: Science,Targeting, and Survey Design*, *arXiv e-prints* (Oct, 2016) arXiv:1611.00036, [`1611.00036`].

[104] M. Hazumi et al., *LiteBIRD: A Satellite for the Studies of B-Mode Polarization and Inflation from Cosmic Background Radiation Detection*, *J. Low. Temp. Phys.* **194** (2019) 443–452.

[105] G. Hinshaw, D. Larson, E. Komatsu, D. N. Spergel, C. L. Bennett, J. Dunkley et al., *Nine-year Wilkinson Microwave Anisotropy Probe (WMAP) Observations: Cosmological Parameter Results*, *ApJS* **208** (Oct., 2013) 19, [`1212.5226`].

[106] Planck Collaboration, R. Adam, N. Aghanim, M. Ashdown, J. Aumont, C. Baccigalupi et al., *Planck intermediate results. XLVII. Planck constraints on reionization history*, *A&A* **596** (Dec., 2016) A108, [`1605.03507`].

[107] A. Roy, A. Lapi, D. Spergel and C. Baccigalupi, *Observing patchy reionization with future CMB polarization experiments*, JCAP **5** (May, 2018) 014, [`1801.02393`].

[108] The Polarbear Collaboration: P. A. R. Ade, Y. Akiba, A. E. Anthony, K. Arnold, M. Atlas, D. Barron et al., *A Measurement of the Cosmic Microwave Background B-mode Polarization Power Spectrum at Sub-degree Scales with POLARBEAR*, *ApJ* **794** (Oct., 2014) 171, [`1403.2369`].

[109] A. Suzuki, P. Ade, Y. Akiba, C. Aleman, K. Arnold, C. Baccigalupi et al., *The Polarbear-2 and the Simons Array Experiments*, *Journal of Low Temperature Physics* **184** (Aug., 2016) 805–810, [`1512.07299`].

[110] J. P. Filippini, P. A. R. Ade, M. Amiri, S. J. Benton, R. Bihary, J. J. Bock et al., *SPIDER: a balloon-borne CMB polarimeter for large angular scales*, in *Millimeter, Submillimeter, and Far-Infrared Detectors and Instrumentation for Astronomy V*, vol. 7741 of *Proceedings of the SPIE*, p. 77411N, July, 2010, `1106.2158`, DOI.

[111] B. Reichborn-Kjennerud, A. M. Aboobaker, P. Ade, F. Aubin, C. Baccigalupi, C. Bao et al., *EBEX: a balloon-borne CMB polarization experiment*, in *Millimeter, Submillimeter, and Far-Infrared Detectors and Instrumentation for Astronomy V*, vol. 7741 of *Proceedings of the SPIE*, p. 77411C, July, 2010, `1007.3672`, DOI.

[112] X. Fan, M. A. Strauss, R. H. Becker, R. L. White, J. E. Gunn, G. R. Knapp et al., *Constraining the Evolution of the Ionizing Background and the Epoch of Reionization with z˜6 Quasars. II. A Sample of 19 Quasars*, *AJ* **132** (July, 2006) 117–136, [`astro-ph/0512082`].

[113] G. D. Becker, J. S. Bolton and A. Lidz, *Reionisation and High-Redshift Galaxies: The View from Quasar Absorption Lines*, *Publications of the Astronomical Society of Australia* **32** (Dec., 2015) e045, [1510.03368].

[114] D. J. Mortlock, S. J. Warren, B. P. Venemans, M. Patel, P. C. Hewett, R. G. McMahon et al., *A luminous quasar at a redshift of $z = 7.085$*, *Nature* **474** (June, 2011) 616–619, [1106.6088].

[115] R. Chornock, E. Berger, D. B. Fox, R. Lunnan, M. R. Drout, W.-f. Fong et al., *GRB 130606A as a Probe of the Intergalactic Medium and the Interstellar Medium in a Star-forming Galaxy in the First Gyr after the Big Bang*, *ApJ* **774** (Sept., 2013) 26, [1306.3949].

[116] T. Totani, K. Aoki, T. Hattori, G. Kosugi, Y. Niino, T. Hashimoto et al., *Probing intergalactic neutral hydrogen by the Lyman alpha red damping wing of gamma-ray burst 130606A afterglow spectrum at $z = 5.913$*, *Publications of the Astronomical Society of Japan* **66** (June, 2014) 63, [1312.3934].

[117] R. Barkana and A. Loeb, *In the beginning: the first sources of light and the reionization of the universe*, *Physics Reports* **349** (July, 2001) 125–238, [astro-ph/0010468].

[118] B. E. Robertson, R. S. Ellis, J. S. Dunlop, R. J. McLure and D. P. Stark, *Early star-forming galaxies and the reionization of the Universe*, *Nature* **468** (Nov., 2010) 49–55, [1011.0727].

[119] A. Lapi, C. Mancuso, A. Celotti and L. Danese, *Galaxy Evolution at High Redshift: Obscured Star Formation, GRB Rates, Cosmic Reionization, and Missing Satellites*, *ApJ* **835** (Jan., 2017) 37, [1612.01304].

[120] S. R. Furlanetto and S. P. Oh, *Taxing the rich: recombinations and bubble growth during reionization*, *MNRAS* **363** (Nov., 2005) 1031–1048, [astro-ph/0505065].

[121] A. Lidz, S. P. Oh and S. R. Furlanetto, *Have We Detected Patchy Reionization in Quasar Spectra?*, *ApJL* **639** (Mar., 2006) L47–L50, [astro-ph/0512427].

[122] S. R. Furlanetto and A. Loeb, *Is Double Reionization Physically Plausible?*, *ApJ* **634** (Nov., 2005) 1–13, [astro-ph/0409656].

[123] A. Paranjape and T. R. Choudhury, *An improved model of H II bubbles during the epoch of reionization*, *MNRAS* **442** (Aug., 2014) 1470–1482, [1401.7994].

[124] A. Natarajan, N. Battaglia, H. Trac, U.-L. Pen and A. Loeb, *Reionization on Large Scales. II. Detecting Patchy Reionization through Cross-correlation of the Cosmic Microwave Background*, *ApJ* **776** (Oct., 2013) 82, [1211.2822].

[125] I. T. Iliev, U.-L. Pen, J. Richard Bond, G. Mellema and P. R. Shapiro, *kSZ from patchy reionization: The view from the simulations*, *New Astronomy Reviews* **50** (Dec., 2006) 909–917, [`astro-ph/0607209`].

[126] T. Namikawa, *Constraints on patchy reionization from Planck CMB temperature trispectrum*, *Phys. Rev. D* **97** (Mar., 2018) 063505, [`1711.00058`].

[127] C. Dvorkin and K. M. Smith, *Reconstructing patchy reionization from the cosmic microwave background*, *Phys. Rev. D* **79** (Feb., 2009) 043003, [`arxiv:0812.1566`].

[128] Planck Collaboration, P. A. R. Ade, N. Aghanim, M. Arnaud, M. Ashdown, J. Aumont et al., *Planck 2015 results. XIII. Cosmological parameters*, *A&A* **594** (Sept., 2016) A13, [`arxiv:1502.01589`].

[129] C. Mancuso, A. Lapi, J. Shi, J. Gonzalez-Nuevo, R. Aversa and L. Danese, *The Quest for Dusty Star-forming Galaxies at High Redshift* $z \gtrsim 4$, *ApJ* **823** (June, 2016) 128, [`arxiv:1604.02507`].

[130] C. Mancuso, A. Lapi, J. Shi, Z.-Y. Cai, J. Gonzalez-Nuevo, M. Béthermin et al., *The Main Sequences of Star-forming Galaxies and Active Galactic Nuclei at High Redshift*, *ApJ* **833** (Dec., 2016) 152, [`arxiv:1610.05910`].

[131] G. R. Meurer, T. M. Heckman and D. Calzetti, *Dust Absorption and the Ultraviolet Luminosity Density at z ˜ 3 as Calibrated by Local Starburst Galaxies*, *ApJ* **521** (Aug., 1999) 64–80, [`astro-ph/9903054`].

[132] R. J. Bouwens, G. D. Illingworth, M. Franx, R.-R. Chary, G. R. Meurer, C. J. Conselice et al., *UV Continuum Slope and Dust Obscuration from* $z \sim 6$ *to* $z \sim 2$*: The Star Formation Rate Density at High Redshift*, *ApJ* **705** (Nov., 2009) 936–961, [`arxiv:0909.4074`].

[133] R. J. Bouwens et al., *UV Luminosity Functions at redshifts z ∼4 to z ∼10: 10000 Galaxies from HST Legacy Fields*, *Astrophys. J.* **803** (2015) 34, [`1403.4295`].

[134] R. J. Bouwens, M. Aravena, R. Decarli, F. Walter, E. da Cunha, I. Labbé et al., *ALMA Spectroscopic Survey in the Hubble Ultra Deep Field: The Infrared Excess of UV-Selected z = 2-10 Galaxies as a Function of UV-Continuum Slope and Stellar Mass*, *ApJ* **833** (Dec., 2016) 72, [`arxiv:1606.05280`].

[135] R. J. Bouwens, P. A. Oesch, G. D. Illingworth, R. S. Ellis and M. Stefanon, *The* $z \sim 6$ *luminosity function fainter than -15 mag from the hubble frontier fields: The impact of magnification uncertainties*, *The Astrophysical Journal* **843** (jul, 2017) 129.

[136] L. Silva, G. L. Granato, A. Bressan and L. Danese, *Modeling the Effects of Dust on Galactic Spectral Energy Distributions from the Ultraviolet to the Millimeter Band*, *ApJ* **509** (Dec., 1998) 103–117.

[137] A. Efstathiou, M. Rowan-Robinson and R. Siebenmorgen, *Massive star formation in galaxies: radiative transfer models of the UV to millimetre emission of starburst galaxies*, *MNRAS* **313** (Apr., 2000) 734–744, [`astro-ph/9912252`].

[138] K. E. K. Coppin, J. E. Geach, O. Almaini, V. Arumugam, J. S. Dunlop, W. G. Hartley et al., *The SCUBA-2 Cosmology Legacy Survey: the submillimetre properties of Lyman-break galaxies at $z = 3$-5*, *MNRAS* **446** (Jan., 2015) 1293–1304, [`arxiv:1407.6712`].

[139] N. A. Reddy, M. Kriek, A. E. Shapley, W. R. Freeman, B. Siana, A. L. Coil et al., *THE MOSDEF SURVEY: MEASUREMENTS OF BALMER DECREMENTS AND THE DUST ATTENUATION CURVE AT REDSHIFTS$z\sim$ 1.4–2.6*, *The Astrophysical Journal* **806** (jun, 2015) 259.

[140] Y. Fudamoto, P. A. Oesch, E. Schinnerer, B. Groves, A. Karim, B. Magnelli et al., *The Dust Attenuation of Star-forming Galaxies at $z \sim 3$ and Beyond: New Insights from ALMA Observations*, *ArXiv e-prints* (May, 2017) , [`arxiv:1705.01559`].

[141] M. Novak, V. Smolčić, J. Delhaize, I. Delvecchio, G. Zamorani, N. Baran et al., *The VLA-COSMOS 3 GHz Large Project: Cosmic star formation history since z 5*, *A&A* **602** (June, 2017) A5, [`arxiv:1703.09724`].

[142] D. A. Riechers, T. K. D. Leung, R. J. Ivison, I. Perez-Fournon, A. J. R. Lewis, R. Marques-Chaves et al., *Rise of the Titans: A Dusty, Hyper-Luminous "870 micron Riser" Galaxy at z˜6*, *ArXiv e-prints* (May, 2017) , [`arxiv:1705.09660`].

[143] J. A. Zavala, A. Montaña, D. H. Hughes, M. S. Yun, R. J. Ivison, E. Valiante et al., *An amplified dusty star-forming galaxy at $z = 6$: unveiling an elusive population of galaxies*, *ArXiv e-prints* (July, 2017) , [`arxiv:1707.09022`].

[144] A. Bressan, L. Silva and G. L. Granato, *Far infrared and radio emission in dusty starburst galaxies*, *A&A* **392** (Sept., 2002) 377–391, [`astro-ph/0206029`].

[145] R. C. Kennicutt and N. J. Evans, *Star Formation in the Milky Way and Nearby Galaxies*, *Annual Review of Astronomy and Astrophysics* **50** (Sept., 2012) 531–608, [`arxiv:1204.3552`].

[146] C. Mancuso, A. Lapi, I. Prandoni, I. Obi, J. Gonzalez-Nuevo, F. Perrotta et al., *Galaxy Evolution in the Radio Band: The Role of Star-forming Galaxies and Active Galactic Nuclei*, *ApJ* **842** (June, 2017) 95, [`arxiv:1705.06539`].

[147] A. Alavi, B. Siana, J. Richard, D. P. Stark, C. Scarlata, H. I. Teplitz et al., *Ultra-faint Ultraviolet Galaxies at z ˜ 2 behind the Lensing Cluster A1689: The Luminosity Function, Dust Extinction, and Star Formation Rate Density*, *ApJ* **780** (Jan., 2014) 143, [`arxiv:1305.2413`].

[148] A. Alavi, B. Siana, J. Richard, M. Rafelski, M. Jauzac, M. Limousin et al., *THE EVOLUTION OF THE FAINT END OF THE UV LUMINOSITY FUNCTION DURING THE PEAK EPOCH OF STAR FORMATION $(1\lt z\lt 3)$*, *The Astrophysical Journal* **832** (nov, 2016) 56.

[149] R. C. Livermore, S. L. Finkelstein and J. M. Lotz, *Directly Observing the Galaxies Likely Responsible for Reionization*, *ApJ* **835** (Feb., 2017) 113, [`arxiv:1604.06799`].

[150] P. Madau and M. Dickinson, *Cosmic Star-Formation History*, *Annual Review of Astronomy and Astrophysics* **52** (Aug., 2014) 415–486, [`arxiv:1403.0007`].

[151] D. Schiminovich, O. Ilbert, S. Arnouts, B. Milliard, L. Tresse, O. Le Fèvre et al., *The GALEX-VVDS Measurement of the Evolution of the Far-Ultraviolet Luminosity Density and the Cosmic Star Formation Rate*, *ApJL* **619** (Jan., 2005) L47–L50, [`astro-ph/0411424`].

[152] A. M. Hopkins and J. F. Beacom, *On the Normalization of the Cosmic Star Formation History*, *ApJ* **651** (Nov., 2006) 142–154, [`astro-ph/0601463`].

[153] B. Magnelli, P. Popesso, S. Berta, F. Pozzi, D. Elbaz, D. Lutz et al., *The deepest Herschel-PACS far-infrared survey: number counts and infrared luminosity functions from combined PEP/GOODS-H observations*, *A&A* **553** (May, 2013) A132, [`arxiv:1303.4436`].

[154] C. Gruppioni, F. Pozzi, G. Rodighiero, I. Delvecchio, S. Berta, L. Pozzetti et al., *The Herschel PEP/HerMES Luminosity Function. I: Probing the Evolution of PACS selected Galaxies to $z \sim 4$*, *MNRAS* **432** (June, 2013) 23–52, [`arxiv:1302.5209`].

[155] D. Liu, E. Daddi, M. Dickinson, F. Owen, M. Pannella, M. Sargent et al., *"Super-deblended" Dust Emission in Galaxies: I. the GOODS-North Catalog and the Cosmic Star Formation Rate Density out to Redshift 6*, *ArXiv e-prints* (Mar., 2017) , [`1703.05281`].

[156] M. Rowan-Robinson, S. Oliver, L. Wang, D. Farrah, D. L. Clements, C. Gruppioni et al., *The star formation rate density from $z = 1$ to 6*, *MNRAS* **461** (Sept., 2016) 1100–1111, [`arxiv:1605.03937`].

[157] M. D. Kistler, H. Yüksel, J. F. Beacom, A. M. Hopkins and J. S. B. Wyithe, *The Star Formation Rate in the Reionization Era as Indicated by Gamma-Ray Bursts*, *ApJL* **705** (Nov., 2009) L104–L108, [`arxiv:0906.0590`].

[158] M. D. Kistler, H. Yuksel and A. M. Hopkins, *The Cosmic Star Formation Rate from the Faintest Galaxies in the Unobservable Universe*, *ArXiv e-prints* (May, 2013) , [`arxiv:1305.1630`].

[159] Planck Collaboration, R. Adam, N. Aghanim, M. Ashdown, J. Aumont, C. Baccigalupi et al., *Planck intermediate results. XLVII. Planck constraints on reionization history*, *A&A* **596** (Dec., 2016) A108, [`arxiv:1605.03507`].

[160] R. F. J. van der Burg, H. Hildebrandt and T. Erben, *The UV galaxy luminosity function at z = 3-5 from the CFHT Legacy Survey Deep fields*, *A&A* **523** (Nov., 2010) A74, [`arxiv:1009.0758`].

[161] S. L. Finkelstein, R. E. Ryan, Jr., C. Papovich, M. Dickinson, M. Song, R. S. Somerville et al., *The Evolution of the Galaxy Rest-frame Ultraviolet Luminosity Function over the First Two Billion Years*, *ApJ* **810** (Sept., 2015) 71, [`arxiv:1410.5439`].

[162] O. Cucciati, L. Tresse, O. Ilbert, O. Le Fèvre, B. Garilli, V. Le Brun et al., *The star formation rate density and dust attenuation evolution over 12 Gyr with the VVDS surveys*, *A&A* **539** (Mar., 2012) A31, [`arxiv:1109.1005`].

[163] T. K. Wyder, M. A. Treyer, B. Milliard, D. Schiminovich, S. Arnouts, T. Budavári et al., *The Ultraviolet Galaxy Luminosity Function in the Local Universe from GALEX Data*, *ApJL* **619** (Jan., 2005) L15–L18, [`astro-ph/0411364`].

[164] P. A. Oesch, R. J. Bouwens, C. M. Carollo, G. D. Illingworth, D. Magee, M. Trenti et al., *The Evolution of the Ultraviolet Luminosity Function from z ˜ 0.75 to z ˜ 2.5 Using HST ERS WFC3/UVIS Observations*, *ApJL* **725** (Dec., 2010) L150–L155, [`arxiv:1005.1661`].

[165] C. Gruppioni, F. Calura, F. Pozzi, I. Delvecchio, S. Berta, G. De Lucia et al., *Star formation in Herschel's Monsters versus semi-analytic models*, *MNRAS* **451** (Aug., 2015) 3419–3426, [`arxiv:1506.01518`].

[166] A. Cooray, J. Calanog, J. L. Wardlow, J. Bock, C. Bridge, D. Burgarella et al., *HerMES: The Rest-frame UV Emission and a Lensing Model for the z = 6.34 Luminous Dusty Starburst Galaxy HFLS3*, *ApJ* **790** (July, 2014) 40, [`arxiv:1404.1378`].

[167] J. Mao, A. Lapi, G. L. Granato, G. de Zotti and L. Danese, *The Role of the Dust in Primeval Galaxies: A Simple Physical Model for Lyman Break Galaxies and Lyα Emitters*, *ApJ* **667** (Oct., 2007) 655–666, [`astro-ph/0611799`].

[168] J. S. Dunlop, A. B. Rogers, R. J. McLure, R. S. Ellis, B. E. Robertson, A. Koekemoer et al., *The UV continua and inferred stellar populations of galaxies at $z\sim$ 7-9 revealed by the Hubble Ultra-Deep Field 2012 campaign*, *MNRAS* **432** (July, 2013) 3520–3533, [`arxiv:1212.0860`].

[169] B. E. Robertson, R. S. Ellis, S. R. Furlanetto and J. S. Dunlop, *Cosmic Reionization and Early Star-forming Galaxies: A Joint Analysis of New*

Constraints from Planck and the Hubble Space Telescope, *ApJL* **802** (Apr., 2015) L19, [`arxiv:1502.02024`].

[170] P. Madau, F. Haardt and M. J. Rees, *Radiative Transfer in a Clumpy Universe. III. The Nature of Cosmological Ionizing Sources*, *ApJ* **514** (Apr., 1999) 648–659, [`astro-ph/9809058`].

[171] A. Ferrara and S. Pandolfi, *Reionization of the Intergalactic Medium*, *ArXiv e-prints* (Sept., 2014) , [`arxiv:1409.4946`].

[172] A. H. Pawlik, M. Milosavljević and V. Bromm, *The First Galaxies: Assembly under Radiative Feedback from the First Stars*, *ApJ* **767** (Apr., 2013) 59, [`arxiv:1208.3698`].

[173] C. Schultz, J. Oñorbe, K. N. Abazajian and J. S. Bullock, *The high-z universe confronts warm dark matter: Galaxy counts, reionization and the nature of dark matter*, *MNRAS* **442** (Aug., 2014) 1597–1609, [`arxiv:1401.3769`].

[174] R. A. Sunyaev and R. Khatri, *Unavoidable CMB Spectral Features and Blackbody Photosphere of Our Universe*, *International Journal of Modern Physics D* **22** (June, 2013) 1330014, [`arxiv:1302.6553`].

[175] G. De Zotti, M. Negrello, G. Castex, A. Lapi and M. Bonato, *Another look at distortions of the Cosmic Microwave Background spectrum*, *JCAP* **1603** (2016) 047, [`arxiv:1512.04816`].

[176] T. Matsumura, Y. Akiba, J. Borrill, Y. Chinone, M. Dobbs, H. Fuke et al., *Mission Design of LiteBIRD*, *Journal of Low Temperature Physics* **176** (Sept., 2014) 733–740, [`arxiv:1311.2847`].

[177] A. Lewis, *Cosmological parameters from WMAP 5-year temperature maps*, *Phys. Rev. D* **78** (July, 2008) 023002, [`arxiv:0804.3865`].

[178] C. Dvorkin, W. Hu and K. M. Smith, *B-mode CMB polarization from patchy screening during reionization*, *Phys. Rev. D* **79** (May, 2009) 107302, [`arxiv:0902.4413`].

[179] N. Battaglia, A. Natarajan, H. Trac, R. Cen and A. Loeb, *Reionization on Large Scales. III. Predictions for Low-l Cosmic Microwave Background Polarization and High-l Kinetic Sunyaev-Zel'dovich Observables*, *ApJ* **776** (Oct., 2013) 83, [`arxiv:1211.2832`].

[180] S. Furlanetto, M. Zaldarriaga and L. Hernquist, *The Growth of HII regions during reionization*, *Astrophys. J.* **613** (2004) 1–15, [`astro-ph/0403697`].

[181] X. Wang and W. Hu, *Redshift Space 21 cm Power Spectra from Reionization*, *ApJ* **643** (June, 2006) 585, [`astro-ph/0511141`].

[182] M. Su, A. P. S. Yadav, M. McQuinn, J. Yoo and M. Zaldarriaga, *An Improved Forecast of Patchy Reionization Reconstruction with CMB*, *ArXiv e-prints* (June, 2011) , [`arxiv:1106.4313`].

[183] W. Hu, *Reionization revisited: secondary cmb anisotropies and polarization*, *Astrophys. J.* **529** (2000) 12, [`astro-ph/9907103`].

[184] M. J. Mortonson and W. Hu, *The Maximum B-mode Polarization of the Cosmic Microwave Background from Inhomogeneous Reionization*, *Astrophys. J.* **657** (2007) 1–14, [`astro-ph/0607652`].

[185] V. Gluscevic, M. Kamionkowski and A. Cooray, *Derotation of the cosmic microwave background polarization: Full-sky formalism*, *Phys. Rev. D* **80** (July, 2009) 023510, [`arxiv:0905.1687`].

[186] A. Lewis, A. Challinor and D. Hanson, *The shape of the CMB lensing bispectrum*, *JCAP* **3** (Mar., 2011) 018, [`arxiv:1101.2234`].

[187] K. M. Górski, E. Hivon, A. J. Banday, B. D. Wandelt, F. K. Hansen, M. Reinecke et al., *HEALPix: A Framework for High-Resolution Discretization and Fast Analysis of Data Distributed on the Sphere*, *ApJ* **622** (Apr., 2005) 759–771, [`astro-ph/0409513`].

[188] Planck Collaboration, R. Adam, N. Aghanim, M. Ashdown, J. Aumont, C. Baccigalupi et al., *Planck intermediate results. XLVII. Planck constraints on reionization history*, *A&A* **596** (Dec., 2016) A108, [`1605.03507`].

[189] A. H. Pawlik, J. Schaye and E. van Scherpenzeel, *Keeping the Universe ionized: photoheating and the clumping factor of the high-redshift intergalactic medium*, *MNRAS* **394** (Apr., 2009) 1812–1824, [`0807.3963`].

[190] J. M. Shull, A. Harness, M. Trenti and B. D. Smith, *Critical Star Formation Rates for Reionization: Full Reionization Occurs at Redshift z ApJ*, *ApJ* **747** (Mar., 2012) 100.

[191] K. Finlator, S. P. Oh, F. Özel and R. Davé, *Gas clumping in self-consistent reionization models*, *MNRAS* **427** (Dec., 2012) 2464–2479, [`1209.2489`].

[192] R. A. Sunyaev and I. B. Zeldovich, *Microwave background radiation as a probe of the contemporary structure and history of the universe*, *Annual Review of Astronomy and Astrophysics* **18** (1980) 537–560.

[193] C. Feng and G. Holder, *Searching for patchy reionization from cosmic microwave background with hybrid quadratic estimators*, *ArXiv e-prints* (Aug., 2018) , [`1808.01592`].

[194] Q. Ma, K. Helgason, E. Komatsu, B. Ciardi and A. Ferrara, *Measuring patchy reionization with kSZ^2-21 cm correlations*, *MNRAS* **476** (May, 2018) 4025–4031, [`1712.05305`].

[195] M. A. Alvarez, *The Kinetic Sunyaev-Zeldovich Effect from Reionization: Simulated Full-sky Maps at Arcminute Resolution*, *ApJ* **824** (June, 2016) 118, [`1511.02846`].

[196] M. A. Alvarez, E. Komatsu, O. Doré and P. R. Shapiro, *The Cosmic Reionization History as Revealed by the Cosmic Microwave Background Doppler-21 cm Correlation*, *ApJ* **647** (Aug., 2006) 840–852, [`astro-ph/0512010`].

[197] G. B. Field, *Excitation of the hydrogen 21-cm line*, *Proceedings of the IRE* **46** (Jan, 1958) 240–250.

[198] S. R. Furlanetto, S. P. Oh and F. H. Briggs, *Cosmology at low frequencies: The 21 cm transition and the high-redshift Universe*, *Physics Reports* **433** (Oct., 2006) 181–301, [`astro-ph/0608032`].

[199] P. D. Meerburg, C. Dvorkin and D. N. Spergel, *Probing Patchy Reionization through τ-21 cm Correlation Statistics*, *ApJ* **779** (Dec., 2013) 124, [`1303.3887`].

[200] G. P. Holder, I. T. Iliev and G. Mellema, *Reconstructing the Thomson Optical Depth due to Patchy Reionization with 21 cm Fluctuation Maps*, *ApJL* **663** (July, 2007) L1–L4, [`astro-ph/0609689`].

[201] X. Wang and W. Hu, *Redshift Space 21 cm Power Spectra from Reionization*, *ApJ* **643** (June, 2006) 585, [`astro-ph/0511141`].

[202] H. Tashiro, N. Aghanim, M. Langer, M. Douspis, S. Zaroubi and V. Jelic, *Detectability of the 21-cm CMB cross-correlation from the epoch of reionization*, *MNRAS* **402** (Mar., 2010) 2617–2625, [`0908.1632`].

[203] N. Battaglia, J. R. Bond, C. Pfrommer and J. L. Sievers, *On the Cluster Physics of Sunyaev-Zel'dovich and X-Ray Surveys. II. Deconstructing the Thermal SZ Power Spectrum*, *ApJ* **758** (Oct, 2012) 75, [`1109.3711`].

[204] H. Hui, P. A. R. Ade, Z. Ahmed, R. W. Aikin, K. D. Alexander, D. Barkats et al., *BICEP Array: a multi-frequency degree-scale CMB polarimeter*, in *Millimeter, Submillimeter, and Far-Infrared Detectors and Instrumentation for Astronomy IX*, vol. 10708 of *Society of Photo-Optical Instrumentation Engineers (SPIE) Conference Series*, p. 1070807, July, 2018, `1808.00568`, DOI.

[205] B. A. Benson, P. A. R. Ade, Z. Ahmed, S. W. Allen, K. Arnold, J. E. Austermann et al., *SPT-3G: a next-generation cosmic microwave background polarization experiment on the South Pole telescope*, in *Millimeter, Submillimeter, and Far-Infrared Detectors and Instrumentation for Astronomy VII*, vol. 9153 of *Proceedings of the SPIE*, p. 91531P, July, 2014, `1407.2973`, DOI.

[206] K. N. Abazajian, P. Adshead, Z. Ahmed, S. W. Allen, D. Alonso, K. S. Arnold et al., *CMB-S4 Science Book, First Edition*, *arXiv e-prints* (Oct, 2016) arXiv:1610.02743, [`1610.02743`].

[207] T. Matsumura, Y. Akiba, J. Borrill, Y. Chinone, M. Dobbs, H. Fuke et al., *Mission Design of LiteBIRD*, *Journal of Low Temperature Physics* **176** (Sep, 2014) 733–740, [`1311.2847`].

[208] T. Louis, E. Grace, M. Hasselfield, M. Lungu, L. Maurin, G. E. Addison et al., *The Atacama Cosmology Telescope: two-season ACTPol spectra and parameters*, *Journal of Cosmology and Astro-Particle Physics* **2017** (Jun, 2017) 031, [`1610.02360`].

[209] D. Hanson, S. Hoover, A. Crites, P. A. R. Ade, K. A. Aird, J. E. Austermann et al., *Detection of B-Mode Polarization in the Cosmic Microwave Background with Data from the South Pole Telescope*, *Physical Review Letters* **111** (Oct., 2013) 141301, [`1307.5830`].

[210] BICEP2 and Keck Array Collaborations, P. A. R. Ade, Z. Ahmed, R. W. Aikin, K. D. Alexander, D. Barkats et al., *BICEP2/Keck Array V: Measurements of B-mode Polarization at Degree Angular Scales and 150 GHz by the Keck Array*, *ApJ* **811** (Oct, 2015) 126, [`1502.00643`].

[211] Planck Collaboration, R. Adam, P. A. R. Ade, N. Aghanim, M. Arnaud, M. Ashdown et al., *Planck 2015 results. IX. Diffuse component separation: CMB maps*, *A&A* **594** (Sep, 2016) A9, [`1502.05956`].

[212] BICEP2/Keck Collaboration, Planck Collaboration, P. A. R. Ade, N. Aghanim, Z. Ahmed, R. W. Aikin et al., *Joint Analysis of BICEP2/Keck Array and Planck Data*, *Phys. Rev. Lett.* **114** (Mar, 2015) 101301, [`1502.00612`].

[213] Planck Collaboration, R. Adam, P. A. R. Ade, N. Aghanim, M. Arnaud, J. Aumont et al., *Planck intermediate results. XXX. The angular power spectrum of polarized dust emission at intermediate and high Galactic latitudes*, *A&A* **586** (Feb., 2016) A133, [`1409.5738`].

[214] M. Zaldarriaga and U. Seljak, *Gravitational lensing effect on cosmic microwave background polarization*, *Phys. Rev. D* **58** (July, 1998) 023003, [`astro-ph/9803150`].

[215] R. A. Sunyaev and Y. B. Zeldovich, *The Observations of Relic Radiation as a Test of the Nature of X-Ray Radiation from the Clusters of Galaxies*, *Comments on Astrophysics and Space Physics* **4** (Nov., 1972) 173.

[216] R. A. Sunyaev and I. B. Zeldovich, *Microwave background radiation as a probe of the contemporary structure and history of the universe*, *Annual Review of Astronomy and Astrophysics* **18** (1980) 537–560.

[217] N. Y. Gnedin and A. H. Jaffe, *Secondary Cosmic Microwave Background Anisotropies from Cosmological Reionization*, *ApJ* **551** (Apr., 2001) 3–14, [`astro-ph/0008469`].

[218] O. Zahn, M. Zaldarriaga, L. Hernquist and M. McQuinn, *The Influence of Nonuniform Reionization on the CMB*, *ApJ* **630** (Sept., 2005) 657–666, [`astro-ph/0503166`].

[219] P. A. R. Ade, Y. Akiba, A. E. Anthony, K. Arnold, M. Atlas, D. Barron et al., *Measurement of the Cosmic Microwave Background Polarization Lensing Power Spectrum with the POLARBEAR Experiment*, *Physical Review Letters* **113** (July, 2014) 021301, [`1312.6646`].

[220] A. van Engelen, B. D. Sherwin, N. Sehgal, G. E. Addison, R. Allison, N. Battaglia et al., *The Atacama Cosmology Telescope: Lensing of CMB Temperature and Polarization Derived from Cosmic Infrared Background Cross-correlation*, *ApJ* **808** (July, 2015) 7, [`1412.0626`].

[221] Polarbear Collaboration, P. A. R. Ade, Y. Akiba, A. E. Anthony, K. Arnold, M. Atlas et al., *A Measurement of the Cosmic Microwave Background B-mode Polarization Power Spectrum at Sub-degree Scales with POLARBEAR*, *ApJ* **794** (Oct., 2014) 171, [`1403.2369`].

[222] M. Kesden, A. Cooray and M. Kamionkowski, *Separation of Gravitational-Wave and Cosmic-Shear Contributions to Cosmic Microwave Background Polarization*, *Physical Review Letters* **89** (July, 2002) 011304, [`astro-ph/0202434`].

[223] L. Knox and Y.-S. Song, *Limit on the Detectability of the Energy Scale of Inflation*, *Physical Review Letters* **89** (July, 2002) 011303, [`astro-ph/0202286`].

[224] U. Seljak and C. M. Hirata, *Gravitational lensing as a contaminant of the gravity wave signal in the CMB*, *Phys. Rev. D* **69** (Feb., 2004) 043005, [`astro-ph/0310163`].

[225] G. Kulkarni, G. Worseck and J. F. Hennawi, *Evolution of the AGN UV luminosity function from redshift 7.5*, *arXiv e-prints* (July, 2018) , [`1807.09774`].

[226] J. Chisholm, S. Gazagnes, D. Schaerer, A. Verhamme, J. R. Rigby, M. Bayliss et al., *Accurately predicting the escape fraction of ionizing photons using restframe ultraviolet absorption lines*, *ArXiv e-prints* (Mar., 2018) , [`1803.03655`].

[227] J. Matthee, D. Sobral, M. Gronke, A. Paulino-Afonso, M. Stefanon and H. Röttgering, *Confirmation of double peaked Lyman-alpha emission at z=6.593: Witnessing a galaxy directly contributing to the reionisation of the Universe*, *ArXiv e-prints* (May, 2018) , [`1805.11621`].

[228] T. J. Fletcher, B. E. Robertson, K. Nakajima, R. S. Ellis, D. P. Stark and A. Inoue, *The Lyman Continuum Escape Survey: Ionizing Radiation from [O III]-Strong Sources at a Redshift of 3.1*, *ArXiv e-prints* (June, 2018) , [1806.01741].

[229] C. C. Steidel, M. Bogosavlevic, A. E. Shapley, N. A. Reddy, G. C. Rudie, M. Pettini et al., *The Keck Lyman Continuum Spectroscopic Survey (KLCS): The Emergent Ionizing Spectrum of Galaxies at* $z \sim 3$, *ArXiv e-prints* (May, 2018) , [1805.06071].

[230] G. Kulkarni, T. R. Choudhury, E. Puchwein and M. G. Haehnelt, *Large 21-cm signals from AGN-dominated reionization*, *MNRAS* **469** (Aug., 2017) 4283–4291, [1701.04408].

[231] G. D. Becker, J. S. Bolton, P. Madau, M. Pettini, E. V. Ryan-Weber and B. P. Venemans, *Evidence of patchy hydrogen reionization from an extreme Ly*α *trough below redshift six*, *MNRAS* **447** (Mar., 2015) 3402–3419, [1407.4850].

[232] S. E. I. Bosman, X. Fan, L. Jiang, S. Reed, Y. Matsuoka, G. Becker et al., *New constraints on Lyman-*α *opacity with a sample of 62 quasars at* $z > 5.7$, *MNRAS* (May, 2018) , [1802.08177].

[233] A.-C. Eilers, F. B. Davies and J. F. Hennawi, *The Opacity of the Intergalactic Medium Measured Along Quasar Sightlines at* $z \sim 6$, *Astrophys. J.* **864** (2018) 53, [1807.04229].

[234] G. D. Becker, F. B. Davies, S. R. Furlanetto, M. A. Malkan, E. Boera and C. Douglass, *Evidence for Large-scale Fluctuations in the Metagalactic Ionizing Background Near Redshift Six*, *ApJ* **863** (Aug., 2018) 92, [1803.08932].

[235] G. Kulkarni, L. C. Keating, M. G. Haehnelt, S. E. I. Bosman, E. Puchwein, J. Chardin et al., *Large Ly* α *opacity fluctuations and low CMB* τ *in models of late reionization with large islands of neutral hydrogen extending to* $z < 5.5$, *MNRAS* **485** (May, 2019) L24–L28, [1809.06374].

[236] Planck Collaboration XVI, *Planck 2013 results. XVI. Cosmological parameters*, *A&A* **571** (Nov., 2014) A16, [1303.5076].

[237] S. Naoz, S. Noter and R. Barkana, *The first stars in the Universe*, *MNRAS* **373** (Nov, 2006) L98–L102, [astro-ph/0604050].

[238] M. LoVerde and N. Afshordi, *Extended limber approximation*, *Phys. Rev. D* **78** (Dec, 2008) 123506.

[239] D. N. Limber, *The Analysis of Counts of the Extragalactic Nebulae in Terms of a Fluctuating Density Field.*, *ApJ* **117** (Jan., 1953) 134.

[240] P. Lemos, A. Challinor and G. Efstathiou, *The effect of Limber and flat-sky approximations on galaxy weak lensing*, JCAP **2017** (May, 2017) 014, [1704.01054].

[241] J. S. Bolton, E. Puchwein, D. Sijacki, M. G. Haehnelt, T.-S. Kim, A. Meiksin et al., *The Sherwood simulation suite: overview and data comparisons with the Lyman α forest at redshifts $2 \geq z \geq 5$*, *Mon. Not. Roy. Astron. Soc.* **464** (2017) 897–914, [1605.03462].

[242] V. Springel, N. Yoshida and S. D. M. White, *GADGET: a code for collisionless and gasdynamical cosmological simulations*, *New Astron.* **6** (Apr., 2001) 79–117, [astro-ph/0003162].

[243] V. Springel, *The cosmological simulation code GADGET-2*, *MNRAS* **364** (Dec., 2005) 1105–1134, [astro-ph/0505010].

[244] M. Viel, M. G. Haehnelt and V. Springel, *Inferring the dark matter power spectrum from the Lyman α forest in high-resolution QSO absorption spectra*, *MNRAS* **354** (Nov., 2004) 684–694, [astro-ph/0404600].

[245] A. H. Pawlik, J. Schaye and E. van Scherpenzeel, *Keeping the Universe ionized: photoheating and the clumping factor of the high-redshift intergalactic medium*, *MNRAS* **394** (Apr., 2009) 1812–1824, [0807.3963].

[246] J. Chardin, G. Kulkarni and M. G. Haehnelt, *Self-shielding of hydrogen in the IGM during the epoch of reionization*, *MNRAS* **478** (July, 2018) 1065–1076, [1707.06993].

[247] F. Haardt and P. Madau, *Radiative Transfer in a Clumpy Universe. IV. New Synthesis Models of the Cosmic UV/X-Ray Background*, *ApJ* **746** (Feb., 2012) 125, [1105.2039].

[248] G. D. Becker, J. S. Bolton, M. G. Haehnelt and W. L. W. Sargent, *Detection of extended He II reionization in the temperature evolution of the intergalactic medium*, *MNRAS* **410** (Jan., 2011) 1096–1112, [1008.2622].

[249] J. Oñorbe, F. B. Davies, Z. Lukić, J. F. Hennawi and D. Sorini, *Inhomogeneous Reionization Models in Cosmological Hydrodynamical Simulations*, *arXiv e-prints* (Oct, 2018) arXiv:1810.11683, [1810.11683].

[250] G. Kulkarni, J. F. Hennawi, J. Oñorbe, A. Rorai and V. Springel, *Characterizing the Pressure Smoothing Scale of the Intergalactic Medium*, *ApJ* **812** (Oct., 2015) 30, [1504.00366].

[251] J. Oñorbe, J. F. Hennawi and Z. Lukić, *Self-consistent Modeling of Reionization in Cosmological Hydrodynamical Simulations*, *ApJ* **837** (Mar., 2017) 106, [1607.04218].

[252] N. Katz, D. H. Weinberg and L. Hernquist, *Cosmological Simulations with TreeSPH*, *ApJS* **105** (July, 1996) 19, [`astro-ph/9509107`].

[253] S. Ikeuchi and J. P. Ostriker, *Evolution of the intergalactic medium - What happened during the epoch Z = 3-10?*, *ApJ* **301** (Feb., 1986) 522–543.

[254] D. Aubert and R. Teyssier, *A radiative transfer scheme for cosmological reionization based on a local Eddington tensor*, *MNRAS* **387** (June, 2008) 295–307, [`0709.1544`].

[255] D. Aubert and R. Teyssier, *Reionization Simulations Powered by Graphics Processing Units. I. On the Structure of the Ultraviolet Radiation Field*, *ApJ* **724** (Nov., 2010) 244–266, [`1004.2503`].

[256] L. C. Keating, E. Puchwein and M. G. Haehnelt, *Spatial fluctuations of the intergalactic temperature-density relation after hydrogen reionization*, *MNRAS* **477** (July, 2018) 5501–5516, [`1709.05351`].

[257] B. Greig, A. Mesinger, Z. Haiman and R. A. Simcoe, *Are we witnessing the epoch of reionisation at* $z = 7.1$ *from the spectrum of J1120+0641?*, *MNRAS* **466** (Apr., 2017) 4239–4249, [`1606.00441`].

[258] F. B. Davies, J. F. Hennawi, E. Bañados, Z. Lukić, R. Decarli, X. Fan et al., *Quantitative Constraints on the Reionization History from the IGM Damping Wing Signature in Two Quasars at z > 7*, *ApJ* **864** (Sep, 2018) 142, [`1802.06066`].

[259] I. D. McGreer, A. Mesinger and V. D'Odorico, *Model-independent evidence in favour of an end to reionization by* $z \approx 6$, *MNRAS* **447** (Feb., 2015) 499–505, [`ArXiv:1411.5375`].

[260] G. Worseck, J. X. Prochaska, J. F. Hennawi and M. McQuinn, *Early and Extended Helium Reionization over More Than 600 Million Years of Cosmic Time*, *ApJ* **825** (July, 2016) 144, [`1405.7405`].

[261] G. Worseck, F. B. Davies, J. F. Hennawi and J. X. Prochaska, *The Evolution of the HeII-Ionizing Background at Redshifts 2.3<z<3.8 Inferred from a Statistical Sample of 24 HST/COS HeII Ly*α *Absorption Spectra*, *Astrophys. J.* **875** (2019) 111, [`1808.05247`].

[262] A. Mesinger, S. Furlanetto and R. Cen, *21CMFAST: a fast, seminumerical simulation of the high-redshift 21-cm signal*, *MNRAS* **411** (Feb., 2011) 955–972, [`1003.3878`].

[263] A. Mesinger and S. Furlanetto, *Efficient Simulations of Early Structure Formation and Reionization*, *ApJ* **669** (Nov., 2007) 663–675, [`0704.0946`].

[264] Y. B. Zel'Dovich, *Reprint of 1970A&A.....5...84Z. Gravitational instability: an approximate theory for large density perturbations.*, *A&A* **500** (Mar, 2070) 13–18.

[265] G. Efstathiou, M. Davis, S. D. M. White and C. S. Frenk, *Numerical techniques for large cosmological N-body simulations*, *ApJS* **57** (Feb, 1985) 241–260.

[266] F. B. Davies, G. D. Becker and S. R. Furlanetto, *Determining the Nature of Late Gunn-Peterson Troughs with Galaxy Surveys*, *ApJ* **860** (Jun, 2018) 155, [`1708.08927`].

[267] F. B. Davies, S. R. Furlanetto and K. L. Dixon, *A self-consistent 3D model of fluctuations in the helium-ionizing background*, *MNRAS* **465** (Mar, 2017) 2886–2894, [`1703.10177`].

[268] M. G. Santos, L. Ferramacho, M. B. Silva, A. Amblard and A. Cooray, *Fast large volume simulations of the 21-cm signal from the reionization and pre-reionization epochs*, *MNRAS* **406** (Aug, 2010) 2421–2432, [`0911.2219`].

[269] C. Lacey and S. Cole, *Merger rates in hierarchical models of galaxy formation*, *MNRAS* **262** (June, 1993) 627–649.

[270] J. R. Bond, S. Cole, G. Efstathiou and N. Kaiser, *Excursion set mass functions for hierarchical Gaussian fluctuations*, *ApJ* **379** (Oct., 1991) 440–460.

[271] S. R. Furlanetto, M. Zaldarriaga and L. Hernquist, *Statistical Probes of Reionization with 21 Centimeter Tomography*, *ApJ* **613** (Sept., 2004) 16–22, [`astro-ph/0404112`].

[272] T. R. Choudhury, M. G. Haehnelt and J. Regan, *Inside-out or outside-in: the topology of reionization in the photon-starved regime suggested by Lyα forest data*, *MNRAS* **394** (Apr., 2009) 960–977, [`0806.1524`].

[273] A. Mesinger, S. Furlanetto and R. Cen, *21CMFAST: a fast, seminumerical simulation of the high-redshift 21-cm signal*, *MNRAS* **411** (Feb., 2011) 955–972, [`1003.3878`].

[274] G. Kulkarni, T. R. Choudhury, E. Puchwein and M. G. Haehnelt, *Models of the cosmological 21 cm signal from the epoch of reionization calibrated with Ly α and CMB data*, *MNRAS* **463** (Dec., 2016) 2583–2599, [`1607.03891`].

[275] S. R. Furlanetto, M. Zaldarriaga and L. Hernquist, *The Growth of H II Regions During Reionization*, *ApJ* **613** (Sept., 2004) 1–15, [`astro-ph/0403697`].

[276] L. Knox, *Determination of inflationary observables by cosmic microwave background anisotropy experiments*, *Phys. Rev. D* **52** (Oct, 1995) 4307–4318, [`astro-ph/9504054`].

[277] K. Abazajian, G. Addison, P. Adshead, Z. Ahmed, S. W. Allen, D. Alonso et al., *CMB-S4 Science Case, Reference Design, and Project Plan*, *arXiv e-prints* (Jul, 2019) arXiv:1907.04473, [1907.04473].

[278] T. Essinger-Hileman, A. Ali, M. Amiri, J. W. Appel, D. Araujo, C. L. Bennett et al., *CLASS: the cosmology large angular scale surveyor*, in *Proceedings of the SPIE*, vol. 9153 of *Society of Photo-Optical Instrumentation Engineers (SPIE) Conference Series*, p. 91531I, Jul, 2014, 1408.4788, DOI.

[279] S. Mukherjee, S. Paul and T. R. Choudhury, *Is patchy reionization an obstacle in detecting the primordial gravitational wave signal?*, *arXiv e-prints* (Mar, 2019) arXiv:1903.01994, [1903.01994].

[280] A. Lewis, *Cosmological parameters from WMAP 5-year temperature maps*, *Phys. Rev.* **D78** (2008) 023002, [0804.3865].

[281] S. Dumitru, G. Kulkarni, G. Lagache and M. G. Haehnelt, *Predictions and sensitivity forecasts for reionization-era [C II] line intensity mapping*, *MNRAS* **485** (May, 2019) 3486–3498, [1802.04804].

[282] L. C. Keating, L. H. Weinberger, G. Kulkarni, M. G. Haehnelt, J. Chardin and D. Aubert, *Long troughs in the Lyman-α forest below redshift 6 due to islands of neutral hydrogen*, *arXiv e-prints* (May, 2019) arXiv:1905.12640, [1905.12640].

[283] E. Vanzella et al., *The Great Observatories Origins Deep Survey: Constraints on the Lyman Continuum Escape Fraction Distribution of Lyman–Break Galaxies at $3.4 < z < 4.5$*, *Astrophys. J.* **725** (2010) 1011–1031, [1009.1140].

[284] J. Chisholm, S. Gazagnes, D. Schaerer, A. Verhamme, J. R. Rigby, M. Bayliss et al., *Accurately predicting the escape fraction of ionizing photons using rest-frame ultraviolet absorption lines*, *A&A* **616** (Aug, 2018) A30, [1803.03655].

[285] C. C. Steidel, M. Bogosavljević, A. E. Shapley, N. A. Reddy, G. C. Rudie, M. Pettini et al., *The Keck Lyman Continuum Spectroscopic Survey (KLCS): The Emergent Ionizing Spectrum of Galaxies at $z \sim 3$*, *ApJ* **869** (Dec, 2018) 123, [1805.06071].

[286] J. Japelj, E. Vanzella, F. Fontanot, S. Cristiani, G. B. Caminha, P. Tozzi et al., *Constraints on the Lyman continuum escape fraction for faint star-forming galaxies*, *MNRAS* **468** (June, 2017) 389–403, [1612.06401].

[287] A. E. Shapley, C. C. Steidel, A. L. Strom, M. Bogosavljević, N. A. Reddy, B. Siana et al., *Q1549-C25: A Clean Source of Lyman-Continuum Emission at $z = 3.15$*, *ApJL* **826** (Aug., 2016) L24, [1606.00443].

[288] R. E. Mostardi, A. E. Shapley, C. C. Steidel, R. F. Trainor, N. A. Reddy and B. Siana, *A High-Resolution Hubble Space Telescope Study of Apparent Lyman Continuum Leakers at z˜3*, *ApJ* **810** (Sept., 2015) 107, [`1506.08201`].

[289] S. Borthakur, T. M. Heckman, C. Leitherer and R. A. Overzier, *A local clue to the reionization of the universe*, *Science* **346** (Oct., 2014) 216–219, [`1410.3511`].

[290] A. Grazian, E. Giallongo, R. Gerbasi, F. Fiore, A. Fontana, O. Le Fèvre et al., *The Lyman continuum escape fraction of galaxies at $z = 3.3$ in the VUDS-LBC/COSMOS field*, *A&A* **585** (Jan., 2016) A48, [`1509.01101`].

[291] Y. I. Izotov, I. Orlitová, D. Schaerer, T. X. Thuan, A. Verhamme, N. G. Guseva et al., *Eight per cent leakage of Lyman continuum photons from a compact, star-forming dwarf galaxy*, *Nature* **529** (Jan., 2016) 178–180, [`1601.03068`].

[292] Y. I. Izotov, G. Worseck, D. Schaerer, N. G. Guseva, T. X. Thuan, V. Fricke, A. et al., *Low-redshift Lyman continuum leaking galaxies with high [O III]/[O II] ratios*, *MNRAS* **478** (Aug., 2018) 4851–4865, [`1805.09865`].

[293] Y. I. Izotov, D. Schaerer, G. Worseck, N. G. Guseva, T. X. Thuan, A. Verhamme et al., *J1154+2443: a low-redshift compact star-forming galaxy with a 46 per cent leakage of Lyman continuum photons*, *MNRAS* **474** (Mar., 2018) 4514–4527, [`1711.11449`].

[294] Y. Sekimoto, P. Ade, K. Arnold, J. Aumont, J. Austermann, C. Baccigalupi et al., *Concept design of the LiteBIRD satellite for CMB B-mode polarization*, in *Space Telescopes and Instrumentation 2018: Optical, Infrared, and Millimeter Wave*, vol. 10698 of *Society of Photo-Optical Instrumentation Engineers (SPIE) Conference Series*, p. 106981Y, Aug., 2018, DOI.

[295] N. Krachmalnicoff, C. Baccigalupi, J. Aumont, M. Bersanelli and A. Mennella, *Characterization of foreground emission on degree angular scales for CMB B-mode observations . Thermal dust and synchrotron signal from Planck and WMAP data*, *A&A* **588** (Apr., 2016) A65, [`1511.00532`].

[296] M. Tegmark, A. N. Taylor and A. F. Heavens, *Karhunen-Loève Eigenvalue Problems in Cosmology: How Should We Tackle Large Data Sets?*, *ApJ* **480** (May, 1997) 22–35, [`astro-ph/9603021`].

[297] M. Tegmark, *CMB mapping experiments: A designer's guide*, *Phys. Rev. D* **56** (Oct, 1997) 4514–4529, [`astro-ph/9705188`].

[298] C. Feng and G. Holder, *Searching for patchy reionization from cosmic microwave background with hybrid quadratic estimators*, *Phys. Rev. D* **99** (Jun, 2019) 123502, [`1808.01592`].

[299] N. Krachmalnicoff, E. Carretti, C. Baccigalupi, G. Bernardi, S. Brown, B. M. Gaensler et al., *S-PASS view of polarized Galactic synchrotron at 2.3 GHz as a contaminant to CMB observations*, *A&A* **618** (Oct, 2018) A166, [`1802.01145`].

[300] S. K. Choi and L. A. Page, *Polarized galactic synchrotron and dust emission and their correlation*, JCAP **2015** (Dec, 2015) 020, [`1509.05934`].